

**EFFECTS OF LINEAR ENERGY TRANSFER AND HYPOXIA ON
RADIATION-INDUCED IMMUNOGENICITY THROUGH STING**

by

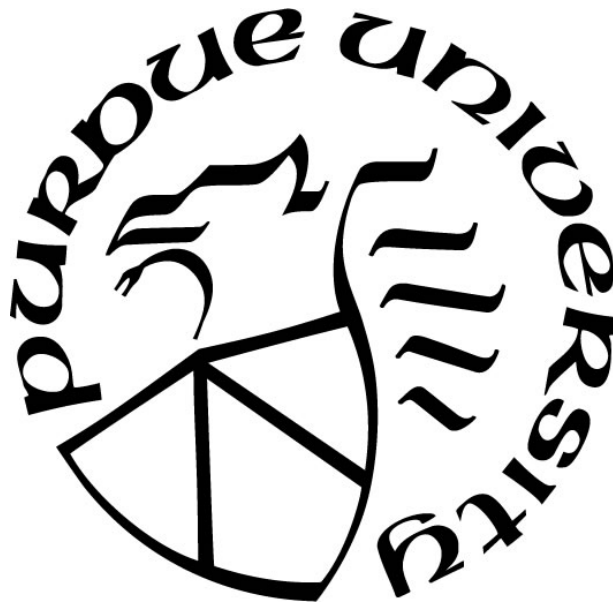
Devin A. Miles

A Dissertation

Submitted to the Faculty of Purdue University

In Partial Fulfillment of the Requirements for the degree of

Doctor of Philosophy



School of Health Sciences

West Lafayette, Indiana

May 2020

**THE PURDUE UNIVERSITY GRADUATE SCHOOL
STATEMENT OF COMMITTEE APPROVAL**

Dr. Keith Stantz, Chair

School of Health Sciences, Purdue University

Dr. Carlos Perez-Torres

School of Health Sciences, Purdue University

Dr. Jeannie Plantenga

Department of Veterinary Clinical Sciences, College of Veterinary Medicine, Purdue University

Dr. Ning Cao

Department of Radiation Oncology, University of Washington

Dr. Vadim Moskvina

Department of Radiation Oncology, St. Jude Children's Research Hospital

Approved by:

Dr. Aaron Bowman

Dedicated to my family, friends, and all who have supported me along the way.

ACKNOWLEDGMENTS

I have many people to thank for the success of this work. First and foremost, I would like to thank my advisor, Keith Stantz, for his unrelenting support and encouragement as this project expanded into uncharted territory in radiation biology and immunology. Additionally, I would like to thank Carlos Perez-Torres, Jeannie Plantenga, Vadim Moskvin, Ning Cao, and Jonathan Farr for their support as members of my advisory committee.

I would like to thank Ning Cao (again), George Sandison, Rob Stewart, Juergen Meyer, and the rest of the Department of Radiation Oncology at the University of Washington for granting me resources and allowing me to explore these new ideas from their labs – it was a privilege. Rob Emery, Dave Argento, Greg Moffitt, Eric Dorman, and Marissa Kranz of the UW medical cyclotron facility kindly tolerated my (nearly) constant requests for beamtime. Support from Thomas Pulliam, Shira Cherny, and Paul Nghiem of UW Dermatology was essential for producing results from my *in vitro* assays, and Helen Chin-Sinex and Marc Mendonca of IUPUI played a critical role in my training for cell culture technique. Ardiana Moustaki and Benjamin Youngblood of the Department of Immunology at St. Jude Children’s Research Hospital, and Eli Lilly & Co. graciously provided mice for our imaging studies. I am grateful to Purdue University and the School of Health Sciences for supporting me throughout my PhD through the Purdue Doctoral Fellowship, Bilsland Fellowship, and HSCI research assistantship.

Last, but not least, I would not have made it this far without the support of my parents, Mark and Rebecca Miles, and without the emotional support from my close friends, Paul Yoon and Titania Juang.

TABLE OF CONTENTS

LIST OF TABLES	8
LIST OF FIGURES	9
ABSTRACT	14
CHAPTER 1. INTRODUCTION	16
1.1 Radiation Therapy and Abscopal Effects	16
1.2 Clinical Abscopal Effects in Merkel Cell Carcinoma.....	18
1.3 Stimulator of Interferon Genes	21
1.4 DNA Damage and Repair	24
1.5 Hypoxia in Radiation Therapy	26
1.6 Hypoxia Imaging, Photoacoustic CT.....	28
1.7 Hypothesis.....	30
CHAPTER 2. SPECIFIC AIMS	32
2.1 Model STING Regulation from DNA Damage Models	32
2.2 Measure STING Regulation from Varying Radiation Sources	32
2.3 Develop Imaging Protocols to Localize and Distinguish Hypoxic Status.....	32
2.4 Innovation and Impact	33
CHAPTER 3. DNA DAMAGE MODELING OF STING RESPONSE IN VARYING CONDITIONS, <i>IN VITRO</i>	34
3.1 Introduction.....	34
3.2. Materials and Methods.....	34
3.2.1 Monte Carlo Damage Simulation	34
3.2.1.1. Source Modeling: X-Rays	36
3.2.1.2. Source Modeling: Charged Particle Beams	37
3.2.2 Retrospective Analysis	37
3.4 Results.....	39
3.4.1 Predicted Effects of High-LET Radiation on STING Regulation	39
3.4.2 Predicted Effects of Varied Oxygenation on STING Regulation.....	43
3.5 Discussion	44

CHAPTER 4. EXPERIMENTAL MEASUREMENT OF STING REGULATION IN VARYING CONDITIONS	46
4.1 Introduction.....	46
4.2 Materials and Methods.....	46
4.2.1 Cell Culture Irradiations	46
4.2.2 Interferon Beta Assay	49
4.2.3 Cytosolic dsDNA Assay.....	50
4.2.4 Exonuclease Trex1 Assay.....	51
4.2.5 Interferon Beta and Trex1 Modeling	52
4.2.6 Modeling IFN β in General Purpose Monte Carlo	53
4.3 Results.....	54
4.3.1 Interferon Beta Dose Response	54
4.3.2 Cytosolic dsDNA Dose Response	56
4.3.3 Exonuclease Trex1 Dose Response	57
4.3.4 Interferon Beta and Trex1 Modeling	59
4.3.5 Modeling IFN β in Particle Transport Monte Carlo.....	61
4.4 Discussion	64
CHAPTER 5. DEVELOPMENT OF IMAGING TECHNIQUES TO LOCALIZE AND DISTINGUISH HYPOXIC STATUS	67
5.1 Introduction.....	67
5.2 Materials and Methods.....	67
5.2.1 Photoacoustic CT.....	67
5.2.2 Murine Tumor Models.....	68
5.2.2.1 Syngeneic MC38.....	68
5.2.2.2 Syngeneic MMTV-PyMT	69
5.2.3 Imaging Analysis.....	69
5.2.3.1 Image Registration	70
5.2.3.2 PCT Calibration.....	70
5.2.3.1 PCT Analysis – single image sets	73
5.2.3.1 PCT Analysis – longitudinal image sets and hypoxia classification.....	74
5.3 Results.....	76

5.3.1 Syngeneic MC38	78
5.3.2 Syngeneic MMTV-PyMT	81
5.4 Discussion	86
CHAPTER 6. DISCUSSION.....	88
CHAPTER 7. CONCLUSIONS AND FUTURE WORKS.....	92
REFERENCES	94
APPENDIX A. INTERFERON BETA ELISA PROTOCOL	103
APPENDIX B. TREX1 IMMUNOFLUORESCENCE PROTOCOL	107
APPENDIX C. CYTOSOLIC DSDNA QUANTIFICATION PROTOCOL.....	109
VITA.....	111

LIST OF TABLES

Table 1. Fit coefficients for a variety of human and murine cells for cytosolic dsDNA and Trex1 dose response as a function of physical dose and the number of DSB clusters per Gy, as modeled in MCDS. Fits were performed using the MATLAB curve fitting toolbox. Cytosolic dsDNA fits used the built-in Gauss1 equation (3.2). Trex1 data was fitted to a sigmoid function (3.3).....	41
Table 2. DNA damage coefficients calculated in MCDS for a variety of radiation sources, varying oxygenation. Photon sources were input as polyenergetic secondary electron spectra, calculated using FLUKA particle transport Monte Carlo. Electron, proton, and helium ion sources were input as monoenergetic for simplicity, due to range dependencies arising from continuous average energy loss across iontherapy beams.	42
Table 3. Fit coefficients for IFN β and Trex1 dose response following SARRP x-ray or CNTS fast neutron irradiation. IFN β measurements were fitted to a single-term Gaussian function, and Trex1 was fitted to a sigmoid function using the MATLAB curve fitting toolbox (Eqn. 1 and 2).....	60

LIST OF FIGURES

- Figure 1. An MCC patient receiving a combination of neutron beam therapy and immunotherapy (anti-PD1). A+B show the lesions directly treated with neutrons by two fractions of 3 Gy, circled in red. The blue-circled lesions were not directly treated. C+D show the patient at one month following treatment, showing complete remission. Photo from Schaub et al. (2019).....20
- Figure 2. The cGAS-STING signaling pathway. DNA stress leads to cytosolic DNA accumulation by micronucleus formation and rupture. DNA is sensed by cGAS and used to activate transcription factors IRF3 and NF- κ B, leading to production of inflammatory cytokines. Figure from Li et al. (2018).....22
- Figure 3. Summary of DNA damage induced by ionizing radiation, and repair mechanisms for each. Single strand breaks and base damages are repaired through base-excision repair (BER). Double strand breaks, whether clustered or base damage-adjacent, are repaired through homologous repair (HR) during S/G2, and non-homologous end joining (NHEJ) during the rest of the cell cycle. Figure from R. Stewart lecture on DNA repair, Univ. of Washington resident didactics (2019).....25
- Figure 4. (Top) The mechanism of oxygen fixation of radiation-induced DNA damage. DNA damage from indirect action relies on free radicals produced in water radiolysis, which are conventionally ‘fixed’ by chemical reactions with oxygen. When oxygen is removed, this fixation is no longer possible. (Bottom) The effect of oxygenation on radiation sensitivity. Fully oxygenated cells are roughly three times more radiosensitive than fully anoxic cells. Figures from the 7th edition of Radiobiology for the Radiologist (Hall, Giacca; 2012).....26
- Figure 5. The effects of limitations in oxygen perfusion and diffusion on hypoxic status. Hypoxic cells are illustrated in blue, normoxic cells in yellow. Chronic hypoxia (left) occurs in cells that reside beyond the diffusion length of oxygen from blood supply, dependent on the distance away from a blood vessel. Acute hypoxia occurs in cells that reside near an occluded blood vessel, which is occasionally perfused with blood, leading to oxygenation that varies with time. Figure from Horsman et al. (2013)27
- Figure 6. Optical absorption coefficients for hemoglobin, water, fat as a function of photon wavelength. At near-infrared wavelengths (shaded in yellow), the main absorbers of photons are hemoglobin (Hb) and oxyhemoglobin (HbO₂). Near-infrared light also interacts in water and fat, but the absorption coefficients are 3 orders of magnitude lower than hemoglobin. Figure from Mehrmohammadi et al. (2013)29
- Figure 7. Example of DNA lesion distribution and clustering across two strands of DNA, as modeled in MCDS. N_{\min} refers to the minimum separation for two lesions to be considered of separate clusters. Lesion 1 consists of a DSB with a nearby SSB. Lesion 2 consists of two SSB on the same strand. Figure from Stewart et al. 200435

Figure 8. FLUKA simulation geometry to calculate the secondary electron fluence following exposure to 220 kVp x-rays. A 0.1-mm diameter beamlet of 220 keV electrons are directed at a tungsten anode, creating bremsstrahlung and characteristic x-rays that propagate out. The resulting x-rays pass through a 0.8 mm beryllium window and a 0.15 mm brass foil to attenuate low-energy x-rays. At 35 cm away from the source, a cell culture plate is placed, where secondary electrons are measured after passing through 2 mm of water.37

Figure 9. Published data for cytosolic dsDNA and Trex1 dose response from Vanpouille-Box et al. (2017) for a variety of human (MDS-MB-231, 4157TR) and murine (4T1, MC38, TSA) cells. Cytosolic dsDNA (top) follows a Gaussian trend, with varying amplitude and background concentrations per cell type. Trex1 (bottom) roughly follows a sigmoidal trend, with varying ‘plateau’ amplitudes.38

Figure 10. Predicted cytosolic dsDNA accumulation following radiation with SARRP x-rays, monoenergetic 1 MeV protons, and monoenergetic 1 MeV helium ions. Higher-LET radiation induces more DSB per Gy, resulting in accumulation of cytosolic dsDNA at lower doses (left). The ratio of doses for peak cytosolic dsDNA is the ratio of Σ between sources, i.e. the RBE_{DSB} . The rapid buildup of dsDNA followed by upregulation of Trex1 at lower doses (right).40

Figure 11. Predicted cytosolic dsDNA dose response following SARRP irradiation, varying oxygenation. Hypoxic cells experience fewer effective initial DSB per Gy due to the lack of oxygen fixation and enhanced chemical repair. Lower mmHg condition yield fewer DSB per Gy, resulting in accumulation of cytosolic dsDNA at higher doses (left). The ratio of doses for peak cytosolic dsDNA is the ratio of Σ between oxygen conditions, i.e. the oxygen enhancement ratio. The shallower buildup of dsDNA is followed by upregulation of Trex1 at higher doses (right). .43

Figure 12. Predicted dose to achieve peak cytosolic dsDNA for a variety of radiation sources, as a function of cellular oxygenation. Lower-LET sources, such as photons, are expected to experience peak dsDNA accumulation at higher doses, and experience oxygen enhancement effects that can triple the dose to achieve peak response. Higher LET radiation is able to drive dsDNA accumulation at lower doses, with lesser dependence on oxygenation.44

Figure 13. Cell culture flask set up for irradiation on an Xstrahl SARRP. The SARRP uses a copper filter, with the collimator removed to expand the field as much as possible. The stage is also lowered to enable the highest amount of beam divergence possible. The flask, here a T75, is aligned to the treatment field with lasers.47

Figure 14. Cell culture plates set up for irradiation using the Clinical Neutron Therapy System at the University of Washington. Cells are irradiated from the bottom-up with 2cm of solid water, to ensure that the cells are beyond the buildup region of the neutron PDD. Due to the low dose rate and limited efficiency of neutron production, 4 samples were irradiated at once with staggered doses to minimize the total delivered dose and lessen damage to the CNTS beryllium target.48

Figure 15. Secreted IFN β dose response in MCC13 cells following SARRP x-ray irradiation and CNTS fast neutron irradiation by ELISA. The ratio of these peak doses is 2.4, approximately equivalent to the RBE_{DSB} reported for CNTS neutrons. There is no significant difference in the amplitude of peak IFN β secretion ($P > 0.05$; paired t-test).55

Figure 16. The effects of passage number on peak interferon beta production, and the RBE-weighted dose to achieve peak IFN β . (Top) The peak amplitude of IFN β steeply decreases with passage. (Bottom) The dose required to induce peak IFN β secretion steadily increases with passage. These trends support published data indicating that cells maintained in culture will gradually see inhibit their innate immune response due to lack of stromal and immune components *in vitro* (Mouriaux et al., 2016).56

Figure 17. Cytosolic dsDNA dose response in MC38 cells following SARRP x-ray irradiation. The peak at 12 was not reproduced from Vanpouille-Box (2017, shown in green), while the background dsDNA was comparable. Due to the success of the IFN β and Trex1 assays, this was assumed to be a procedural issue.57

Figure 18. Measured TREX1 dose response in MCC13 cells following SARRP x-ray irradiation and CNTS fast neutron irradiation. Dose responses are normalized to background expression of TREX1. The ratio of slopes, i.e. the RBE_{TREX1}, is 4.0.....58

Figure 19. Trex1 dose response in MC38 cells following ionizing radiation. As the passage number increases, the dose response appears less sigmoidal.....59

Figure 20. Modeled IFN β and Trex1 regulation as a function of dose, for SARRP x-rays, fast neutrons, 6 MV x-rays, low-energy protons, and low-energy carbon ions. (Top) IFN β secretion as a function of dose for various radiation sources. High-LET radiation induces more DSB Gy⁻¹ and have a larger RBE_{DSB}, which parallels the increased efficiency of IFN β secretion. (Bottom) Trex1 upregulation as a function of dose for various radiation sources. Accumulation of DNA damage at lower doses enables Trex1 upregulation at lower doses. All fits to measured data use inputs for MCC13 cells (Table 1, 2).....61

Figure 21. Monte Carlo model of IFN β dose-response for 6 MV x-rays, CNTS fast neutrons, protons, alpha particles, and carbon ions. (Left panel) Depth-dose plots for a variety of clinical beams, normalized to produce peak IFN β in MCC13s treated at the depth of max dose. (Right) IFN β secretion as a function of depth in water for varying clinical beams. Delivered doses for ion sources can be normalized such that IFN β is only stimulated around their Bragg peak; heavier ions can produce sharper regions of pro-immunogenic activity than indirectly ionizing x-rays or neutrons. Uncharged sources can stimulate elevated IFN β more uniformly with depth.63

Figure 22. Schematic of the Nexus128 photoacoustic CT scanner. An OPO-tunable YAG laser is directed through a fiber optic cable into the bowl of the PCT scanner. A tumor sample held in the upper ‘bowl’ of the scanner is excited by exposure to the laser, creating ultrasound signals that propagate outward at a nearly-constant velocity. Sampling the timing of these ultrasound signals enables the origin of the absorption to be calculated. Figure from Justin Sick thesis (2016)68

Figure 23. The PCT calibration GUI. Entire PCT-S datasets can be loaded to confirm the success of 2D or 3D coregistration. Once coregistration is confirmed, the PCT-S Calibration function can be used to write a PCT-S spectra data file for fitting and determination of SaO₂, CtHb. PCT-Calibration can be run in batch mode, for datasets that use the same laser data file. A 3D ROI drawing function was designed to contour the tumor. Voxel intensities can be plotted as a function of wavelength to visualize the variability in NIR light absorption, or as a function of time to examine the effects from longitudinal (or potentially, dynamic contrast enhanced) imaging.....73

Figure 24. The longitudinal PCT analysis GUI. PCT-S data that has been fitted to Eqn. 5.1 can be loaded to visualize and calculate changes in SaO₂ and CtHb over time. The displayed images are average, standard deviation, and maximum intensity of the SaO₂ (top row) and CtHb (middle row) over time. Data from individual voxels can be plotted (bottom row) as a function of time for a direct visualization of SaO₂/CtHb variability with time. Using an SaO₂ threshold in voxels that always contain hemoglobin, hypoxia classification can be determined here.75

Figure 25. Illustration of hypoxia classification based on voxel SaO₂, in voxels containing hemoglobin. If the SaO₂ is always under the hypoxia threshold (0.2) during longitudinal scanning, it is considered chronically hypoxic. If the SaO₂ is both above and below the threshold at some point during scanning, it is considered acutely hypoxic. If the SaO₂ is always above the threshold, it is considered normoxic.77

Figure 26. MC38 tumor growth over time. Tumor sizes were measured using calipers.78

Figure 27. Representative PCT maps for a single MC38 tumor imaged on different days. For hypoxia classification, blue voxels are normoxic, red voxels are acutely hypoxic, and green voxels are chronically hypoxic. The SaO₂ and CtHb were, on average, highest for the earliest scans where the tumor was smallest. As the tumor volume increases, SaO₂ and CtHb decreased. As a result, only some acute hypoxia was classified in the tumor early on. With growth, the tumor become more acutely hypoxic, eventually developing regions of chronic hypoxia.79

Figure 28. Trends in tumor hypoxia for MC38 tumors. Data shown is taken from longitudinal scans for the entire cohort of tumors. As demonstrated before, hypoxia in smaller tumors is predominantly acute, and chronic hypoxia appears as the tumor is allowed to grow. The relative amount of normoxic tissue was roughly constant.80

Figure 29. MMTV-PyMT tumor volumes, measured using calipers on the day of imaging. All treatment groups saw a reduction in tumor growth by the time of imaging, relative to the IgG4 control. Tumors treated with Ang2 alone saw the highest degree of growth suppression, but this was not significantly different from the other treatment groups.81

Figure 30. SaO₂ trends for MMTV-PyMT treated with anti-angiogenic drugs. DC101-treated tumors had a significantly higher SaO₂ than those treated with Ang2 or combination therapy. DC101+Ang2-treated tumors had a significantly lower SaO₂ than DC101 or Ang2 alone. (*P < 0.05; paired t-test)82

Figure 31. Hemoglobin concentration trends for MMTV-PyMT tumors treated with anti-angiogenic drugs. DC101-treated tumors had a significantly lower CtHb than those treated with combination therapy. (*P < 0.05; paired t-test)83

Figure 32. Acute hypoxia trends for MMTV-PyMT tumors treated with anti-angiogenic drugs. DC101-treated tumors had a significantly lower fraction of acute hypoxia than all other groups. DC101+Ang2-treated tumors had a significantly higher fraction of acute hypoxia than DC101 and the control but were not statistically different from tumors treated with Ang2 alone. (*P < 0.05; **P < 0.01; paired t-test)84

Figure 33. Chronic hypoxia trends for MMTV-PyMT tumors treated with anti-angiogenic drugs. DC101-treated tumors had a significantly lower fraction of chronic hypoxia than all other groups. (*P < 0.05; **P < 0.01; paired t-test)85

Figure 34. Overall hypoxic fraction trends for MMTV-PyMT tumors treated with various anti-angiogenic drugs. DC101-treated tumors had a significantly lower hypoxic fraction than all other groups. On average, MMTV-PyMT tumors had the highest hypoxic fraction following combination therapy, but this was not statistically different from Ang2 alone or the control group. (*P < 0.05; **P < 0.01; paired t-test).....86

ABSTRACT

Purpose: Preclinical studies have demonstrated that cancer cells may produce innate immune signals such as type-I interferons following radiation damage, which derives from activation of the cGAS-STING pathway following detection of cytosolic dsDNA. Limited studies have explored how these mechanisms vary from the conditions of the radiation exposure. High-linear energy transfer (LET) radiation induces more DNA double-strand breaks (DSB) per dose than low-LET radiation, thus is expected to be more immunogenic. However, DNA damage in hypoxic cells is more probable to undergo chemical repair due to limitations in oxygen fixation, thus is expected to be more immunosuppressive. Our goal is to study and model the dose response characteristics of IFN β and Trex1 *in vitro* following exposure of radiations with varying LET and to develop techniques for further study *in vivo*.

Methods: Reference data from Vanpouille-Box (2017) on STING dose response was applied to develop empirical models of cytosolic dsDNA and Trex1 regulation as a function of dose and quantity of DNA DSB, the latter of which is dependent on particle LET and oxygenation and is calculated using Monte Carlo Damage Simulation (MCDS) software. These models were used as preliminary data to guide *in vitro* experiments using Merkel cell carcinoma cells. The dose response of pro-inflammatory IFN β and exonuclease Trex1, an anti-inflammatory suppressor of cGAS-STING, was measured post-irradiation. MCDS was again used to model fast neutron relative biological effectiveness for DSB induction (RBE_{DSB}) and compared to laboratory measurements of the RBE for IFN β production ($RBE_{IFN\beta}$). $RBE_{IFN\beta}$ models were applied to radiation transport simulations to quantify the potential secretion of IFN β in representative clinical beams. To enable intra-tumor radiation targeting of tumor hypoxia, mice were seeded with syngeneic tumors and imaged longitudinally with PCT-spectroscopy to determine local variations hemoglobin concentration (Hb) and oxygen saturation (SaO₂) over time. Hypoxia classification was based on SaO₂ levels in voxels containing hemoglobin relative to a “hypoxia threshold” of $SaO_2 < 0.2$.

Results: Based on analysis of published data, our preliminary models of cytosolic DNA and Trex1 dose responses demonstrate dose enhancements from high-LET radiation, such as that at the distal edge of a Bragg peak, and suppression from cellular hypoxia. This manifests as an

RBE-dependent ‘shift’ in STING response. Laboratory measurements in MCC13 cells show peak IFN β production at 6.1 Gy following fast neutron irradiation and 14.5 Gy following x-rays (RBE_{IFN β} = 2.4). However, IFN β signal amplitudes were not significantly different between these radiation types. Trex1 signal increased linearly with dose, with fourfold higher upregulation per dose for fast neutrons. Modeling of RBE in clinical beams suggests that ion sources may induce spatially localized IFN β near their end of range, which is potentially advantageous for initiation of tumor-specific immune activity. Uncharged sources stimulate IFN β more uniformly with depth. Longitudinal PCT-S scanning is able to localize and distinguish chronic and acute hypoxia *in vivo*. Changes in the hypoxic classification from tumor growth and following anti-angiogenic therapy are distinguishable.

Conclusion: Radiation-induced immunogenicity can be induced differentially based on radiation quality and is expected to be affected by cellular oxygenation. High-LET radiation, such as fast neutrons, drives greater IFN β innate immune response per dose than low-LET radiation, such as x-rays, which may enhance abscopal effects when used in combination with immune-stimulating agents. However, anti-inflammatory signaling is greater per dose for fast neutrons, and it remains unclear if high-LET radiations are therapeutically advantageous over low-LET radiation for pro-inflammatory tumor signaling. High resolution *in vivo* imaging of tumor hypoxia is feasible with photoacoustic techniques, which can potentially be leveraged to study selective immunogenicity enhancement of the hypoxic niche following radiation therapy.

CHAPTER 1. INTRODUCTION

1.1 Radiation Therapy and Abscopal Effects

In 2020, an estimated 2 million people in the US will be diagnosed with some form of cancer, and roughly 50% of them will receive therapeutic radiation over the course of their treatment¹. Radiation has been used as a therapeutic tool against cancer since the late 1800's, with early documented cases within the first 5 years following the discovery of x-rays^{2,3}. In the following century, the technology to enable radiation delivery has advanced with the goal of sufficiently treating a disease site while sparing adjacent healthy tissue. The development of the linear accelerator enabled x-ray energies to increase from kilovoltage to megavoltage, leading to superficial normal tissue sparing and enhanced target coverage at-depth⁴. Beam-shaping tools evolved from collimators to compensator to multi-leaf collimators. Anatomical imaging and external-beam simulation advanced toward comprehensive 3D dose simulation, such as 3D conformal radiotherapy or Intensity Modulated Radiation Therapy (IMRT), which enable treatment of lesions any part of the body with sub-centimeter precision. Across these advancements, the common goal of radiation therapy remains the same: achieve local control of disease while limiting nearby organ-at-risk doses. However, in some rare cases, directly irradiating a tumor can result in suppression of 'out of field' disease sites.

These out of field effects, coined as 'abscopal effects,' were first described by Robert Mole in the *Journal of British Radiology* in 1953⁵. Early experiments detail a single fraction of 6-10 Gy of radiation delivered abdominally to rats, resulting in a 75% decrease thyroid hormone secretion. Mole emphasized that these effects were not a result of whole-body irradiation or targeted irradiation of lymphatic tissue. The given explanation postulates that an organism is a single, closed system, and stimulation of one piece can drive changes to the whole system. This was the first publication that documented local radiation having systemic effects "at a distance from the irradiated volume but within the same organism."

The relevance of this concept to cancer therapy was demonstrated in patient case studies in the decades following⁶. One such example is a case study from 1969, describing therapy for a

patient suffering from a malignant lymphoma that had metastasized to lymph nodes in the lungs and pelvis. Treatment was given to the whole pelvis with palliative intent, with a total of 3,500 rads (35 Gy) delivered over 26 days. By completion, all irradiated lymph nodes were no longer palpable, and within one month following treatment the patient was entirely asymptomatic. The author speculated that irradiation depleted abnormal lymphocytes, driving a rapid recirculation of new lymphocytes. As new lymphocytes emerge into the pelvis, they resulted in a “generalized great decrease in circulating tumor cells.”

Modern developments in immunology and cancer biology have determined that these rare effects are a result of the patients developing an immune response to their disease, with tumor death mediated by cytotoxic T-cells that have become primed by antigens created from dying cells^{7,8}. The rarity of abscopal effects comes as an artifact of how spontaneous cancers form⁹. Mutant cells that do not develop some means to evade immune surveillance are often swiftly destroyed – thus cells that are able to survive long enough to form palpable tumors will have some intrinsic means of evading surveillance. This evasion broadly manifests as two key traits: limiting the immune system’s capacity to interact with cancer cells and limiting the antigens produced by cancer cells¹⁰⁻¹². These traits inhibit the immune system’s ability to distinguish “non-self” antigens, such as those from dying cancer cells, from “self” antigens, such as those from healthy cells.

Enhancing the immune system’s capacity to recognize, infiltrate, and interact with cancer cells has been an ongoing focus in the field of clinical immunotherapy¹³. Common clinical approaches involve removing the ‘brakes’ on immune checkpoints, through the blockade of programmed death-1 (PD1) and cytotoxic T-lymphocyte antigen 4 (CTLA4) mechanisms^{14,15}. CTLA-4 functions to indirectly suppress killer T-cell functionality by limiting costimulatory signals at priming¹⁵. PD-1 directly suppresses T-cell function by surface antigens on target cells inducing T-cell apoptosis¹⁶. Both of these immune checkpoints are nominally immunosuppressive, and function to prevent autoimmunity in healthy cells, and both are capable of disrupting CD8+ T-cells from targeting cancer cells.

While the development of immune checkpoint inhibitors has been groundbreaking, their effectiveness alone is limited. An estimated 45% of cancer patients are eligible to receive immune

checkpoint inhibitors, but only 13% will notice a benefit with respect to disease control¹⁷. The rarity of successful abscopal effects can be tracked through the literature – with only 23 case studies published from 1964-2014¹⁸.

1.2 Clinical Abscopal Effects in Merkel Cell Carcinoma

Merkel cell carcinoma (MCC) is a rare, aggressive, small-cell skin cancer that is typically associated with sustained ultraviolet radiation exposure, such as sunlight, or infection of the Merkel cell polyomavirus (MCPyV)¹⁹. Genomic integration of MCPyV was detected in 8 out of 10 MCCs, but both means of incidence generally result from a combination of immunosuppression and DNA damage²⁰. Therapeutic response is differential between MCPyV-positive and MCPyV-negative MCCs, as well as in MCC patients that are subject to chronic immunosuppression, such as HIV or lupus²¹. MCC patients with chronic immunosuppression generally see enhanced cumulative incidence of MCC-specific death, with higher rates of local, regional, and distant recurrence following radiation therapy²¹. Responsiveness to immunotherapy is dependent on T-cell infiltration, with tumors bearing well-present CD8+ T-cells accounting for less than 20% of MCCs²⁰.

As the last line of treatment options, MCC patients that prove unresponsive to conventional IMRT and immunotherapy, alone, are being treated with neutron beam radiation therapy using 50 MV fast neutrons at the Clinical Neutron Therapy System (CNTS) at the University of Washington^{22,23}. This is currently the only remaining facility capable of treating human patients with fast neutron therapy. Neutrons are produced by directing cyclotron-accelerated 50.5 MeV protons onto a water-cooled Beryllium target, generating neutrons primarily through (p, n) and (p, n + p) reactions^{24,25}. The resulting neutron beam is directed through a steel flattening filter to flatten the dose profile shaped to the target profile with an MLC system. MLC leaves consist of iron doped with polyethylene inserts to ensure full beam attenuation. The average neutron energy at the depth of max dose is roughly 16.1 MeV. Most neutron dose contributions are due to secondary charged particles through neutron transmutation interactions with water, either low-energy protons produced in (n, p) interactions with hydrogen or low-energy alpha particles through (n, alpha) interactions with oxygen²⁶. For the endpoint of DNA double-strand break induction, these neutrons have an RBE of 2.7 relative to Cobalt-60 gamma rays²⁶.

Case studies from the University of Washington observed what appeared to be abscopal effects in MCC patients treated with both immunotherapy drugs and neutron radiation therapy, that were previously treated and unresponsive to x-ray radiation and immunotherapy alone. As an example, one patient with an immunosuppressive disease (chronic lymphocytic leukemia) was diagnosed with a non-viral MCC and initially treated with a single fraction of 8-Gy using MV x-rays²². After a short-lived initial response, in-field disease progressed within 6 weeks of the treatment, with additional lesions occurring on the skin. This patient began anti-PD1 immunotherapy treatment with pembrolizumab, with palliative intent. One month following immunotherapy, the patient was enrolled in neutron radiation therapy. A total of 5 lesions were treated with 6 Gy of fast neutrons, delivered in two fractions of 3 Gy, one week apart. Within two weeks, all treated lesions had completely responded, as well as the out-of-field lesions (Figure 1). Nine months following radiation, this patient remained disease-free.

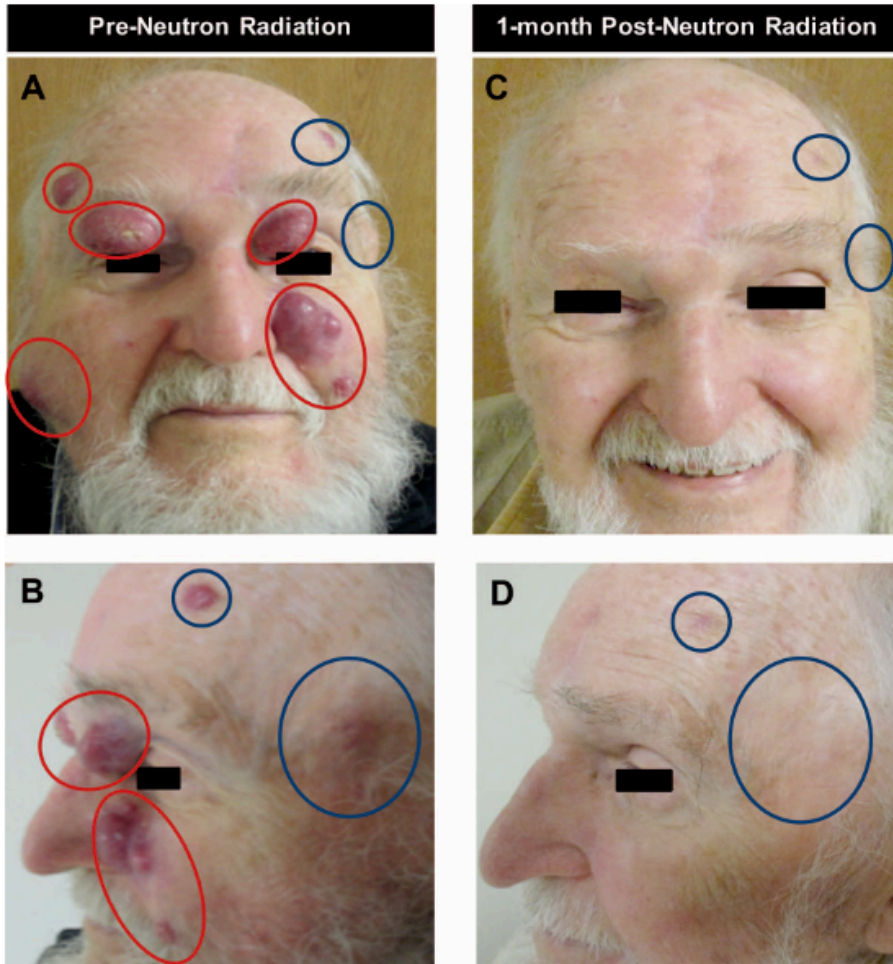


Figure 1. An MCC patient receiving a combination of neutron beam therapy and immunotherapy (anti-PD1). A+B show the lesions directly treated with neutrons by two fractions of 3 Gy, circled in red. The blue-circled lesions were not directly treated. C+D show the patient at one month following treatment, showing complete remission. Photo from Schaub et al. (2019)

Another patient was diagnosed with recurrent MCC of the scalp, previously treated with anti-PD1 immunotherapy and megavoltage x-ray (low-LET) radiotherapy²³. Neutron radiotherapy was administered, with a total of 18 Gy delivered in 12 fractions over four weeks to all disease sites, resulting in a complete clinical response. Small out-of-field lesions developed within 6 months of treatment completion, which were treated with various immunotherapy drugs (anti-PD1, toll-like receptor 4 agonist). Following treatment with anti-PD1, secondary lesions completely responded. Five years after treatment, this patient remains free of recurrent MCC.

In cases like these, the patients were previously unresponsive to low-LET radiation or immunotherapy alone, and only experienced full therapeutic control when treated with both high-LET radiation and immunotherapy. This suggests that synergistic effects can occur when treatments are combined, and that x-ray radiotherapy may be less suitable to stimulate an immune response than higher-LET radiotherapy. Immunotherapy is designed to make the tumor environment more susceptible to immune surveillance. Thus, particularly high-LET, radiation must be acting to enhance antigen production from the cancer cells.

1.3 Stimulator of Interferon Genes

Immune recognition in response to DNA damage is a concept that traces back to virology. DNA viruses, such as herpesvirus and papillomavirus, chiefly act to invade the nuclei of cells, induce DNA damage, and integrate with the host DNA during repair²⁷. Immune surveillance does not extend to the nuclei of eukaryotic cells; another means of detection is needed.

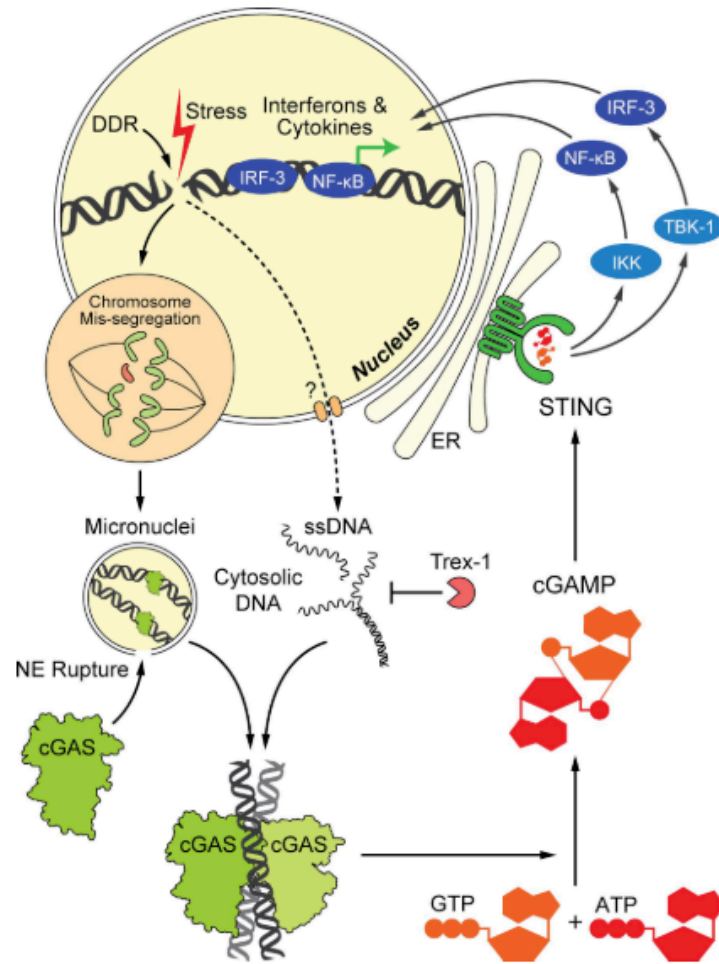


Figure 2. The cGAS-STING signaling pathway. DNA stress leads to cytosolic DNA accumulation by micronucleus formation and rupture. DNA is sensed by cGAS and used to activate transcription factors IRF3 and NF-κB, leading to production of inflammatory cytokines. Figure from Li et al. (2018)

The Stimulator of Interferon Genes (STING) pathway evolved such that cells can detect and respond to DNA viral infections (Figure 2)²⁸. Through STING, infections are detected by double-stranded DNA fragments left behind by viral invasion and DNA integration, either by directly diffusing outside of the cell's nucleus or through formation of unstable micronuclei, which both deliver DNA into the cytosol²⁹. DNA detection is performed by cyclic GMP-AMP synthase (cGAS). cGAS binds to dsDNA fragments with GMP/AMP to create cyclic GMP-AMP (cGAMP). cGAMP has the unique capability of interacting and phosphorylating STING receptors on the cells' endoplasmic reticulum, which then ignites a series of pro-inflammatory signals³⁰. Activated STING dimers translocate to the perinuclear space through Golgi apparatus, which goes on to

phosphorylate tank-binding kinase-1 (TBK1)³¹. TBK1 activation leads to nuclear transcription NF- κ B (nuclear factor light-chain-enhancer of activated B cells) and IRF3 (immune regulatory factor 3). NF- κ B and IRF3 both drive production of type-I interferon, such as interferon-beta (IFN β), which is known to promote immune-stimulatory functions and enable activation of innate immune responses through dendritic cells, CD8⁺ T-cells, and natural killer cells³¹.

Once expressed, IFN β acts as a danger signal to the surrounding immune system and is detected by tumor-infiltrating lymphocytes, such as dendritic cells³². Dendritic cells seek out pathogen or damage-associated molecular patterns (PAMP/DAMP), i.e. tumor antigens, expressed on the cell surface of dying cells through class-I major histocompatibility complexes (MHC-1)^{31,33}. Upon detection, these antigens are converted into peptides expressed on the dendritic cell's surface, which is able to cross-present the tumor antigens to MHC-1 on naïve CD8⁺ (killer) T-cells. By this action, CD8⁺ T-cells become primed to a target. This cascade of interactions following IFN β production unleashes killer T-cells that are able to recognize target cells that are positive for the original DAMP³⁴.

Although newly discovered, this signaling pathway has been extensively studied *in vivo* and *in vitro*, chiefly by scientists at Weill-Cornell with respect to radiation-induced STING. A 2017 Nature Comms manuscript³⁵ described the dose response mechanics of cytosolic dsDNA accumulation in a range of human and murine cancers, demonstrating high accumulation of dsDNA and IFN β production between 8-12 Gy of x-ray radiation. In-vivo studies of combined radiation and PD1 inhibitors in mice, showed remarkable tumor control in un-irradiated contralateral flank tumors at 8 Gy. However, these effects are not present when absorbed doses exceed 12 Gy. In-vivo studies combining anti-CTLA4 and fractionated ionizing radiation in dual-flank B16 melanoma tumors have shown an abscopal effect with single-fraction doses ranging from 5-8 Gy, with little dependence on the timing between fractions³⁶. Blocking CD8 abrogates the pro-immunogenic response, further confirming that these effects are immune-mediated.

While hypofractionated radiation has been shown to be pro-immunogenic, the single-fraction dose can have a dramatic effect on immunogenicity, especially at doses exceeding 12 Gy.³⁵ As an excess of dsDNA accumulates in the cytosol and IFN β is secreted at high

concentrations, the genotoxic stress drives the cell to begin upregulating three-prime-five-prime exonuclease 1 (Trex1), which acts as an inhibitory signal to degrade cytosolic dsDNA. Not much is currently known about the mechanism of Trex1 upregulation and its role as a STING antagonist, whether it is a direct responder to cytosolic dsDNA is debated³⁷. However, Trex1 deficiencies in mice and humans comes with high rates of autoimmune disorder³⁸. This suggests that Trex1 is, at least, immunosuppressive and a mechanism of autoimmune disease.

1.4 DNA Damage and Repair

In the current understanding of radiation biology, nuclear DNA is the primary target for the biological effects of ionizing radiation³⁹. Radiation-induced DNA damage can manifest in four discrete ways: base damages, DNA protein crosslinks, mismatches, and strand breaks. Base damages refer to individual DNA bases (A, T, G, C) being covalently modified into another. Crosslinks refer to covalent links forming between DNA bases, either inter-or-intra strand. Mismatches refer to base pairs being repaired with the incorrect bases, commonly T being replaced for U. Lastly, strand breaks refer to breaks in the sugar-phosphate ‘backbone’ of DNA and can be classified as single (SSB) or double-strand breaks (DSB).

SSB and DSB are the most relevant forms of DNA damage leading to clonogenic cell death, with the latter being the most potentially lethal form of DNA damage. Roughly 1000 SSB and 40 DSBs occur per Gy of radiation dose per cell, which are induced by either ‘direct’ or ‘indirect’ action^{40,41}. Indirect action refers to DNA damage induced secondarily following physiochemical interactions of low linear energy transfer (LET) particles with other molecules in a cell, chiefly mediated by hydroxyl radicals created through water radiolysis. Radical-DNA interactions can be chemically repaired through reactions with sulfhydryl groups, but the presence of oxygen molecules make these damages permanent (oxygen fixation)³⁹. Direct action refers to DNA damage induced directly by ionization interactions between radiation and DNA. Indirect action is the dominant interaction mechanism for radiation with a low linear energy transfer (LET), such as x-rays or electrons. Conversely, high-LET radiation (heavy ions, neutrons) predominantly interacts through direct action.

Different forms of DNA damage can be repaired through distinct repair pathways (Figure 3)^{39,42}. SSB are generally repaired through the process of base-excision repair or nucleotide-excision repair, where sections of damaged bases are excised and re-filled by polymerases and ligases. DSB are repaired through homologous recombination repair (HRR) or non-homologous end joining (NHEJ), depending on cell cycle staging and the presence of homologous chromosomes. HRR occurs in the S/G2 phases of the cell cycle, with higher rates of successful repair due to the presence of sister chromosomes to use as a template. However, NHEJ is the more predominant DSB repair mechanism, where damaged ends are directly rejoined by DNA protein kinases. The accuracy of the repair is dependent on the nature of the breaks – perfectly-matched overhangs can be successfully repaired, but imperfectly-matched overhangs suffer from nucleotide loss at repair. Imperfect matches are more common, thus NHEJ is more error prone. It should be noted that flawed DNA repair is not inherently lethal but can result in DNA translocations that are mutagenic and carcinogenic.

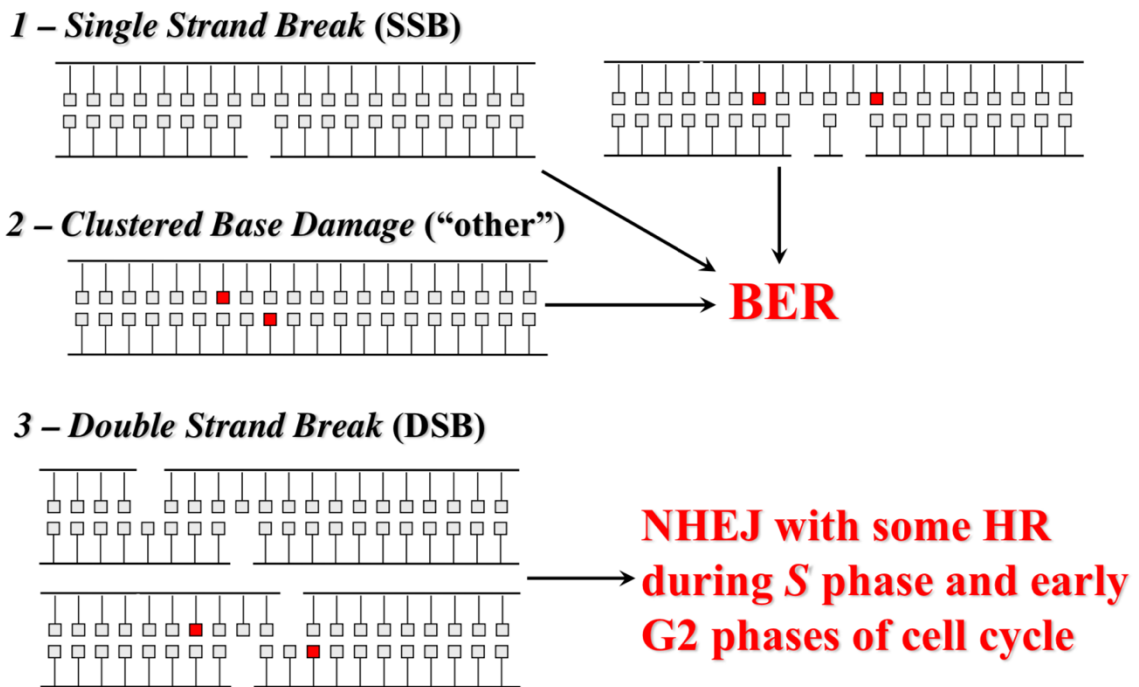


Figure 3. Summary of DNA damage induced by ionizing radiation, and repair mechanisms for each. Single strand breaks and base damages are repaired through base-excision repair (BER). Double strand breaks, whether clustered or base damage-adjacent, are repaired through homologous repair (HR) during S/G2, and non-homologous end joining (NHEJ) during the rest of the cell cycle. Figure from R. Stewart lecture on DNA repair, Univ. of Washington resident didactics (2019)

1.5 Hypoxia in Radiation Therapy

Oxygenation plays a large role in the radiosensitivity or radioresistance of cancer, particularly for low-LET radiation that induces DNA damage by indirect action (Figure 4). Oxygen ‘stabilizes’ the damaged ends of DNA strands from hydroxyl radicals, making them more difficult to repair⁴³. As oxygen is removed, DNA lesions remain less stable and radiosensitivity decreases⁴⁴. At anoxia, low LET radiation requires roughly 3x more dose for equivalent clonogenic death⁴³. Directly ionizing radiation, such as high-LET charged particle beams is able to overcome heightened radioresistance by directly damaging DNA⁴⁵.

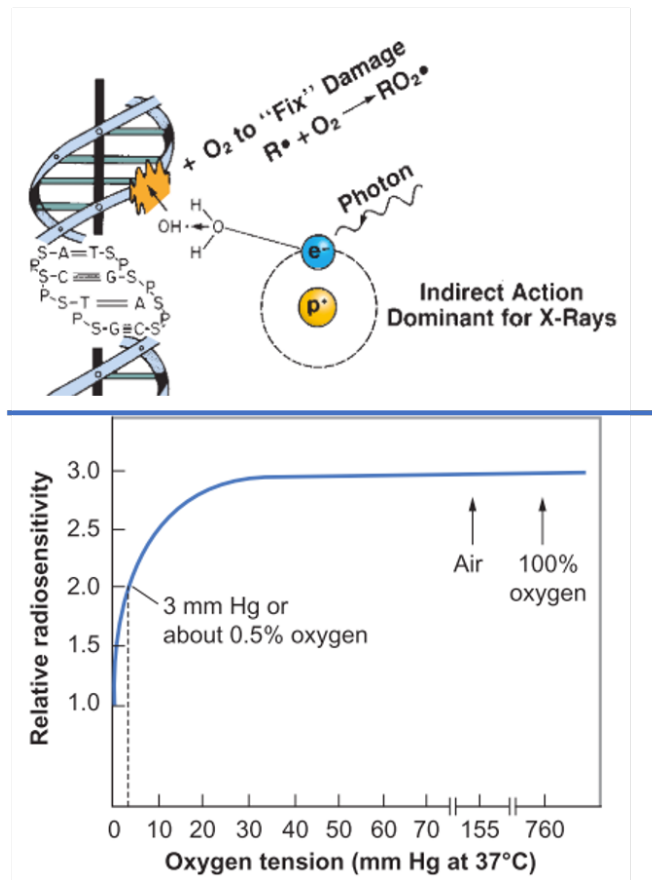


Figure 4. (Top) The mechanism of oxygen fixation of radiation-induced DNA damage. DNA damage from indirect action relies on free radicals produced in water radiolysis, which are conventionally ‘fixed’ by chemical reactions with oxygen. When oxygen is removed, this fixation is no longer possible. (Bottom) The effect of oxygenation on radiation sensitivity. Fully oxygenated cells are roughly three times more radiosensitive than fully anoxic cells. Figures from the 7th edition of Radiobiology for the Radiologist (Hall, Giacca; 2012).

Hypoxia impacts many other mechanisms than DNA damage and repair. Disordered tumor growth and dysfunction in angiogenesis and vasculogenesis result in the deprivation of oxygen to tumor cells, with differential effects that vary over space and time (Figure 5)⁴⁶⁻⁴⁸. Briefly, as a result of chaotic growth, some regions within a tumor grow beyond the diffusion length of oxygen from native vasculature, resulting in a limitation of oxygen diffusion (chronic) hypoxia. This oxygen deprivation promotes accumulation of hypoxia-inducible factor alpha subunits (HIF-1a and HIF-2a) and formation of HIF transcription factors, resulting in upregulation of VEGF and chaotic formation of neovasculature (angiogenesis)⁴⁸. Disordered and ‘leaky’ vasculature can yield in a different form of hypoxia, where delivery of O₂ is transient and limited by fluctuations in blood vessel perfusion (acute hypoxia)⁴⁹.

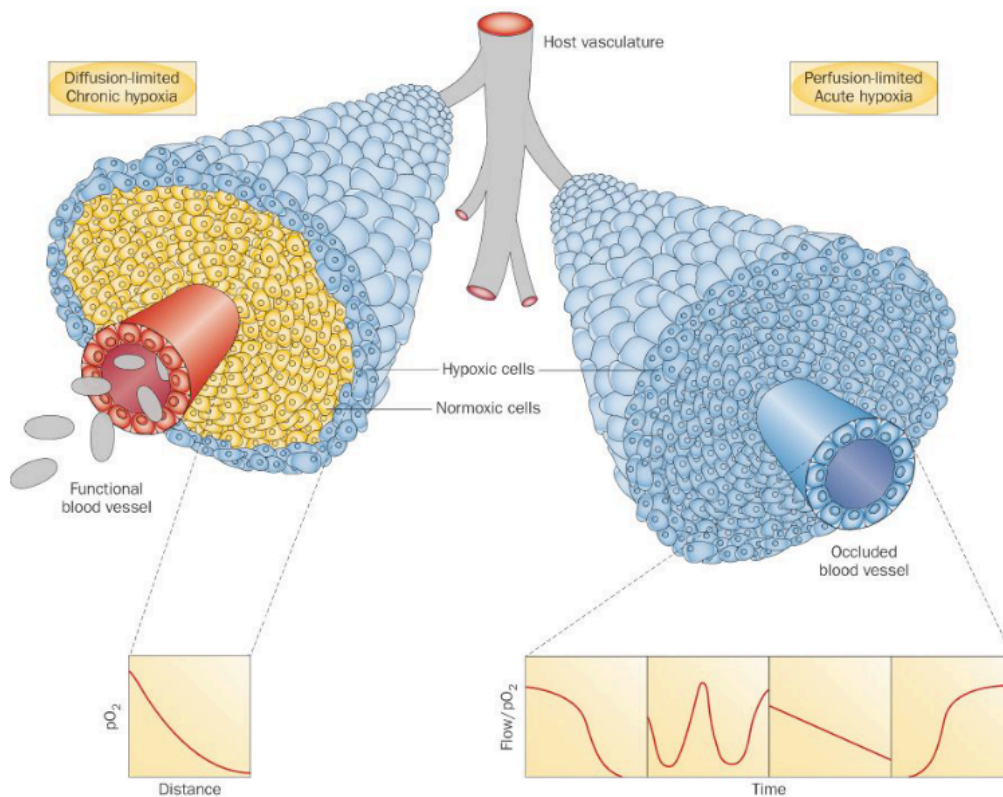


Figure 5. The effects of limitations in oxygen perfusion and diffusion on hypoxic status. Hypoxic cells are illustrated in blue, normoxic cells in yellow. Chronic hypoxia (left) occurs in cells that reside beyond the diffusion length of oxygen from blood supply, dependent on the distance away from a blood vessel. Acute hypoxia occurs in cells that reside near an occluded blood vessel, which is occasionally perfused with blood, leading to oxygenation that varies with time. Figure from Horsman et al. (2013)

Tumor cells in acutely hypoxic conditions have been shown to undergo epithelial-to-mesenchymal transformation, changing their own morphology to become more motile and less susceptible to environmental stressors⁵⁰. Many known EMT mechanisms have been linked to acute hypoxia, such as Snail, Twist, Hedgehog, and Notch⁵¹. Chronically hypoxic regions of tumors become focal regions of mesenchymal stem-like cells, accompanied by changes in metabolic activity (Warburg effect), elevated stem cell maintenance factors, and elevated immunosuppressive factors⁵². Both subgroups can be attributed with treatment resistance in radiation, chemotherapy, and immunotherapy regimens, and yield subpopulations of cells with enhanced capacity of metastasis and recurrence.

1.6 Hypoxia Imaging, Photoacoustic CT

Intratumor measurement of tissue oxygenation has clinically been performed using a variety of techniques, each with their own strengths and weaknesses. The gold standard for interstitial oxygen measurement is the Eppendorf probe, which offers absolute measurements quickly, at the cost of invasiveness and limited spatial sampling⁵³. Many PET/SPECT tracers have been developed, relying on nitroimidazole binding to intermediate products of formed during hypoxic reactions in cells⁵⁴. However, nitroimidazole-positive voxels have poor correlation with hypoxic cells measured via HIF-1/2 histopathology⁵⁵. PET/SPECT scans also suffer from long acquisition times, artificially skewing readings to predominantly bias toward chronic hypoxia. Dynamic contrast-enhanced MRI is another common approach to hypoxia imaging, which can give volumetric data on vascular perfusion at high resolutions, but this only gives an instantaneous view of perfusion – which is only one contributing factor to chronic hypoxia and varies over time in acute hypoxia⁵⁵. Multiple perfusion images would be required to demonstrate changes in perfusion. In a preclinical setting, many of these issues can be overcome through the use of photoacoustic CT spectroscopy (PCT-S).

Photoacoustic imaging utilizes the photoacoustic effect, first described by Alexander Graham Bell, which relies on the conversion of electromagnetic energy into high-frequency acoustic pressure signals in tissue⁵⁶. This conversion is the result of rapid thermal expansion and contraction that follow energy absorption, which occurs on the order of microseconds⁵⁷. Photoacoustic imaging systems typically utilize nanosecond pulses of light, considered

instantaneous, to ensure that all absorption interactions complete before energy absorption can be converted into acoustic pressure. Conventionally, these light sources are near-infrared lasers, chosen because long-wavelength light is able to more-easily penetrate into tissue for imaging of structures at a greater depth⁵⁸. The resulting acoustic signals are emitted isotropically, and can be detected with ultrasound transducers, either singly or by an array of transducers⁵⁹. By applying filtered backprojection techniques to photoacoustic measurements acquired at many angles, cross-sectional photoacoustic computed tomography (PCT) can be achieved. Modern photoacoustic systems can be designed at the scale of single cells (PCT-microscopy) or for whole-breast imaging (photoacoustic mammography)⁶⁰. The PCT system used in the lab of Dr. Keith Stantz typically acquires images at a resolution of 0.15 mm voxels, with an acquisition time of 3-12 seconds.

At near-infrared wavelengths, the main endogenous absorbers of EM radiation are oxyhemoglobin and deoxyhemoglobin (Figure 6), which have absorption cross sections 2-3 orders of magnitude higher than water or fat⁶¹. The presence of oxygen on hemoglobin alters its absorption spectrum. By acquiring PCT images at varying NIR wavelengths, the resulting signal can be fit to the molecular extinction coefficients for oxygenated and deoxygenated hemoglobin to determine the hemoglobin concentration and the oxygen saturation of hemoglobin⁶².

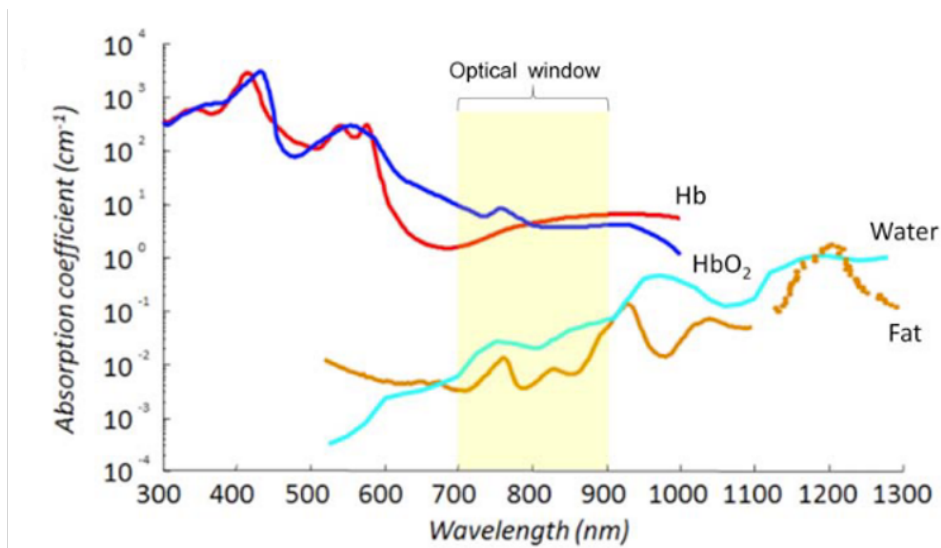


Figure 6. Optical absorption coefficients for hemoglobin, water, fat as a function of photon wavelength. At near-infrared wavelengths (shaded in yellow), the main absorbers of photons are hemoglobin (Hb) and oxyhemoglobin (HbO₂). Near-infrared light also interacts in water and fat, but the absorption coefficients are 3 orders of magnitude lower than hemoglobin. Figure from Mehrmohammadi et al. (2013)

The main limitations of the clinical hypoxia imaging techniques described above are invasiveness, poor time resolution, poor spatial resolution, and the need for vascular perfusion. PCT-S is a single imaging modality that is able to noninvasively measure oxy/deoxyhemoglobin concentrations and oxygen saturations quickly and with a high spatial resolution. Repeat scans require no extra injection of perfusion agents, so changes in tissue oxygenation can be readily tracked over time, differentiating between acute and chronic hypoxia.

1.7 Hypothesis

Current techniques used in radiation therapy simplify a complex biological problem into a physical problem – where anatomical imaging is used to identify and treat a large tumor volume with a uniform radiation dose. While largely successful, local and distant recurrence occurs in many cancers leading to poor overall survival rates. Many of these recurrences can be attributed to treatment-resistant sub-populations of transformed mesenchymal cells, which are known to be maintained within hypoxic regions of the tumor and to evade immune-surveillance. By accounting for immunogenic (biological) effects, such as radiation-enhanced immunogenicity via the STING pathway, concurrent radiation and immune therapies can potentially be implemented to induce an abscopal response, selective to these hypoxic cells with the highest metastatic potential. As this response is dependent on DNA damage, x-ray radiation at clinically viable doses is likely insufficient due to oxygen-enhancement effects. Therefore, we believe that high-LET radiation, which is able to overcome oxygen enhancement effects, is capable of selectively inducing this adaptive immune response to metastatic and recurrent cancers.

Little prior work has been done to explore STING induction by high-LET radiation, in part due to the limited accessibility of clinical heavy ion beam therapy. Therefore, we will initially use DNA damage modeling to develop a predictive model of STING regulators (cytosolic dsDNA and TREX1) as a function of physical dose and Σ (the initial number of DSB clusters per Gy). We hypothesize that hypoxia will reduce the efficiency of low-LET radiation of inducing STING via these regulators, and that high-LET radiation will both more efficiently trigger STING and abrogate oxygen-enhancement effects.

These models will be based purely on physical modeling and require experimental verification. As previously described, the CNTS at the University of Washington is one of the few clinics in the world capable of treating with high-LET external beam radiation, and MCC have a clinical history of inducing abscopal effects in response to neutron therapy. Through direct in vitro testing of MCC cells, we further hypothesize that high-LET fast neutrons will be more efficient per dose at inducing STING than low-LET x-rays. This will be tested through the assay of IFN β secretion, cytosolic dsDNA accumulation, and Trex1 upregulation. Laboratory measurements will be used for refining and extending these DNA damage models to predict STING response.

Lastly, advanced imaging will be required to support the selective targeting of hypoxic regions within a tumor harboring cancer cells with the highest metastatic potential. Novel in-vivo oxygenation imaging techniques will be developed using photoacoustic CT to identify normoxic and hypoxic regions of these tumors for guidance in focal radiation delivery. We hypothesize that chronic and acute hypoxia can be both detected and distinguished based on longitudinal sampling of local hemoglobin concentration and oxygen saturation.

CHAPTER 2. SPECIFIC AIMS

2.1 Model STING Regulation from DNA Damage Models

In vitro data has been published on cytosolic dsDNA concentrations and exonuclease Trex1 expression as a function of radiation dose from 220 kVp x-rays for MC38 cancer cells. Using Monte Carlo Damage Simulation (MCDS)⁴⁰ software with a single-cell geometry, the number of nucleic double-stranded DNA break clusters (DSB per Gy) will be calculated for the published doses and fitted to form simple models of DSB vs. dsDNA concentration and DSB vs. Trex1 upregulation parameters. These models of dsDNA accumulation and Trex1 upregulation will be applied to new MCDS simulations varying the radiation source (220 kVp and 6 MV photons, protons, alpha particles, fast neutrons) and oxygenation conditions ($pO_2 < 20$ mmHg), assuming that equivalent nuclear DNA damage yields equivalent STING activation.

2.2 Measure STING Regulation from Varying Radiation Sources

Experimental validation of x-ray and fast neutron models will be performed through in vitro study using MCC13 non-viral Merkel cell carcinoma cells⁶³ (courtesy of Paul Nghiem Lab, University of Washington) using the Small Animal Radiotherapy Research Platform (SARRP) and Clinical Neutron Therapy System (CNTS) at the University of Washington. Dose escalation studies will be performed using cells plated and irradiated at a comparable confluence to the reference experiments. STING activation will be determined through two endpoints: IFN β secretion and Trex1 upregulation. Trex1 upregulation will be measured using immunofluorescence techniques. IFN β secretion in cell-free supernatant will be measured through ELISA assay. Agreement with our DNA damage models will be assessed, and if necessary, our models will be revisited to match measurement.

2.3 Develop Imaging Protocols to Localize and Distinguish Hypoxic Status

Syngeneic MC38 colorectal tumors will be seeded onto immune-competent mice and tracked for two weeks of growth. Tumor volumes will be measured throughout development, and photoacoustic CT spectroscopy scans will be performed to track changes in oxyhemoglobin

saturation (SaO₂) and concentration (CtHb). Every three days, a series of PCT-S images will be acquired in 15-minute intervals over 2 hours to measure short-term fluctuations in SaO₂ and CtHb. Temporal data will be used to develop a classification system for sub-regions of predominantly chronic or acute tumor hypoxia.

2.4 Innovation and Impact

Adjuvant radiation and immunotherapy is a rapidly growing focus of radiation oncology, yet cGAS/STING/Trex1 are a relatively new discovery. As of writing, no groups have explored the variability in STING-driven immunogenicity due to high-LET radiation or hypoxia, which are common points of study within radiation biology and dramatically impact initial DNA damage, repair, and clonogenic survival. This work aims to bridge the gap between radiation oncology and immunology through a preclinical approach, utilizing both Monte Carlo radiation transport modeling and laboratory experiment, to establish the basic groundwork for clinical translation.

CHAPTER 3. DNA DAMAGE MODELING OF STING RESPONSE IN VARYING CONDITIONS, *IN VITRO*

3.1 Introduction

Radiation-induced immunogenicity, particularly from accumulation of cytosolic dsDNA activating STING, is mediated by micronucleation and DNA fragmentation following DNA damage³⁰. This suggests that study of radiation damage may yield further details about the mechanism of radiation-enhanced immunogenicity. Laboratory experiments of cGAS-STING-Trex1 are conventionally performed using low-LET x-ray radiation sources, such as an Xstrahl SARRP, in normoxic conditions, and have demonstrated a strong pro-immunogenic response following doses of 8-12 Gy³⁵. However, the effects of varying radiation quality and tissue oxygenation remain largely unexplored.

High-LET radiation sources produce more dense ionization interactions, yielding more geometrically complex DNA damage that is more difficult to repair, which can lead to higher rates of micronucleus formation per dose^{64,65}. Thus, radiation that is more extensively damaging is predicted to be more immunogenic. In contrast, as previously described, oxygen deprivation can render cancer cells unresponsive to (particularly, low-LET) radiation due to the lack of chemical fixation of indirect DNA damage by oxygen, enabling chemical repair. The purpose of this chapter is to use Monte Carlo radiation interaction simulation techniques to develop preliminary models of the DNA damage induced in published experiments on STING regulation. These models are then applied to other forms of radiation, as well as conditions of varying cellular oxygenation.

3.2. Materials and Methods

3.2.1 Monte Carlo Damage Simulation

Monte Carlo damage simulation (MCDS), originally developed in 2004 at Purdue University by Stewart and Semenenko, a modeling software capable of simulating the formation of single and multiply damaged sites on DNA for an arbitrary radiation source⁴⁰. Briefly, the software inputs a radiation type and particle energy, either mono-energetically or poly-energetic spectrum, and determines the number of SSB, DSB, and base damages. MCDS randomly

distributes DNA lesions over both strands for a pre-defined length of DNA. Following ‘damage,’ MCDS parses through the length of the modeled DNA strand and groups DNA lesions into damage clusters based on their proximity, with a minimum separation that can be defined as an input (Figure 7)⁶⁶. Clustered damages are classified using the scheme defined by Nikjoo et al.⁶⁷, loosely into SSB and DSB with varying complexity depending on other local damages, such as SSB+ (multiple adjacent SSB on the same strand) or DSB++ (multiple adjacent DSB). One particularly useful output is Σ , the number of DSB/Gy/Gbp, which can be used to define the RBE with respect to DSB formation (Eqn 3.1)⁶⁸. Conventionally, Σ_{ref} corresponds damage from a cobalt-60 radiation source.

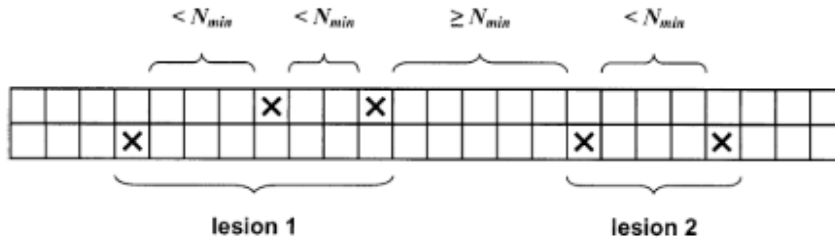


Figure 7. Example of DNA lesion distribution and clustering across two strands of DNA, as modeled in MCDS. N_{min} refers to the minimum separation for two lesions to be considered of separate clusters. Lesion 1 consists of a DSB with a nearby SSB. Lesion 2 consists of two SSB on the same strand. Figure from Stewart et al. 2004

$$RBE_{DSB} = \frac{\Sigma_{test}}{\Sigma_{ref}} \quad (3.1)$$

MCDS is the only DNA damage modeling software capable of accounting for oxygenation effects⁶⁶. To achieve this, the probability of DNA fixation by an oxygen molecule within a cell is calculated based on the local oxygen concentration, the number of DNA lesions chemically fixed in oxygen-depleted (anoxic) irradiations, the oxygen concentration at which half of the maximum DNA lesions are removed, the effective atomic number of the radiation source, and the velocity of the particles relative to the speed of light. This oxygenation correction also accounts for physiochemical processes that inhibit chemical DNA repair. Once the probability of oxygen fixation is determined, the total number of modeled DNA lesions are reduced by this probability,

and the DNA damage clustering algorithm proceeds as described above. This approach has been validated against in-vivo and in vitro data for a variety of cell lines and closely agrees with oxygen enhancement effects. By directly calculating the probability of chemical repair, effects of oxygen radical scavengers can also be modeled, although this is not explored within the context of this work.

3.2.1.1. Source Modeling: X-Rays

MCDS modeling for photon sources requires tabulated data of the relative dose contribution of secondary electrons for a given setup – here modeled as a cell monolayer with 1 cm of water buildup with 20 cm of water for backscatter. All beam modeling was performed in FLUKA general purpose Monte Carlo PRECISIO defaults, with 10^8 histories and electron transport cutoffs reduced to 1 keV^{69,70}.

A 220 kVp x-ray source was modeled to match a Varian NDI 225/22 x-ray tube typical of SARRP orthovoltage irradiators (Figure8), as described in Stewart et al²⁶. Briefly, a 220 keV electron pencil beam was directed at a tungsten wedge at 45-degrees to the beam. A brass filter of 0.8 mm thickness was added to remove low-energy photons and increase the average energy of the resulting beam. The surface of the simulated cell plate was positioned at 35 cm from the brass filter to match the exact radiation geometry. Parallel simulations were performed using 10-million primaries, scoring the dose contribution of secondary electrons as a function of particle energy. This dose spectrum was tabulated as an input file for MCDS simulations.

A 6 MV x-ray source was modeled to match a Varian Clinac. Geometric models of the treatment head components were not available, so the source photon energies were defined using customized FLUKA SOURCE.f subroutine and a photon fluence spectrum provided with the Computational Environment for Radiotherapy Research (CERR) VMC++ modeling package⁷¹. The cell monolayer geometry was maintained from the prior simulation, with the SSD changed to 100cm. Simulation parameters were kept consistent, and the resulting electron dose spectrum was tabulated as an input file for MCDS.

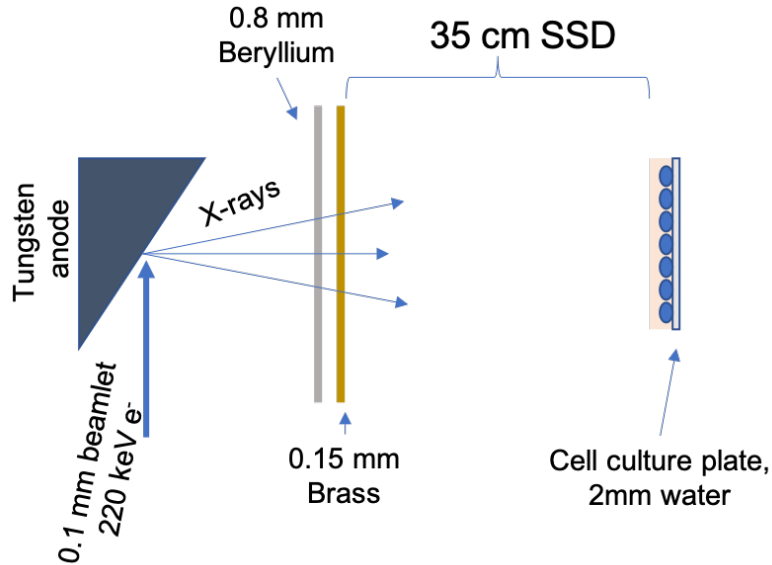


Figure 8. FLUKA simulation geometry to calculate the secondary electron fluence following exposure to 220 kVp x-rays. A 0.1-mm diameter beamlet of 220 keV electrons are directed at a tungsten anode, creating bremsstrahlung and characteristic x-rays that propagate out. The resulting x-rays pass through a 0.8 mm beryllium window and a 0.15 mm brass foil to attenuate low-energy x-rays. At 35 cm away from the source, a cell culture plate is placed, where secondary electrons are measured after passing through 2 mm of water.

3.2.1.2. Source Modeling: Charged Particle Beams

MCDS by default can model DNA damage from monoenergetic charged particle sources for ions up to Fe56 without further external definition of the source properties. Due to the immense variability in energy spread among ion beams, across systems, across primary energies, and across depths, iontherapy sources were modeled as monoenergetic⁷². These energy spreads can be modeled in general purpose Monte Carlo and used to calculate DNA damage on a voxel-by-voxel basis. This will be discussed and demonstrated in Chapter 4.

3.2.2 Retrospective Analysis

The in vitro dose response characteristics of STING regulators cytosolic dsDNA and exonuclease Trex1 have been published by Vanpouille-Box³⁵ for a variety of human and murine cells, where cell plates were irradiated to doses up to 30 Gy. The endpoints of Trex1 upregulation and cytosolic dsDNA accumulation were assayed using RT-PCR and fluorescence techniques,

respectively. To generalize these results for use in predicting radiation-enhanced cytokine production, MCDS simulations were designed to calculate the extent of DNA damage from the absorbed doses delivered to each data point.

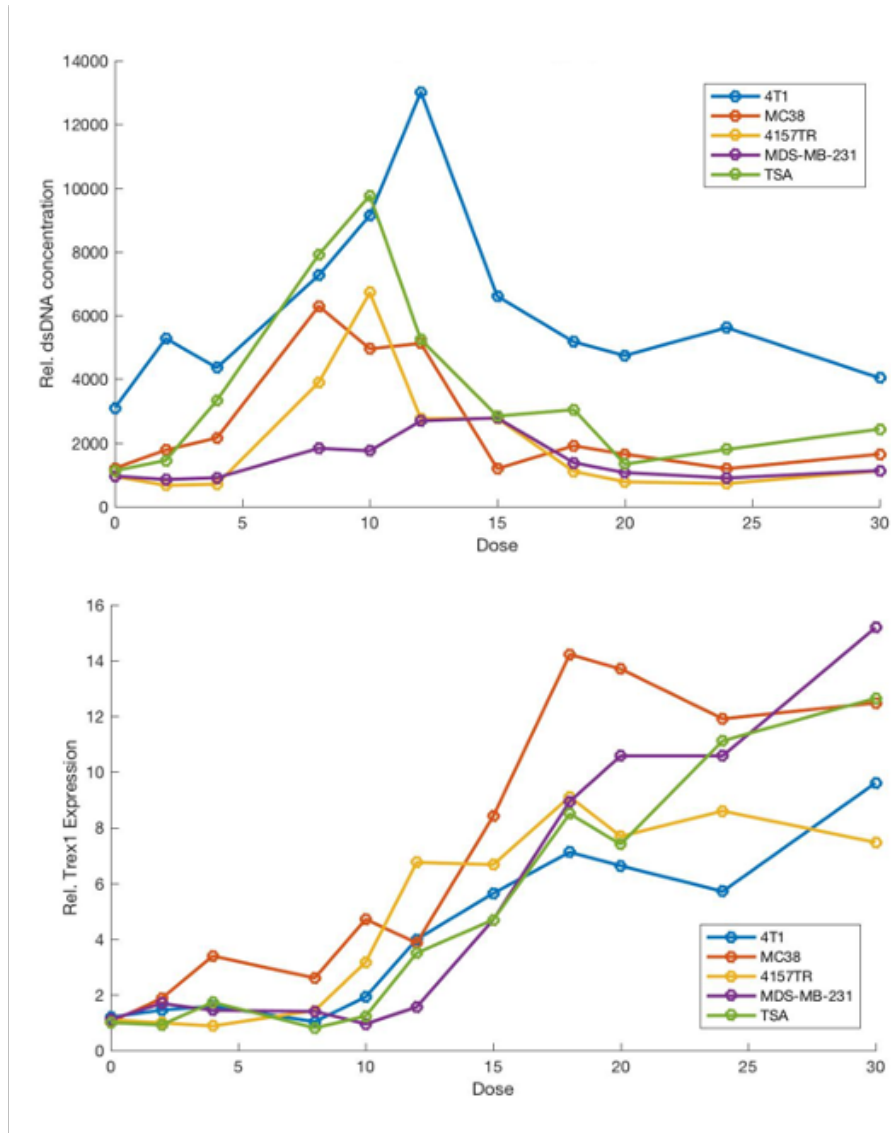


Figure 9. Published data for cytosolic dsDNA and Trex1 dose response from Vanpouille-Box et al. (2017) for a variety of human (MDS-MB-231, 4157TR) and murine (4T1, MC38, TSA) cells. Cytosolic dsDNA (top) follows a Gaussian trend, with varying amplitude and background concentrations per cell type. Trex1 (bottom) roughly follows a sigmoidal trend, with varying ‘plateau’ amplitudes.

The referenced experiment was assumed to use cells in normoxic conditions at 20mmHg, with each cell type modeled using the default nucleus diameter at 5 microns and the default DNA

content of 1 giga-base pairs. Simulations were performed using a SARRP 225kVp photon source, for doses between 0-30 Gy. The number of DSB clusters per unit dose were plotted against the published data for nanograms of cytosolic dsDNA per 10⁶ cells, and n-fold upregulation of Trex1. Data was fitted to Gaussian and Sigmoid curves (Eqn. 3.2 and 3.3) using the MATLAB curve fitting toolbox (MathWorks, Inc.). In equations 3.2 and 3.3, D represents the physical absorbed dose in Gy, Σ is the number of DSB clusters per Gy, and a/b/c are cell-specific constants.

$$selfDNA(D, \Sigma) = a * \exp \left[- \left(\frac{D * \Sigma - b}{c} \right)^2 \right] (ng) \quad (3.2)$$

$$Trex1(D, \Sigma) = \frac{a}{b + \exp(-c * D * \Sigma)} (n - fold \ upregulation) \quad (3.3)$$

These fitted models were applied to new test scenarios, under the assumption that equivalent DNA damage will yield equivalent micronucleation and cytosolic self-DNA accumulation, thus equivalent IFN β and Trex1 regulation. MCDS simulations for the reference cells were repeated to determine Σ for 6MV x-rays, as well as protons, electrons, helium-4, and carbon-12 ion sources with particle energies varied between 1 keV and 300 MeV. Further simulations were performed for cells held in hypoxic and anoxic conditions, from pO₂ = 0 – 20%.

3.4 Results

3.4.1 Predicted Effects of High-LET Radiation on STING Regulation

Prior data follows gaussian and sigmoidal models with all R² > 0.9. Fit coefficients for dsDNA and Trex1 dose responses can be seen in Table 1, Monte Carlo damage coefficients in Table 2 Variability in peak dsDNA amplitudes, as well as background dsDNA concentrations, are considered cell specific. Higher-LET radiation induces more DSB/Gy, thus cytosolic DNA is expected to accumulate at lower doses (Figure 10). Similarly, exonuclease Trex1 is upregulated at lower doses. The ratio of peak doses between radiation modalities follows the RBE, with respect

to DSB induction. E.g., 1 MeV protons at the distal edge of a pristine Bragg peak have an RBE of approximately 2, which induces a dsDNA peak at $\frac{1}{2}$ of the low-LET dose.

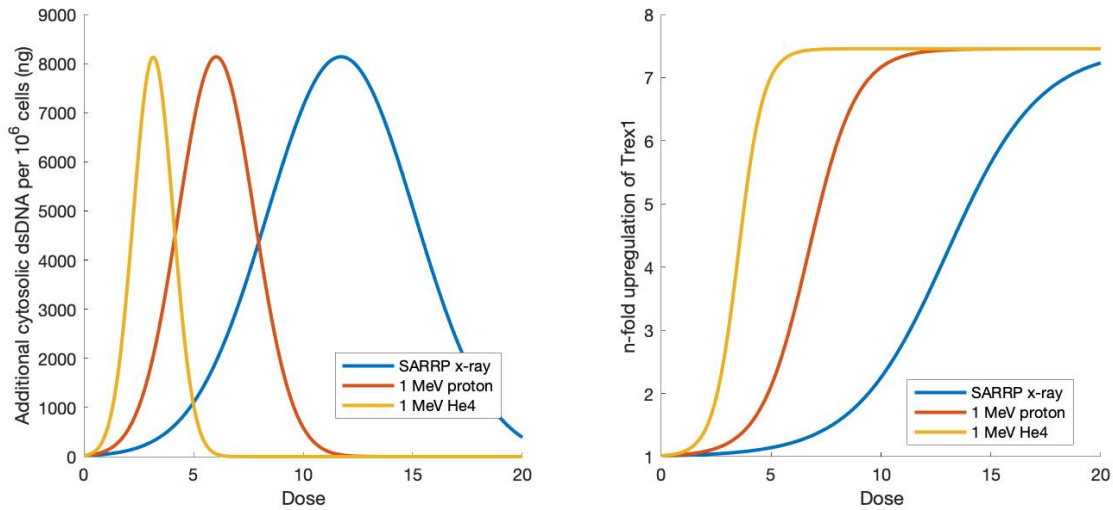


Figure 10. Predicted cytosolic dsDNA accumulation following radiation with SARRP x-rays, monoenergetic 1 MeV protons, and monoenergetic 1 MeV helium ions. Higher-LET radiation induces more DSB per Gy, resulting in accumulation of cytosolic dsDNA at lower doses (left). The ratio of doses for peak cytosolic dsDNA is the ratio of Σ between sources, i.e. the RBE_{DSB} . The rapid buildup of dsDNA followed by upregulation of Trex1 at lower doses (right).

Table 1. Fit coefficients for a variety of human and murine cells for cytosolic dsDNA and Trex1 dose response as a function of physical dose and the number of DSB clusters per Gy, as modeled in MCDS. Fits were performed using the MATLAB curve fitting toolbox. Cytosolic dsDNA fits used the built-in Gauss1 equation (3.2). Trex1 data was fitted to a sigmoid function (3.3)

	TSA		4T1		MC38		MDA-MB-231		4157TR	
	dsDNA	Trex1	dsDNA	Trex1	dsDNA	Trex1	dsDNA	Trex1	dsDNA	Trex1
a	7851	0.09298	4875	0.02935	8139	0.01356	1998	0.01484	6085	0.0001653
b	66.47	0.03802	65.67	0.06231	85.14	0.06531	96.26	0.05376	70.82	0.1379
c	31.76	0.007728	31.57	0.00239	34.52	0.002099	33.97	0.001166	16.13	0.00002334
R²	0.9	0.97	0.9	0.93	0.74	0.9	0.91	0.96	0.87	0.97

Table 2. DNA damage coefficients calculated in MCDS for a variety of radiation sources, varying oxygenation. Photon sources were input as polyenergetic secondary electron spectra, calculated using FLUKA particle transport Monte Carlo. Electron, proton, and helium ion sources were input as monoenergetic for simplicity, due to range dependencies arising from continuous average energy loss across iontherapy beams.

Σ (Avg. DSB clusters per Gy)								
mmHg O ₂	225 kVp photon	6 MV photon	0.1 MeV e	10 MeV e	1 MeV p	100 MeV p	1 MeV He ₄	100 MeV He ₄
0.001	2.99	2.85	2.85	2.83	6.60	2.88	26.29	3.46
0.1	2.90	2.92	2.94	2.91	6.78	2.96	26.33	3.56
0.5	3.34	3.27	3.28	3.26	7.44	3.32	26.42	3.96
1	3.72	3.63	3.66	3.62	8.17	3.68	26.47	4.41
2.5	4.59	4.49	4.51	4.47	9.73	4.55	26.62	5.44
5	5.51	5.40	5.42	5.37	11.30	5.46	26.73	6.52
10	6.47	6.33	6.37	6.31	12.88	6.41	26.82	7.63
20	7.26	7.11	7.14	7.09	14.10	7.20	26.87	8.56
760	9.73	8.32	8.31	8.24	15.87	8.38	26.96	9.93

3.4.2 Predicted Effects of Varied Oxygenation on STING Regulation

Hypoxic cells are less-susceptible to DNA damage and are modeled to accumulate dsDNA more gradually with dose, following common oxygen-enhancement models (Figure 11). Table 2 contains DNA damage coefficients for irradiations in varying oxygenation conditions. An anoxic dsDNA peak occurs at roughly 3x the dose of a low-LET normoxic dsDNA peak. However, high-LET radiation is capable of overcoming oxygen enhancement effects – very high-LET radiation is fully independent of cell oxygenation and is predicted to induce the same dsDNA/Trex1 response regardless of cell status (Figure 12).

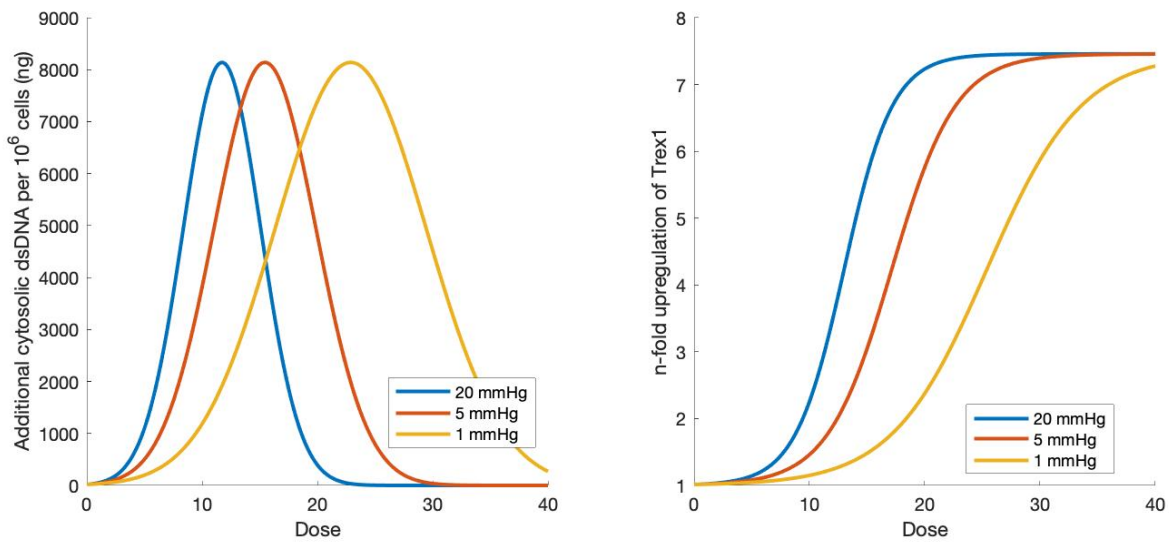


Figure 11. Predicted cytosolic dsDNA dose response following SARRP irradiation, varying oxygenation. Hypoxic cells experience fewer effective initial DSB per Gy due to the lack of oxygen fixation and enhanced chemical repair. Lower mmHg condition yield fewer DSB per Gy, resulting in accumulation of cytosolic dsDNA at higher doses (left). The ratio of doses for peak cytosolic dsDNA is the ratio of Σ between oxygen conditions, i.e. the oxygen enhancement ratio. The shallower buildup of dsDNA is followed by upregulation of Trex1 at higher doses (right).

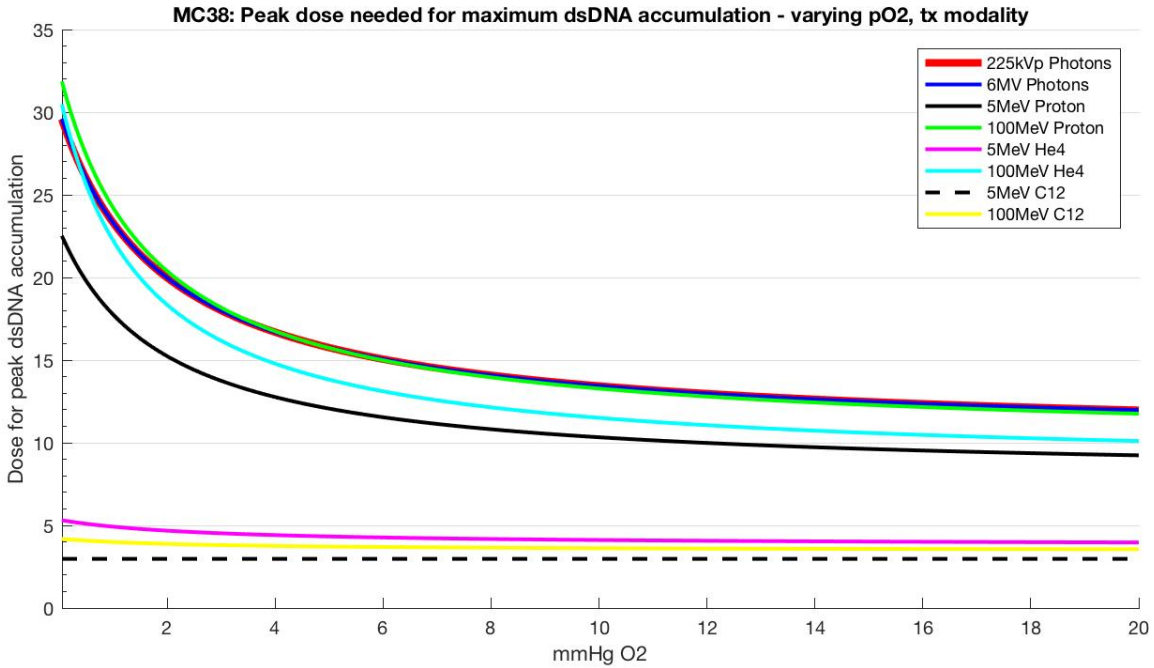


Figure 12. Predicted dose to achieve peak cytosolic dsDNA for a variety of radiation sources, as a function of cellular oxygenation. Lower-LET sources, such as photons, are expected to experience peak dsDNA accumulation at higher doses, and experience oxygen enhancement effects that can triple the dose to achieve peak response. Higher LET radiation is able to drive dsDNA accumulation at lower doses, with lesser dependence on oxygenation.

3.5 Discussion

Classical radiobiology predicts dose enhancement from elevated particle LET, and suppression following oxygen depletion⁷³. These effects hold for a variety of endpoints associated with DNA damage, such as phosphorylation of DNA repair foci, micronucleus formation, and clonogenic survival^{64,65}. Based on DNA damage modeling and a thorough analysis of published data, we also expect cytosolic DNA, thus type-I interferons, and Trex1 enhancements from high-LET radiation, such as that at the distal edge of a Bragg peak, and suppression from cellular hypoxia. These models of cytosolic DNA accumulation and Trex1 regulation can be applied to any arbitrary radiation source, using the appropriate DNA damage coefficient (Σ) from MCDS, under the assumption that equivalent initial DNA damage yields an equivalent downstream response.

The predicted effects of varied particle LET and hypoxia change both the dose for optimal immunogenicity as well as the window of doses where immunogenicity can be enhanced. This dose window narrows for very high-LET radiations, with the FWHM of the gaussian response halving for 1 MeV protons relative to SARRP x-rays. The expected dose window for hypoxic cells is also much wider.

CHAPTER 4. EXPERIMENTAL MEASUREMENT OF STING REGULATION IN VARYING CONDITIONS

4.1 Introduction

In the previous section, we attempted to model the effects of varying particle LET and hypoxia on STING regulation, under the assumption that equivalent DNA damage yields equivalent STING response, demonstrating an anticipated shift in radiation-induced immunogenicity. However, no prior data has been published demonstrating how STING immunogenicity can vary outside of low-LET x-ray irradiations, thus these measurements must be performed to validate and improve our DNA damage-based models.

In this section, we perform such measurements. The *in vitro* dose responses of dsDNA, IFN β , and Trex1 were measured in Merkel cell carcinoma cells following low-LET (orthovoltage x-ray) and high-LET (fast neutron) irradiations. Monte Carlo DNA damage modeling was used to generalize these results and form an empirical model of IFN β and Trex1 regulation as a function of physical dose and the LET-based DNA damage coefficient (Σ), as before. These models were finally applied to general particle transport simulation, to map spatial variability in IFN β , i.e. enhanced immunogenicity, across a variety of clinically relevant radiation sources.

4.2 Materials and Methods

4.2.1 Cell Culture Irradiations

Non-viral Merkel cells (MCC13)⁶³ were grown in T75 flasks with 10 mL of RPMI 1640 medium with L-glutamine, supplemented with 10% fetal bovine serum and 1% penicillin/streptomycin. Cultures were incubated at 37 degrees C and 5% CO₂ and passaged twice per week. Cultures were never allowed to reach 100% confluence. The MCC13s tested negative for mycoplasma contamination using an EZ-PCR mycoplasma detection kit.

One day prior to irradiation, cells were passaged and plated in 6cm plates or 4-well chamber slides, depending on the endpoint desired. All plates were seeded for a maximum of 80% confluence at 4-days post-irradiation, roughly 600,000 cells per 6 cm plate or 60,000 cells per well

in a chamber slide. Growth medium was added to 2 mm depth for consistent dosimetry across plates, 4mL for 6cm plates or 0.4 mL for chamber slides. Cells were allowed to incubate at least overnight.

For SARRP irradiation, the x-ray tube was allowed to perform a ~20-minute warmup routine, where the tube cycles through all available voltage/current settings. Upon completion, cell plates were loaded onto the treatment stage at the maximum SSD allowable, the collimator was removed to allow an open field, and plates were irradiated at 220 kVp, 13 mAs, at a dose rate of 2.51 Gy/min (Figure 13). The dose rate was verified by film dosimetry. Irradiations were delivered such that cell plates were out of the incubator for less than 20 minutes, to minimize environmental effects from varying temperature, CO₂ concentration. After irradiation, the growth medium was replaced in all plates, and the cells were immediately returned to the CO₂ incubator. Dose escalation irradiations were delivered up to 22 Gy.

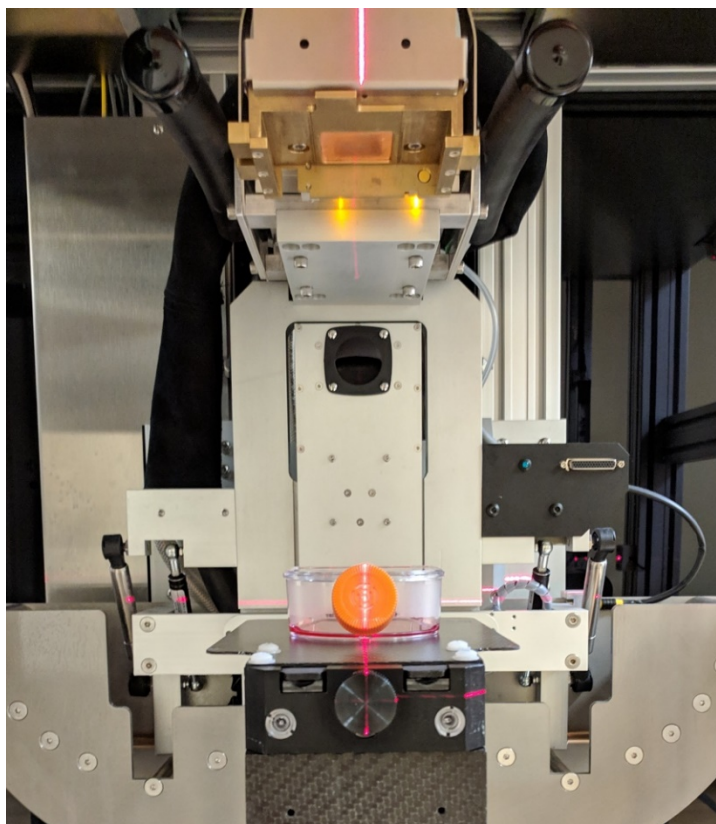


Figure 13. Cell culture flask set up for irradiation on an Xstrahl SARRP. The SARRP uses a copper filter, with the collimator removed to expand the field as much as possible. The stage is also lowered to enable the highest amount of beam divergence possible. The flask, here a T75, is aligned to the treatment field with lasers.

For fast neutron irradiation, exposures were performed immediately following patient treatment, thus no warmup was needed. Irradiations were delivered using the geometry calibrated by the Clinical Neutron Therapy System (CNTS) engineers (Figure 14). Briefly, the neutron gantry was set to 180 degrees and cells were loaded onto the treatment couch with 2cm of solid water buildup. The dose rate was determined to be 60 cGy/MU. Due to the inefficiency of neutron production through p/n reactions, the neutron doses were limited to ≤ 8 Gy to minimize damage to the beam target. Irradiation timing and post-irradiation medium changes were performed using the same protocol as SARRP irradiations.

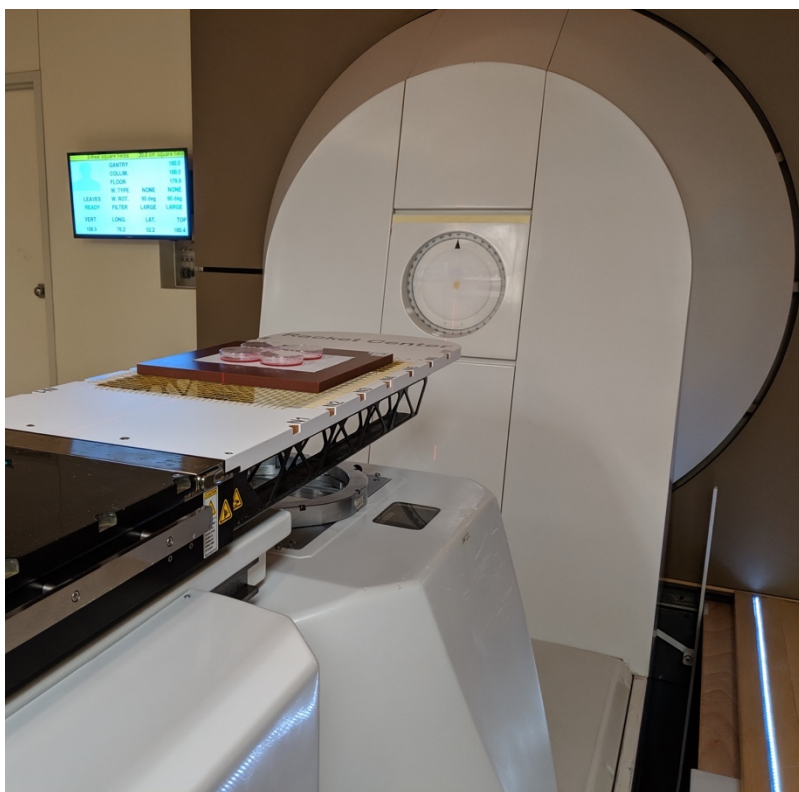


Figure 14. Cell culture plates set up for irradiation using the Clinical Neutron Therapy System at the University of Washington. Cells are irradiated from the bottom-up with 2cm of solid water, to ensure that the cells are beyond the buildup region of the neutron PDD. Due to the low dose rate and limited efficiency of neutron production, 4 samples were irradiated at once with staggered doses to minimize the total delivered dose and lessen damage to the CNTS beryllium target.

After irradiation, the MCC13s were allowed 4 days to incubate. This time point was determined by the Nghiem lab, but verified by IFN β assay using SARRP-irradiated cells at 8 Gy. The doubling time for MCC13 was measured to be roughly 38 hours, so a 4-day incubation ensures

that the treated cells are able to undergo two mitotic cycles. This is important because it allows time for formation and collapse of micronuclei in damaged cells, cGAS detection of cytosolic dsDNA, and full onset of cytokine production.

Per each following endpoint, at least three datasets were acquired for both SARRP and fast neutron irradiations, and statistical significance was calculated using a paired student's t-test. Complete assay protocols are included as Appendices A-C.

4.2.2 Interferon Beta Assay

Interferon Beta was measured in the supernatant (used growth medium) of irradiated cells using an enzyme-linked immunosorbent assay (ELISA). The supernatant from 6cm plates was harvested with a serological pipette and transferred to 15 mL tubes. The supernatant was centrifuged at 1000 rpm for 5 minutes to pellet cell debris and dead cells, and aliquoted into multiple 1.5 mL tubes for later assay. Samples were stored at -20 or -80°C as freezer space was available. Cells were counted for proper normalization of the assay.

IFN β quantification was performed using a DuoSet Human IFN β ELISA kit with ancillary supplies (R&D Systems, DY814-05). This kit uses a sandwich ELISA technique, where a 96-well plate is coated with a capture antibody optimized to 'catch' IFN β in a 100-microliter sample. A secondary detection antibody is applied, immediately followed by a streptavidin conjugated to horseradish peroxidase (HRP). When a substrate solution of hydrogen peroxide and tetramethylbenzidine is applied, the HRP undergoes a colorimetric reaction, darkening wells that have successfully 'sandwiched' a cytokine. After a sufficient time, a 'stop' solution of sulfuric acid is applied to stabilize the color development. Readout is performed using absorbance measurements (optical density, OD) on a Synergy4 microplate plate reader, at wavelengths of 450 and 540 nm. Peak absorption occurs at 450 nm, with the latter wavelength used as a background correction in the event of plate defects. A calibration curve is measured using IFN β standards supplied in the DuoSet kit, serially diluted in complete RPMI.

To analyze the ELISA plate, the OD reading at 540 nm is subtracted from the reading at 450 nm to account for plate defects, and data from replicate wells are averaged. The OD

measurements from the 0 pg/mL standard are subtracted from all values, to fully account for net changes in OD. The calibration curve is generated by fitting the measured IFN β standards to a second-order polynomial, experimentally determined to result in the highest goodness-of-fit. This calibration curve is applied to all of the test wells on the plate to determine the absolute quantity of IFN β per well, in pg/mL. The IFN β readings are lastly normalized to the number of cells in the original plate, and the total volume of supernatant harvested from the plate.

4.2.3 Cytosolic dsDNA Assay

Cytosolic dsDNA assay was performed using the same cells as the IFN β assay. After harvesting the supernatant and counting the cells in each irradiated plate, cells suspensions were centrifuged and medium was replaced with phosphate-buffered saline such that the cell concentrations were 1 million cells per milliliter. 500,000 cells per sample were loaded into 2 mL centrifuge tubes with an angled base and passed through a NE-PER nuclear and cytosolic extraction kit (Thermo Scientific, 78833). Briefly, cells are centrifuged again, and PBS is replaced with CER-I reagent supplemented with HALT protease inhibitor (Thermo Scientific, 78430). Tubes are vortexed vigorously to resuspend the cell pellet and placed on ice for 10 minutes. During this time, the combination of CER-I and cold temperature gently perforates the cell membrane. After 10 minutes, CER-II reagent is added to the suspension, vortexed to mix, and returned to ice for 1 minute. CER-II neutralizes CER-I and halts the reaction. Then, tubes are centrifuged at 14,000 RPM for 5-6 minutes to fully separate nuclear and cytoplasmic fractions. Cytosolic extracts in the supernatant are aliquoted to pre-chilled 1.5 mL tubes and stored at -20°C for later assay.

Double-stranded DNA quantification was performed using a Spectramax dsDNA Nano Quant bulk kit (Molecular Devices, #R8357). Cytosolic extracts are diluted with sterile PBS to ensure readings fall within the dynamic range of the kit, around 2000 cell extracts per μ L, and plated in a black-bottom 96-well plate with calf thymus DNA standards supplied in the kit. A working solution of de-ionized water, supplied buffer, and supplied DNA dye is mixed and applied to each well, and allowed 5 minutes to incubate in the dark. Fluorescence readings are then immediately measured on a Synergy4 plate reader, with excite/emission wavelengths set to 468/507 nm and saved in an Excel spreadsheet in relative fluorescence units (RFU).

To convert RFU into dsDNA measurement, a calibration curve is generated using the DNA standards. Like with IFN β , the calibration curve is generated by fitting the standards to a second-order polynomial, again experimentally determined to result in the highest goodness-of-fit. This calibration curve is applied to all of the test wells on the plate to determine the absolute quantity of dsDNA per well, in nanograms. The cytosolic extracts are already normalized to ~20,000 cells per well, but measurements are rescaled to determine the nanograms of dsDNA per million cells, for direct comparison to literature.

4.2.4 Exonuclease Trex1 Assay

After incubation, 4-well chamber slides are washed twice in sterile PBS and fixed using 10% paraformaldehyde for 10 minutes. Cells are permeabilized using a 0.5% Tween-20 solution in PBS, with a 10-minute incubation. Non-specific antibody blocking was performed with 3% bovine serum albumin for 30-60 minutes. Immunofluorescence staining is performed by incubating cells with a pre-conjugated Trex1/Alexa594 antibody (Abcam ab217095) at a 1:500 dilution in PBS for 2 hours. Additional dsDNA staining is performed using a primary dsDNA antibody, incubating for 2 hours, and a secondary Alexa488 Fluor, also incubating for two hours (Abcam ab27156, ab150113). Slides are washed at least twice between each step, and all incubation steps were performed rocking slowly at room temperature. Upon completion, a coverslip is mounted using a drop of ProLong mounting medium, containing DAPI, as a nuclear DNA counterstain (Invitrogen, P36935). MCC13 experiments were compared to prior data measured in MC38 colorectal adenocarcinoma cells, from the Youngblood lab at the Department of Immunology at St. Jude Children's Research Hospital.

Slides are imaged using a Nikon 90i fluorescence microscope at 20x magnification, and at least 5 views are captured for each sample on each slide. Images are analyzed in ImageJ using customized macro scripts for efficiency. A rough cell count for each view is determined by converting a DAPI image into a binary and applying the watershed function to divide nuclei that are touching. An 'analyze particles' routine is called to count the discrete number of particles above a defined size, and the total count is saved in a .csv file. The total integral density of Trex1 fluorescence is sampled by using the 'measure' function, and the results are saved to a separate .csv file.

A MATLAB script was written to compile and summarize the microscopy data. All DAPI and Trex1 data files are identified, loaded, and data is sorted by both delivered dose and radiation modality. The average and standard deviation of the cell count and Trex1 integral density is determined for each data point over all replicate samples. To find the integral density per cell, the Trex1 integral density is normalized by the cell count per image, which is also averaged per sample. Lastly, the Trex1 data was normalized to the background expression of Trex1 in un-irradiated cells, to determine the relative upregulation per cell.

4.2.5 Interferon Beta and Trex1 Modeling

To develop an empirical model of in vitro STING regulation and suppression, IFN β and Trex1 dose response curves from x-ray and neutron irradiations were fitted to a single-term gaussian (Eqn. 4.1) and a first-order polynomial function (Eqn. 4.2), respectively, using the MATLAB curve fitting toolbox. Curves were fitted as functions of both physical dose and a source-dependent biological effect factor, Σ (DSB clusters/Gy/Gbp), an output factor from Monte Carlo Damage Simulation (MCDS) modeling software⁷⁴. MCDS operates using track structure modeling to determine the number of ionization interactions from charged particles capable of causing DNA damage, while mapping the spatial distribution, or clustering, of the damaged DNA within the nucleus⁷⁵.

$$IFN\beta(D, \Sigma) = a * \exp \left[- \left(\frac{D * \Sigma - b}{c} \right)^2 \right] \left(\frac{pg}{mL} \text{ per } 10^5 \text{ cells} \right) \quad (4.1)$$

$$Trex1(D, \Sigma) = a * D * \Sigma + b \text{ (} n - \text{fold upregulation)} \quad (4.2)$$

Σ for SARRP x-rays was determined by inputting the secondary electron fluence spectrum for 220 kVp x-rays into MCDS, which was modeled using FLUKA general purpose Monte Carlo software. A 220 kVp photon source was modeled to manufacturer specifications for an Xstrahl SARRP using a Varian NDI 225/22 x-ray tube, with 0.8 mm beryllium and 0.15 mm copper filtration, as described in Chapter 3. Σ for fast neutrons (22.41) was obtained from previously published data²⁶.

These models were extended to include Σ for alternative radiation sources, including 6MV linac and charged particle beams (electron, proton, alpha, and carbon ions). The 6MV linac source was modeled in FLUKA using a phase space file from the CERR external beam dose calculation package, initially modeled in VMC++, as previously described⁷¹. Mono-energetic proton, electron, helium-4, and carbon-12 particle sources were directly modeled in MCDS, with particle energies varied between 1 keV and 300 MeV⁷⁵. All MCDS simulations were performed using 50,000 trials to achieve a standard error of less than 1%, using default settings for nucleus diameter (5 μm) and DNA content (1 Gbp).

4.2.6 Modeling IFN β in General Purpose Monte Carlo

Custom FLUKA user subroutines were written to score dose and Σ across an entire radiation field using an empirical approach adapted from Stewart et al²⁶. Briefly, the squared ratio of effective charge and particle speed relative to the speed of light are applied to equation 3 to determine the RBE with respect to DSB, defined relative to cobalt-60 ($RBE_{DSB} = \frac{\Sigma_{test}}{\Sigma_{Co60}}$). Spatial maps of Σ are found by multiplying RBE_{DSB} by the reference Σ (8.3 DSBc/Gy/Gbp). Particle transport Monte Carlo simulations were performed, with the initial beam spot size defined as 5 mm full-width at half-max, for 6MV x-rays, CNTS fast neutrons, and mono-energetic proton, He4, and C12 beams with a range of 10 cm in water in FLUKA, with a voxel resolution of 2 mm. Simulations used 10^8 initial histories. Depth-amplitude plots of the physical dose and Σ are applied to Eqns. 1 and 2 to model and compare the variability in IFN β and Trex1 regulation across whole radiation fields.

$$\Sigma \left(\frac{\text{DSBc}}{\text{Gy} \cdot \text{Gbp}} \right) = RBE_{DSB} * \Sigma_{Co60} = \left[a + b - \left\{ b^{(1-d)} + cx(d-1) \right\}^{1/1-d} \right] * 8.3; \quad x \equiv \left(\frac{z_{eff}}{\beta} \right)^2 \quad (4.3)$$

$$a = 0.9902, \quad b = 2.411, \quad c = 7.32 * 10^{-4}, \quad d = 1.539$$

4.3 Results

4.3.1 Interferon Beta Dose Response

Supernatant from SARRP-irradiated cells was not positive for IFN β until 4 days post-irradiation. This agrees with prior data and supports the theory that time is required between irradiation and immunogenicity due to the time required for micronuclei to form and collapse. At 24 hours post-irradiation, some micronuclei have formed but are largely intact.

The dose response for SARRP-irradiated loosely follows cytosolic dsDNA trends in data published by Vanpouille-Box³⁵. IFN β gradually builds until a peak at 14.5 Gy, with a falloff at higher doses (Figure 15). The IFN β dose response for neutron-irradiated cells follows a similar trend, but peaks and falls off at lower doses, between 6.1 Gy. The peak doses were determined from Gaussian fits to the data. The ratio of peak doses is 2.4, which closely agrees with the measured RBE for micronucleus induction, as well as the modeled RBE with respect to DSB calculated in MCDS, for CNTS fast neutrons relative to SARRP x-rays (2.3). Interestingly, the amplitude of the neutron IFN β measurements were not significantly different from the SARRP IFN β measurements. This suggests that radiation induced IFN β secretion scales with the number of initial DSB per cell, rather than the local DSB complexity or the ability of a cell to repair individual DSB.

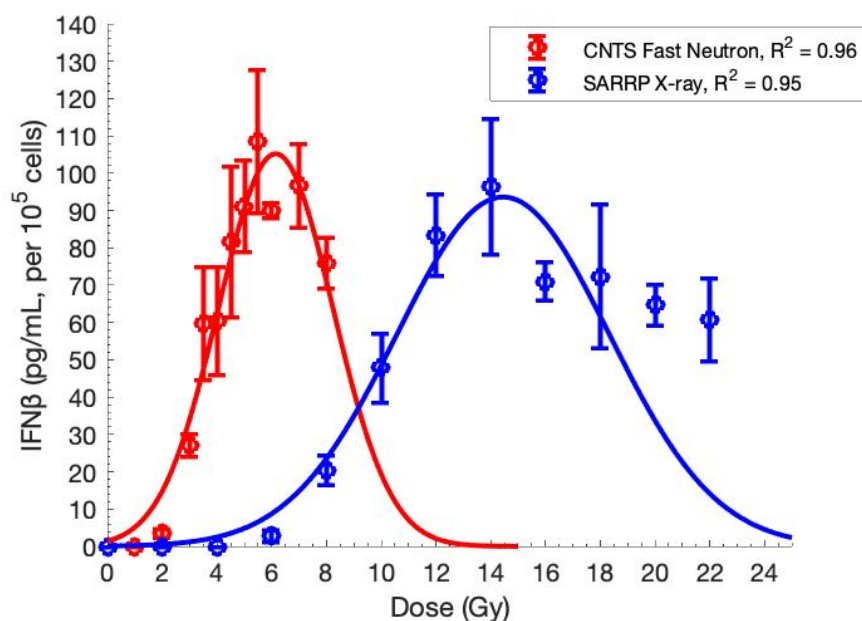


Figure 15. Secreted IFN β dose response in MCC13 cells following SARRP x-ray irradiation and CNTS fast neutron irradiation by ELISA. The ratio of these peak doses is 2.4, approximately equivalent to the RBE_{DSB} reported for CNTS neutrons. There is no significant difference in the amplitude of peak IFN β secretion ($P > 0.05$; paired t-test).

The peak doses and peak amplitudes follow a trend that appears to be age/passage related (Figure 16). Peak IFN β occurs at higher doses for cells at higher passage numbers. The amplitude of peak IFN β also diminishes with passage. These age-related effects rapidly change at low passage numbers and appear to stabilize at high passage numbers.

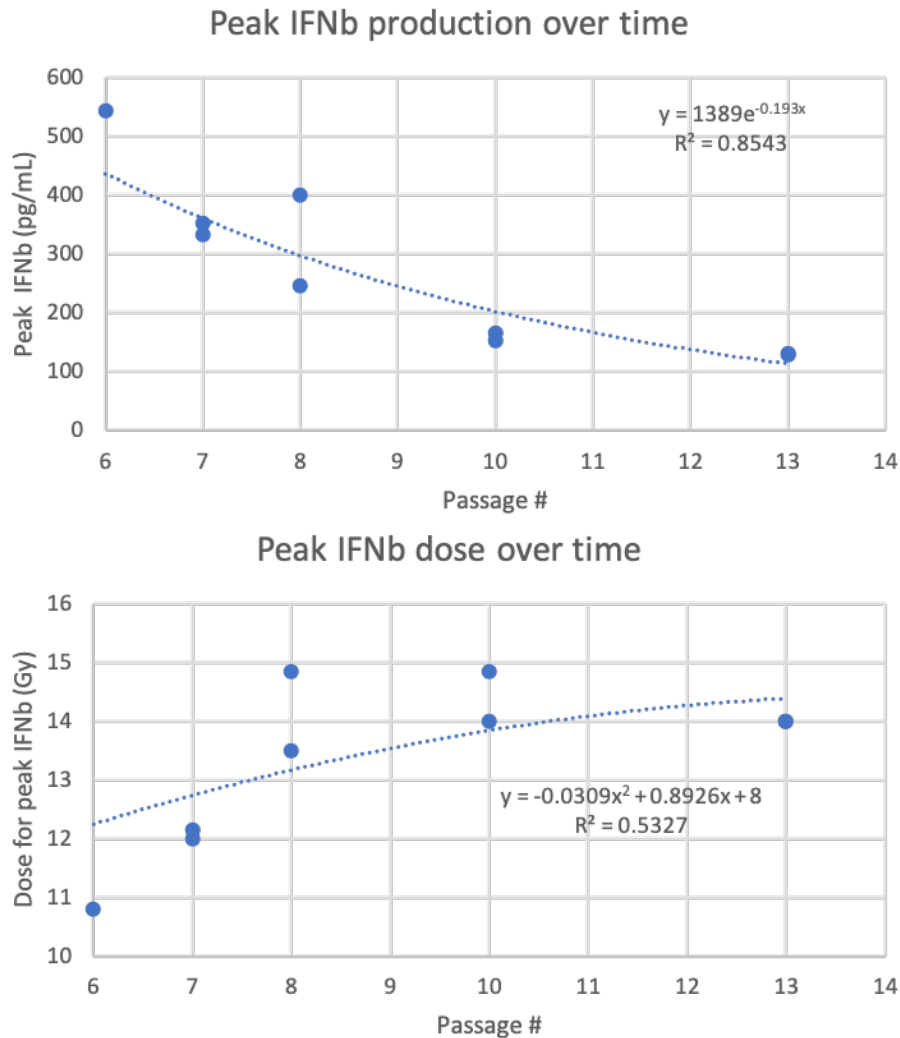


Figure 16. The effects of passage number on peak interferon beta production, and the RBE-weighted dose to achieve peak IFN β . (Top) The peak amplitude of IFN β steeply decreases with passage. (Bottom) The dose required to induce peak IFN β secretion steadily increases with passage. These trends support published data indicating that cells maintained in culture will gradually see inhibit their innate immune response due to lack of stromal and immune components *in vitro* (Mouriaux et al., 2016).

4.3.2 Cytosolic dsDNA Dose Response

Cytosolic DNA measurements were inconclusive and discussed with Claire Vanpouille-Box prior to her protocol submission⁷⁶. Briefly, measured cytosolic DNA produced a flat dose response, without a pronounced dsDNA peak (Figure 17). These measurements closely agreed

with high/low-dose background shown by Vanpouille-Box. Cell confluence was deemed to be the main issue, with under-confluent or over-confluent cells unable to properly accumulate cytosolic dsDNA. However, further issues arose in the cytosolic extraction step of the assay, particularly from inconsistencies in cell counts following washing steps. This endpoint was omitted from further study in favor of IFN β and Trex1.

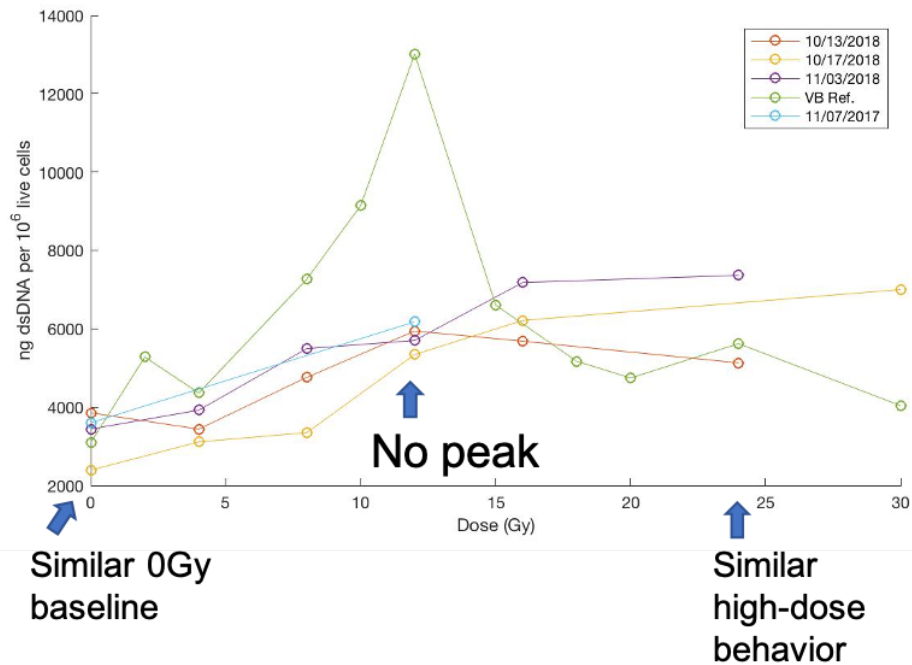


Figure 17. Cytosolic dsDNA dose response in MC38 cells following SARRP x-ray irradiation. The peak at 12 was not reproduced from Vanpouille-Box (2017, shown in green), while the background dsDNA was comparable. Due to the success of the IFN β and Trex1 assays, this was assumed to be a procedural issue.

4.3.3 Exonuclease Trex1 Dose Response

Following prior literature, Trex1 upregulation increases at high doses. However, the shape of the measured dose response curve is roughly linear, possibly from sparse dose sampling. Neutron-irradiated cells accumulate interferon-stimulatory DNA more rapidly per dose than SARRP-irradiated cells, thus Trex1 also upregulates more readily with dose. The relative difference in the slope of the dose response curves is roughly 4.0. The relative amplitudes of Trex1 upregulation were not significantly different between RBE-equivalent doses.

Secondary measurements of dsDNA by immunofluorescence were also inconclusive. Assays suffered from long permeabilization times, leading to antibody binding in the nucleus. This created an excessive background signal that obscured the productive dsDNA dose response.

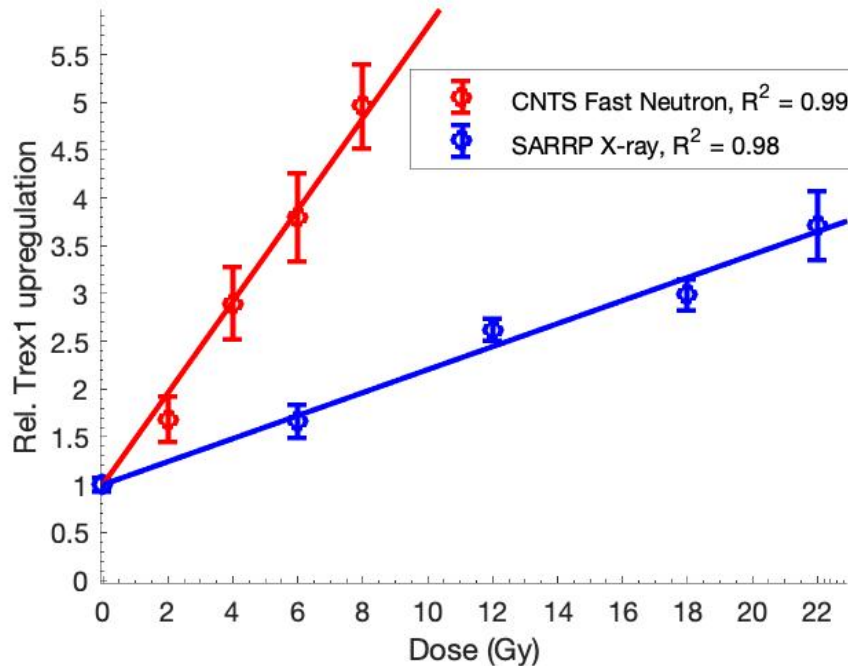


Figure 18. Measured TREX1 dose response in MCC13 cells following SARRP x-ray irradiation and CNTS fast neutron irradiation. Dose responses are normalized to background expression of TREX1. The ratio of slopes, i.e. the RBE_{TREX1} , is 4.0.

Prior measurement of Trex1 in MC38 cells demonstrated a passage-dependent dose response, that appears more sigmoidal at lower passages. Note that these cells were unable to produce $IFN\beta$ and cytosolic dsDNA following ionizing radiation.

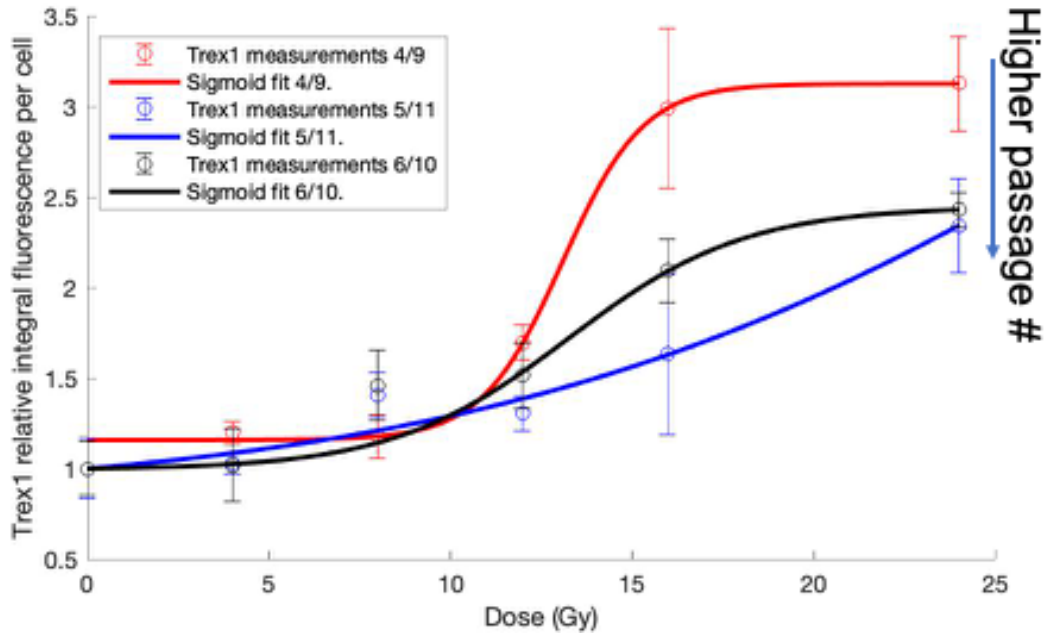


Figure 19. Trex1 dose response in MC38 cells following ionizing radiation. As the passage number increases, the dose response appears less sigmoidal.

4.3.4 Interferon Beta and Trex1 Modeling

Fit coefficients for IFN β and Trex1 dose responses can be seen in Table 3, and Σ Monte Carlo damage coefficients for a variety of low and high-LET radiation sources in Table 2. The R^2 for all fits was > 0.9 . Higher-LET radiation induces more DSB per dose than low-LET radiation, thus IFN β was modeled to accumulate at lower doses (Figure 20). Similarly, exonuclease Trex1 is upregulated at lower doses in high-LET radiation. Here, the ratio of peak doses between a test and reference radiation source is used to define the RBE with respect to IFN β secretion, $RBE_{IFN\beta}$, which is roughly equivalent to the RBE_{DSB} obtained from MCDS (Eqn. 3.1). In Table 3, the reference radiation source for $RBE_{IFN\beta}$ is Cobalt-60.

$$RBE_{IFN\beta} = \frac{D_{peak\ IFN\beta, test}}{D_{peak\ IFN\beta, ref}} \cong RBE_{DSB} \quad (4.4)$$

Table 3. Fit coefficients for IFN β and Trex1 dose response following SARRP x-ray or CNTS fast neutron irradiation. IFN β measurements were fitted to a single-term Gaussian function, and Trex1 was fitted to a sigmoid function using the MATLAB curve fitting toolbox (Eqn. 1 and 2).

	220 kVp x-ray		CNTS Fast Neutron	
	IFN β	Trex1	IFN β	Trex1
a	147.4	0.1001	161.9	0.1755
b	17.3	1	16.7	1
c	7.1	--	8.3	--
RBE_{DSB}	1.19		2.70	
R²	0.95	0.98	0.96	0.99

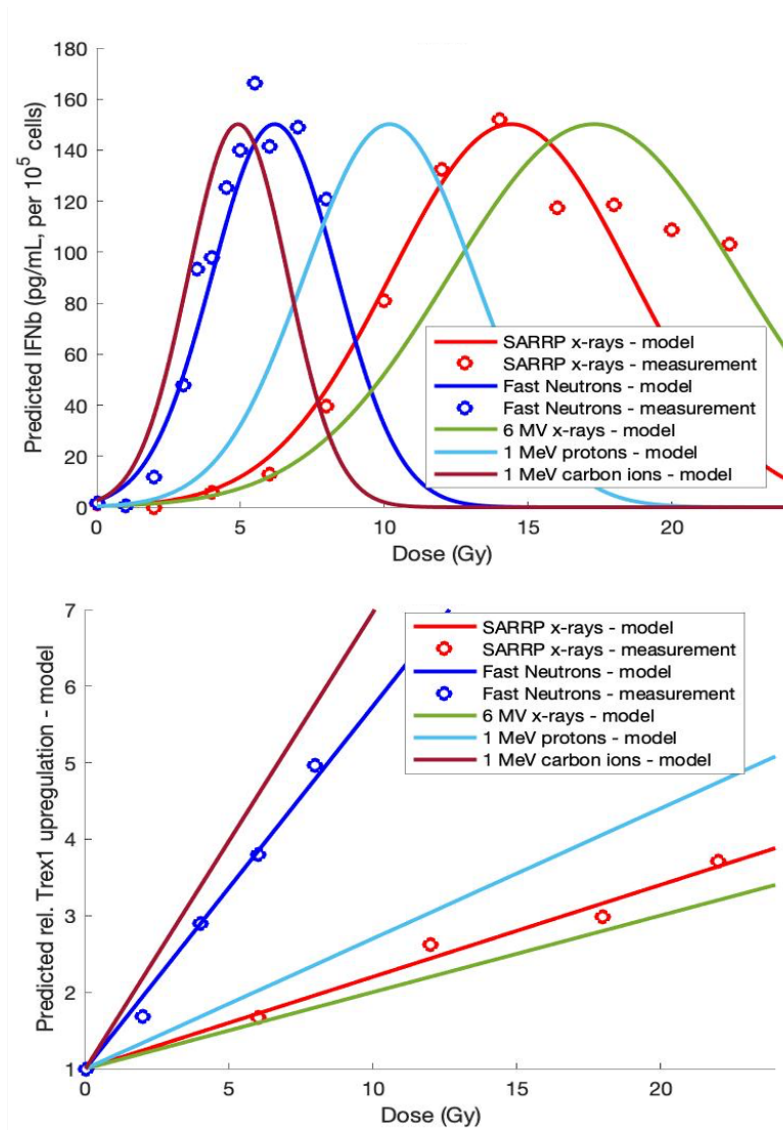


Figure 20. Modeled IFN β and Trex1 regulation as a function of dose, for SARRP x-rays, fast neutrons, 6 MV x-rays, low-energy protons, and low-energy carbon ions. (Top) IFN β secretion as a function of dose for various radiation sources. High-LET radiation induces more DSB Gy⁻¹ and have a larger RBE_{DSB}, which parallels the increased efficiency of IFN β secretion. (Bottom) Trex1 upregulation as a function of dose for various radiation sources. Accumulation of DNA damage at lower doses enables Trex1 upregulation at lower doses. All fits to measured data use inputs for MCC13 cells (Table 1, 2).

4.3.5 Modeling IFN β in Particle Transport Monte Carlo

Σ and physical dose values from FLUKA can be applied to quantify spatial distributions of potential IFN β secretion enhancement, shown as depth dose curves scaled to their RBE_{IFN β} -

equivalent doses and corresponding depth-IFN β curves (Figure 21). Uncharged radiation sources, such as low-LET 6MV x-rays and fast neutrons, don't undergo dramatic changes in Σ as they propagate through tissue. For these sources, activating STING is simply a matter of optimizing the RBE_{IFN β} -weighted dose to a target, which can be achieved through a variety of conventional radiotherapy techniques. For iontherapy sources, the variability in LET and mean energy with depth drives an increase in Σ near the distal edge of their Bragg peaks, resulting in a localized region of potential IFN β stimulation. Heavier ions have a sharper Bragg peak with respect to depth, thus the doses for optimal pro-immunogenic response become tighter, both biologically and dosimetrically.

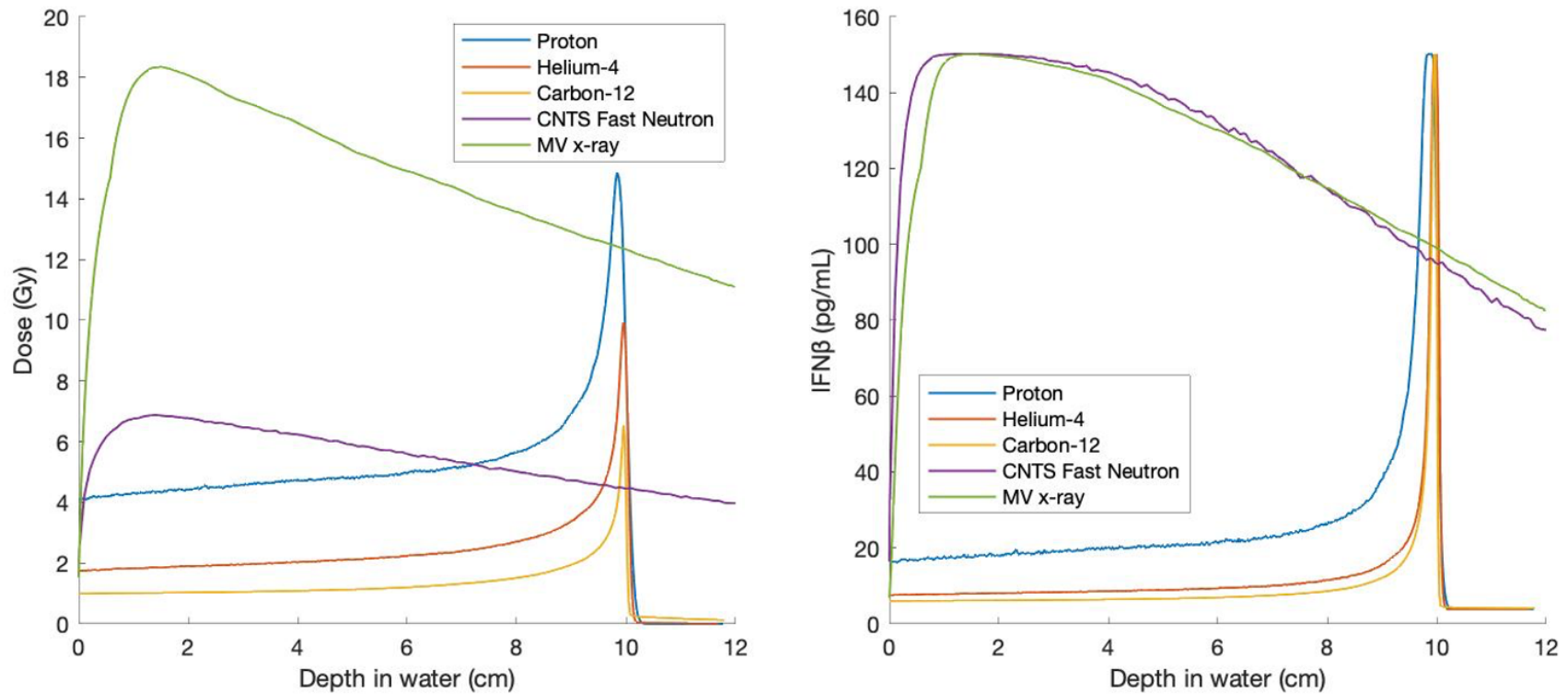


Figure 21. Monte Carlo model of IFN β dose-response for 6 MV x-rays, CNTS fast neutrons, protons, alpha particles, and carbon ions. (Left panel) Depth-dose plots for a variety of clinical beams, normalized to produce peak IFN β in MCC13s treated at the depth of max dose. (Right) IFN β secretion as a function of depth in water for varying clinical beams. Delivered doses for ion sources can be normalized such that IFN β is only stimulated around their Bragg peak; heavier ions can produce sharper regions of pro-immunogenic activity than indirectly ionizing x-rays or neutrons. Uncharged sources can stimulate elevated IFN β more uniformly with depth.

4.4 Discussion

While immunotherapy provides an exciting new treatment option, most solid tumors are seldom responsive to immunotherapy alone¹⁷. An increasingly advocated approach to enhance the efficacy of immunotherapy is to provide concurrent radiation to stimulate STING signaling and immunogenic cell death, which may be optimal within a narrow dose window^{77,78}. Limited prior data has explored the effects of radiation quality on radiation-enhanced immunogenicity. Here, we have demonstrated differential STING response in MCC13 cells by measuring the dose-response characteristics of IFN β and TREX1 following irradiation by low-LET x-rays and high-LET fast neutrons. Stewart et al.²⁶ report that CNTS fast neutrons have an RBE for DSB induction (RBE_{DSB}) of 2.3 relative to SARRP x-rays, which is equivalent to the RBE_{DSB} of 140 MeV $^{12}\text{C}^{6+}$ ions (LET=142.4 keV/ μm and a 0.57 mm range in water)⁷⁵. The measured value for $RBE_{\text{IFN}\beta}$ (2.4) is remarkably close to the RBE_{DSB} of for CNTS neutrons relative to SARRP x-rays. This suggests that radiation-induced IFN β secretion scales with the number of initial DSB per cell, rather than a metric of local DSB complexity or the ability of a cell to repair individual DSB. However, the RBE_{TREX1} was notably higher than $RBE_{\text{IFN}\beta}$, indicating that TREX1 immunosuppression is more readily activated by higher-LET radiation. The mechanism of TREX1 upregulation in response to genotoxic stress is still poorly understood, and further study is needed to explain this differential response. The neutron $RBE_{\text{IFN}\beta}$ and RBE_{TREX1} reported here are higher than the published RBE for micronucleus induction of 2.0 ± 0.1 , but smaller than the RBE for nucleoplasmic bridges of 5.8 ± 2.9 ⁶⁵.

The results from this study are consistent with several clinical case studies of Merkel cell carcinoma patients treated with fast neutrons and add additional insight into potential improvements. Parvathaneni et al treated patients refractory to standard radiation therapy with up to 3 Gy doses of fast neutrons, with some patients seeing complete remission and sustained control for up to 5 years^{22,23}. The results from this study help explain the refractory response to x-ray radiation therapy and a potential immunogenic response from neutrons. Peak IFN β production occurs at 14.5 Gy for low-LET x-rays (Figure 15) with little to no response at conventional (1.6-2 Gy) and most hypofractionated doses (6-8 Gy). With an $RBE_{\text{IFN}\beta}$ of 2.7 (relative to Co-60), the dose to achieve peak IFN β production for fast neutrons decreases to 5.5 Gy. At 3 Gy, IFN β is only 30% of its peak value and at background levels below 1 Gy. Therefore, a single dose of 6 Gy may

be more effective at potentiating an out-of-field response in combination with immune checkpoint inhibitors, with higher doses expected to provide little additional benefit and increase the potential for normal tissue complications. This is supported by prior carbon ion studies⁷⁹, demonstrating abscopal effects at 5.3 Gy in murine models of osteosarcoma. Based on prior literature, repeat fractions would be expected to further enhance IFN β secretion, but the effects of fractionation were not explored here. The reduction in immune signaling with passage agrees with literature, where melanoma cells cultured for long passage times see inhibited immune signaling genes due to the lack of *in vivo* stromal and immune components, *in vitro*⁸⁰.

Fast neutrons chiefly deposit dose through secondary low-energy protons and alpha particles, which offer high RBE and immunogenic enhancement²⁵. One advantage of fast neutrons over iontherapy is the uniformity of RBE and LET with depth, as well as the lack of end-of-range uncertainties. Less variability across a beam allows more simple treatment planning and optimization purely based on physical dose, without the risks of end-of-range, high dose-LET effects in nearby organs at risk. A disadvantage would be the potential for anti-immunogenic response from non-targeted tissue or cells which can obfuscate the innate and adaptive response mechanisms. For iontherapy sources, narrow spatial regions of high-LET radiation, such as at the end of a Bragg peak, may be used advantageously to more-precisely sculpt regions where pro-immunogenic effects are desired. Spread-out Bragg peaks will be necessary to induce IFN β in a volumetric target. Tables 2-3 provide a general framework for calculating RBE_{IFN β} for 6 MV x-rays and fast neutrons, as well as for common ions superficially and at their end of range. Our models enable prediction and simulation of such effects across entire radiation fields, which can be used to design simple treatment plans in general-purpose Monte Carlo software. The results in Figure 20 demonstrate how such a treatment can be constructed. The RBE_{IFN β} factor can be used to define the dose that will stimulate peak IFN β at depth for a specific radiation field (MV, proton, alpha, carbon ion). Due to the nonlinear response (Figure 19), the off-target dose and IFN β production can be kept proportionally (significantly) lower. This would quickly be lost if the target volume increased, and in these situations, a multi-field treatment would be designed.

One limitation of this study is breadth: only one cell line (MCC13) was used for laboratory experiments. This is largely due to the rarity of cultured cell lines having intact STING signaling.

MC38 murine colorectal cells from two sources and A549 human lung adenocarcinoma cells were also examined for STING but failed to produce IFN β in response to radiation or DNA transfection. Literature indicates that deficiencies in cGAS, a cytosolic double-stranded DNA sensor, are common in colon adenocarcinoma cell lines, which frequently occur following hypermethylation of promoter regions, and can in part be restored using demethylation agents⁸¹. However, exploring the restoration of STING in these cells was beyond the scope of this work.

The effects of tumor hypoxia on radiation-induced STING signaling will be a topic of further study. Tumor hypoxia is classically known to inhibit radiation-induced DNA damage by muting oxygen fixation from indirect action by low-LET radiation⁶⁶. Only considering initial DNA damage modeling in MCDS, anoxia results in an LET/RBE-dependent decrease in Σ , thus higher doses are required for equivalent STING activity. However, limited prior studies show suppressed cGAS in hypoxic conditions, resulting in limited downstream IFN β production⁸². It is unclear if high-LET radiation might partially compensate for these effects.

Based on DNA damage modeling, we predicted that the dose responses of STING regulators followed RBE_{DSB} trends – that equivalent DNA damage yielded equivalent downstream effects. Through IFN β and Trex1 measurement of SARRP and neutron irradiated MCC13 cells, this prediction was confirmed. Thus, if the radio-immunogenic response of a cell is known, the response can be further predicted if the RBE_{DSB} is known for the radiation type.

Although IFN β and Trex1 measurements were successful, cytosolic DNA measurements failed, likely as an issue during the procedure. A recent protocol publication by Vanpouille-Box⁷⁶ offers explanations for both microplate and immunofluorescence techniques. Accurate counts are critical, yet cell loss was too significant during the first step of cytosolic extraction, with variations between 20-40% measured between start/finish counts. Immunofluorescence based assay failed due to over-permeabilization, as described above.

CHAPTER 5. DEVELOPMENT OF IMAGING TECHNIQUES TO LOCALIZE AND DISTINGUISH HYPOXIC STATUS

5.1 Introduction

As stated in section 1, tumor hypoxia can manifest from perfusion (acute) and diffusion (chronic) limitations in oxygen delivery, which drive a variety of negative prognostic factors including metastasis, treatment resistance, and recurrence⁴⁸. As demonstrated in Chapter 3, hypoxic cells are expected to be less immunogenic through STING, with peak responses predicted at upwards of 20 Gy in a single delivery. Most spontaneous tumors are at least partially hypoxic⁸³, and clinical radiation fractions rarely⁸⁴ exceed 8 Gy – thus we anticipate the hypoxic niche within a tumor to not be contributing to the overall immune response in most cases. This wide differential in the required doses for STING activation will necessitate radiotherapy planning that both considers and adapts to a patient’s current hypoxic status. Further, the characteristics of cancer cells, with respect to both radiosensitivity and immunosuppression, can wildly vary based on the temporal stability of hypoxia. Therefore, imaging techniques that are sufficiently able to detect and classify hypoxic status are needed.

This section describes a newly developed approach for tumor hypoxia imaging via photoacoustic techniques, which offer high spatial and temporal resolutions at a cost of limited field of view. In this section, we will use photoacoustic imaging to develop a procedure for detecting and classifying hypoxic status in-vivo.

5.2 Materials and Methods

5.2.1 Photoacoustic CT

PCT-S images were acquired using the prototype Nexus128 photoacoustic CT system (Figure 22). This scanner uses an optical parametric oscillator (OPO)-tunable yttrium-aluminum garnet (YAG) laser to stimulate biological samples suspended at the isocenter of an array of 128 ultrasound transducers. Transducers are 3mm diameter with a 5 MHz center frequency, arranged in a rotating hemispherical surface (‘bowl’). The transducer bowl is filled with water, and the temperature is increased to 37 degrees Celsius. The sample is loaded into a thin plastic tray with a

small indent designed for murine tumors, with a few mL of water to fully couple the sample to the system. Images are sampled at 10 wavelengths: 700, 720, 735, 755, 775, 798, 830, 860, 890, 920 nm. Image reconstruction was immediately performed using filtered backprojection through the software packaged with the Nexus acquisition.

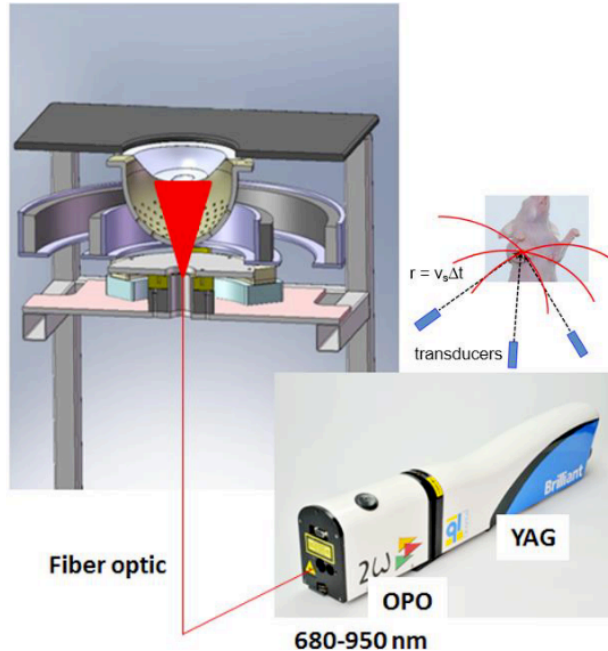


Figure 22. Schematic of the Nexus128 photoacoustic CT scanner. An OPO-tunable YAG laser is directed through a fiber optic cable into the bowl of the PCT scanner. A tumor sample held in the upper ‘bowl’ of the scanner is excited by exposure to the laser, creating ultrasound signals that propagate outward at a nearly-constant velocity. Sampling the timing of these ultrasound signals enables the origin of the absorption to be calculated. Figure from Justin Sick thesis (2016)

5.2.2 Murine Tumor Models

5.2.2.1 Syngeneic MC38

Immunocompetent female albino B6 mice were seeded with 1×10^6 murine colorectal adenocarcinoma cells (MC38) on their rear flanks by Ardiana Moustaki from the Youngblood Lab at St. Jude Children’s Research Hospital, Department of Immunology. MC38-seeded mice were delivered to the Stantz Lab shortly following tumor injection and tumor growth was tracked via caliper measurements. Before imaging, mice were anesthetized with gaseous isoflurane (1.5-3%) in O₂, administered using a calibrated vaporizer. Initial anesthesia was delivered in a sealed induction chamber, and unconscious mice were moved into the bowl of the PCT system where continued isoflurane was delivered using a flexible nose cone. To ensure that the mice are stable, medical tape was used to secure the mice onto the scanning bowl.

Mice were imaged with PCT-S approximately every 3 days to track changes in hemoglobin concentration (CtHb) and oxygen saturation (SaO₂) with growth. Tumors were also imaged longitudinally, every 15 minutes over the span of two hours, to detect temporal changes in SaO₂ and CtHb for hypoxia mapping. The latter image protocol intends to capture changes in tumor oxygenation over the course of minutes and hours⁴⁷.

5.2.2.2 Syngeneic MMTV-PyMT

From Lilly Research Labs at Eli Lilly and Co., mammary fat pads on immunocompetent female FVB mice were seeded with MMTV-PyMT fragments, a murine epithelial breast tumor model driven by oncogenic transformation of polyomavirus middle T-antigen. When MMTV tumors reached a volume of approximately 250 mm³, one of four anti-angiogenic drugs was administered. A control cohort received 20 mg/kg of a control antibody, IgG4. Another cohort received an anti-vascular endothelial growth factor drug (DC101) at a concentration of 40 mg/kg. A third cohort received an anti-angiopoietin-2 (Ang2) drug at 20 mg/kg. The final treatment cohort received a combination of DC101 at 40 mg/kg and Ang2 at 20 mg/kg. All drugs were administered intraperitoneally.

MMTV-PyMT-seeded mice were delivered and imaged with PCT-S one-week post-treatment in a blinded study. Mice were anesthetized with gaseous isoflurane (1.5-3%) in O₂, administered using a calibrated vaporizer. Initial anesthesia was delivered in a sealed induction chamber, and unconscious mice were moved into the bowl of the PCT system where continued isoflurane was delivered using a flexible nose cone. To ensure that the mice are stable, medical tape was used to secure the mice onto the scanning bowl. Spectral PCT images were acquired every 15 minutes for two hours to track local changes in hemoglobin concentration and oxygen saturation, which were converted into hypoxia classifications using methods described above.

5.2.3 Imaging Analysis

The following paragraphs detail the imaging processing applied to all following PCT datasets, which were primarily written in MATLAB (R2016 and later).

5.2.3.1 Image Registration

Images within the same dataset, acquired in the same scan, were co-registered using 2D/2D image registration techniques to eliminate rotational offset artifacts in the Nexus128 system. The `imregtform()` function in MATLAB was used to calculate the rigid transformation matrix between 2D ‘moving’ and a ‘fixed’ (target) image slices. This transformation matrix is calculated to minimize the mean squared error between images using a built-in gradient descent optimization algorithm. The optimization calculation was allowed to iterate 300 times, with min/max step lengths of 0.000001 and 0.015 voxels, respectively. These inputs were found to commonly result in sufficient registrations. The rigid transformation matrix is applied to the entire 3D volume of the ‘moving’ image using the `imwarp()` function, and the resulting image data is saved.

For datasets acquired over many scans, that need to be analyzed longitudinally, images were further co-registered using 3D/3D registration techniques to eliminate offsets from the animal motion or placement errors between scans. Here, prior 2D/2D registration guarantees that datasets are self-registered beforehand, thus 3D/3D registration is only needed between one image per dataset. This registration also uses `imregtform()` to calculate a rigid transformation matrix, this time using entire image matrices as ‘moving’ and ‘fixed’ images, using the same gradient descent optimization and parameters. The resulting 3D transformation matrix was applied to all images in the ‘moving’ dataset and saved for further analysis.

5.2.3.2 PCT Calibration

Co-registered images are in units of photoacoustic intensity (I_{PCT}) and must be converted into absorption coefficients (μ_{abs}). This measured absorption coefficient is defined as:

$$\mu_{abs}^{(meas)}(\lambda) = C_{tHb} * (2.303 * 2 * \varepsilon_{HbO_2}(\lambda) * SaO_2 + 2.303 * 2 * \varepsilon_{Hb}(\lambda) * (1 - SaO_2)) \quad (5.1)$$

Where ε is the wavelength-dependent molecular extinction coefficient in M^{-1}/cm for oxygenated and deoxygenated hemoglobin, referenced from the Oregon Medical Laser Center. The constant 2.303 is used to convert the extinction coefficient into an absorption coefficient (mm^{-1})

¹), and the constant 2 is used to account for pathlength differences in absorption due to hemoglobin encapsulation in red blood cells. C_{tHb} is the hemoglobin concentration (M), and SaO₂ is the relative oxygen saturation of hemoglobin – both of which are unknown and must be determined using spectroscopically by sampling photoacoustic image intensities at varying wavelengths. The laser energy absorbed per voxel, as a function of wavelength, is:

$$E_{abs}^{meas}(\lambda) = \Psi_0 * \Delta^2 * (1 - e^{-\mu_{abs}^{meas} * \Delta}) \approx \Psi_0 * \Delta^3 * \mu_{abs}^{meas} \quad (5.2)$$

Where Ψ_0 is the initial photon energy fluence as light enters a voxel (uJ/mm²) and Δ is the voxel length in millimeters.

This energy can be converted into photoacoustic intensity through the use of a Gruneisen parameter, Γ (PU/ μ J), a tissue-dependent parameter that relates the absorption of energy into a change in local pressure, which is linearly dependent on local hemoglobin concentration. This factor was experimentally determined by the Stantz Lab at Purdue University by sampling the change in photoacoustic intensity as a function of hemoglobin concentration in a phantom. Normalizing these measurements to the input laser energy, the Gruneisen parameter was found to be 9.79×10^4 PU/ μ J.

$$I_{PCT} = \Gamma * E_{abs}^{meas} = \Gamma * \Psi_0 * \Delta^3 * \mu_{abs}^{meas} \quad (5.3)$$

Thus, the absorption coefficient in a voxel can be experimentally determined through photoacoustic CT, by also accounting for the power of the laser system and reconstruction parameters.

$$\mu_{abs}^{meas} \approx \frac{I_{PCT}}{\Gamma * \Psi_0 * \Delta^3} \quad (5.4)$$

Energy fluence is estimated using measured power measurements across all relevant wavelengths (P, mW), sampled at the entry of the laser fiber in the photoacoustic system, acquired periodically as the laser output can change from day-to-day. The position and area of the beam ($\pi\sigma^2$, mm²) are measured using a tube phantom filled with india ink, which is translated across the

beam and fitted to a super gaussian. This beam power and position data is saved as a database file for later use. Light attenuation by water is determined using Beer’s Law, using the absorption coefficient of water and depth (z, cm). This water attenuation factor can be pre-incorporated into the PCT data at reconstruction, so care must be taken to ensure that this correction factor is applied exactly once.

$$\Psi_0 \approx \frac{P/10}{\pi * \sigma^2} e^{-\mu_{H2O} * z} \quad (5.5)$$

A MATLAB GUI, PCT_Calibration.m, was written to efficiently apply the above equations to PCT-S datasets to prepare for spectral fitting (Figure 23). This GUI is designed to load a spectral PCT dataset and enable viewing all images for visual confirmation of co-registration. Once registration is confirmed, the GUI prompts the user to designate an ROI for PCT data to be used – this is done by drawing an arbitrary ROI for a large FOV on a single image slice, which is applied to all slices of interest, defined in the GUI as z_min and z_max. A laser database file from the closest date of image acquisition is selected, which is applied to determine Ψ_0 for all relevant voxels. The Gruneisen parameter can be manually overwritten, if different from our default value, defined above. PCT_Calibration then runs to determine μ_a for all voxels within the ROI, for all available image wavelengths, and writes this data out in a Spectra.dat file. A corresponding Spectra.hdr file contains information about Spectra.dat, such as the number of voxels to be analyzed, the PCT wavelengths sampled, and the hemoglobin and deoxyhemoglobin extinction coefficients at those wavelengths. A batch function was written to calculate and write out spectral data files for all PCT-s dataset acquired of the same mouse, on the same day. A function was also written to enable tumor contouring, which is needed for analysis described in the next section.

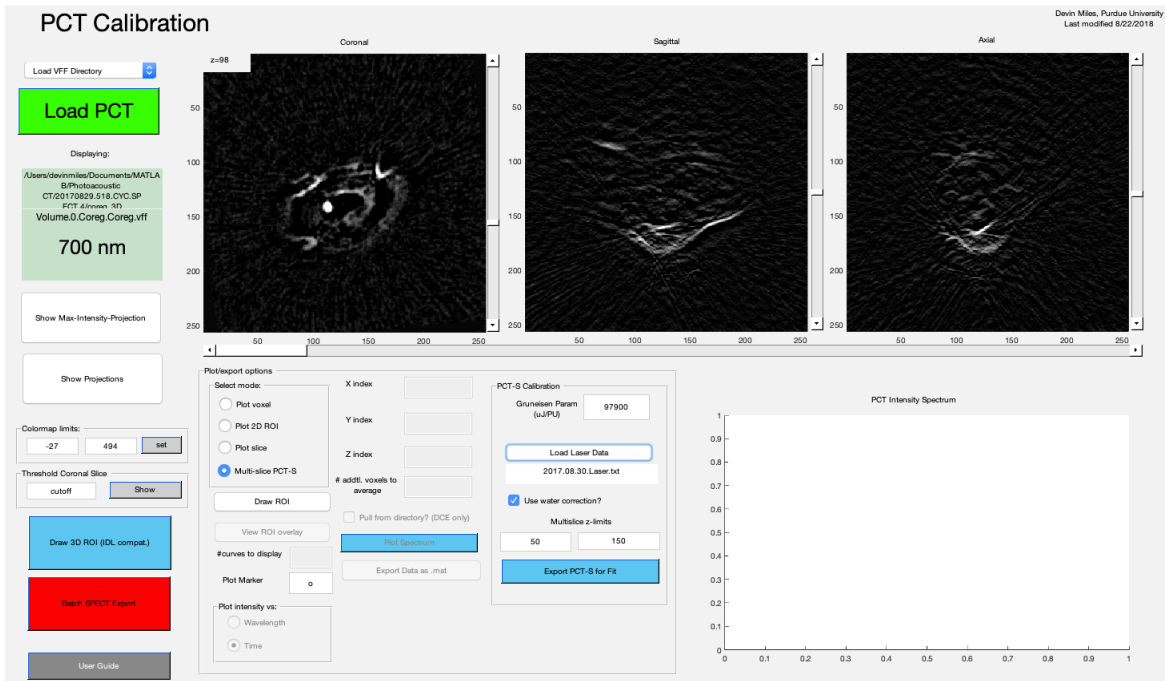


Figure 23. The PCT calibration GUI. Entire PCT-S datasets can be loaded to confirm the success of 2D or 3D coregistration. Once coregistration is confirmed, the PCT-S Calibration function can be used to write a PCT-S spectra data file for fitting and determination of SaO₂, CtHb. PCT-Calibration can be run in batch mode, for datasets that use the same laser data file. A 3D ROI drawing function was designed to contour the tumor. Voxel intensities can be plotted as a function of wavelength to visualize the variability in NIR light absorption, or as a function of time to examine the effects from longitudinal (or potentially, dynamic contrast enhanced) imaging.

Spectra.dat and Spectra.hdr files are passed into SpectraMpfitt.c, a C++ routine developed by K. Stantz to determine C_{Hb} and SaO₂, by nonlinear fitting of μ_{abs} to Eqn. 5.1 to minimize the squared error via Levenberg-Marquardt algorithm. The outputs from each dataset are a Fit.dat file containing SaO₂, CtHb, reduced Chi-square, and error for each voxel within the Spectra.dat.

5.2.3.1 PCT Analysis – single image sets

A MATLAB function was written to process and analyze data from Fit.dat outputs from spectral PCT fitting. This function reads in a Fit.dat file and restructures the tabulated data into 3D matrices of SaO₂, CtHb, reduced chi squared (Chisq), and error. A Chisq cutoff is implemented to omit data that was fitted badly from further analysis. The tumor surface margin is loaded and used to define ‘core’ and ‘periphery’ regions in each spectral fit, through use of a built-in watershed function, bwdist(), which finds the distance between a voxel and an ‘edge.’ The tumor cores were

defined as voxels > 2 mm from the tumor surface. Analyzed data is limited to the most superficial 4 mm of each tumor, due to limitations in photon energy fluence modeling at increasing depth.

Fitted data matrices are used to create histograms of SaO₂, CtHb, and Chisq for the core, periphery, and whole tumor. The SaO₂ histogram is also converted into a cumulative histogram and used to calculate HF5, the hypoxic fraction at 5% SaO₂. The vascular and avascular fractions are determined by tracking the number of voxels containing or not containing hemoglobin, respectively. Average values for SaO₂, HF5, CtHb, and vascular/avascular fraction are saved plotting.

5.2.3.1 PCT Analysis – longitudinal image sets and hypoxia classification

Another MATLAB GUI, LongitudinalPCTAnalysis.m, was created to analyze multiple PCT-S image sets of the same tumor on the same day and perform rudimentary hypoxia classification (Figure 24). The software used the filename of a single PCT-S dataset, containing Fit.dat data, to parse a directory for all datasets acquired on the same day. All Fit.dat files are all loaded and to calculate the average, max-intensity, and standard deviation of SaO₂ and CtHb. The tumor surface contours are used to exclude voxels outside of the tumor volume. Single-voxel data for SaO₂ and CtHb over all time points can be easily plotted.

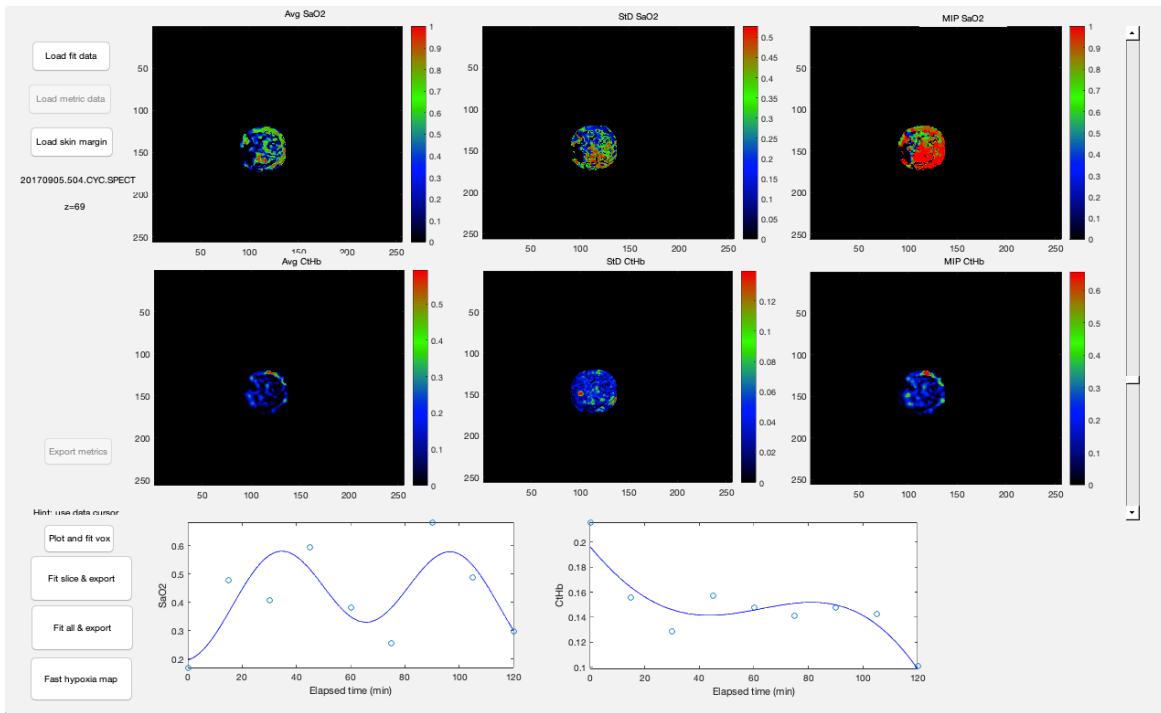


Figure 24. The longitudinal PCT analysis GUI. PCT-S data that has been fitted to Eqn. 5.1 can be loaded to visualize and calculate changes in SaO2 and CtHb over time. The displayed images are average, standard deviation, and maximum intensity of the SaO2 (top row) and CtHb (middle row) over time. Data from individual voxels can be plotted (bottom row) as a function of time for a direct visualization of SaO2/CtHb variability with time. Using an SaO2 threshold in voxels that always contain hemoglobin, hypoxia classification can be determined here.

Hypoxia classification was assessed on a voxel-by-voxel basis by examining SaO2 in all voxels containing hemoglobin ($CtHb > 0$). An SaO2 threshold was implemented for a voxel to be considered hypoxic. This threshold was set to $SaO2 < 0.2$, which was experimentally measured via Oxylite oximeter probe to correspond to partial pressure of oxygen of 10 mmHg by Justin Sick. This oxygen partial pressure is a classical threshold for a cell to be considered hypoxic. A voxel was considered chronically hypoxic if its SaO2 was always measured above this threshold, and normoxic if its SaO2 was always above. If at any point a voxel's SaO2 was above and below this threshold, the voxel was considered acutely hypoxic. These classifications were determined for all voxels within a user-defined volume of interest and saved as a label map for analysis. The relative fraction of acute hypoxia, chronic hypoxia, and normoxia was calculated for the most superficial 4mm of the tumor, determined using the tumor contours.

5.3 Results

A representative image describing the hypoxia classification is shown in Figure 25, using the classification parameters described above.

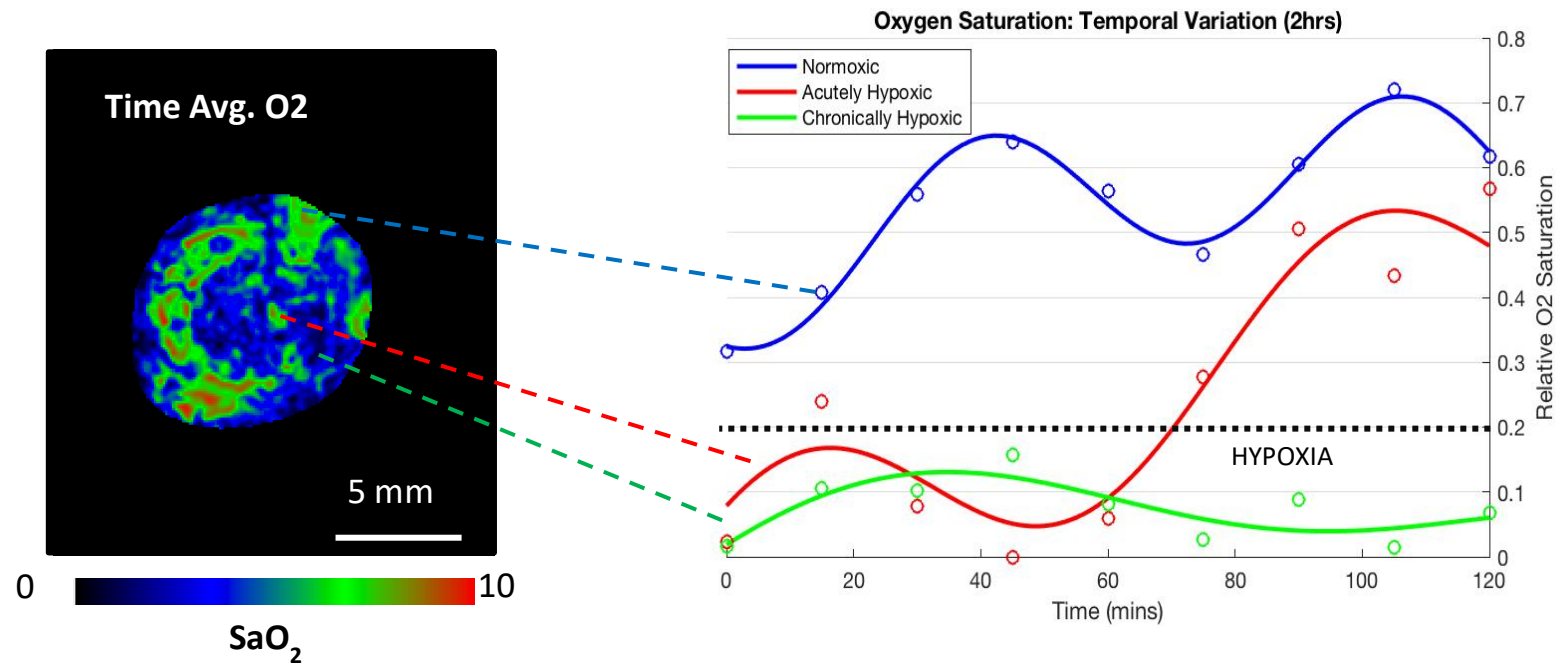


Figure 25. Illustration of hypoxia classification based on voxel SaO₂, in voxels containing hemoglobin. If the SaO₂ is always under the hypoxia threshold (0.2) during longitudinal scanning, it is considered chronically hypoxic. If the SaO₂ is both above and below the threshold at some point during scanning, it is considered acutely hypoxic. If the SaO₂ is always above the threshold, it is considered normoxic.

5.3.1 Syngeneic MC38

Exponential tumor growth was observed, with a large tumor size differential appearing at 10 days following tumor seeding (Figure 26). This is due to small differences in the number of cells seeded, which is common in cell lines with a short doubling time. Representative hypoxia maps for a single MC38 tumor, imaged at different stages of growth is shown in Fig. 27. Average CtHb and SaO2 tended to decrease with tumor growth, as HF5 increased.

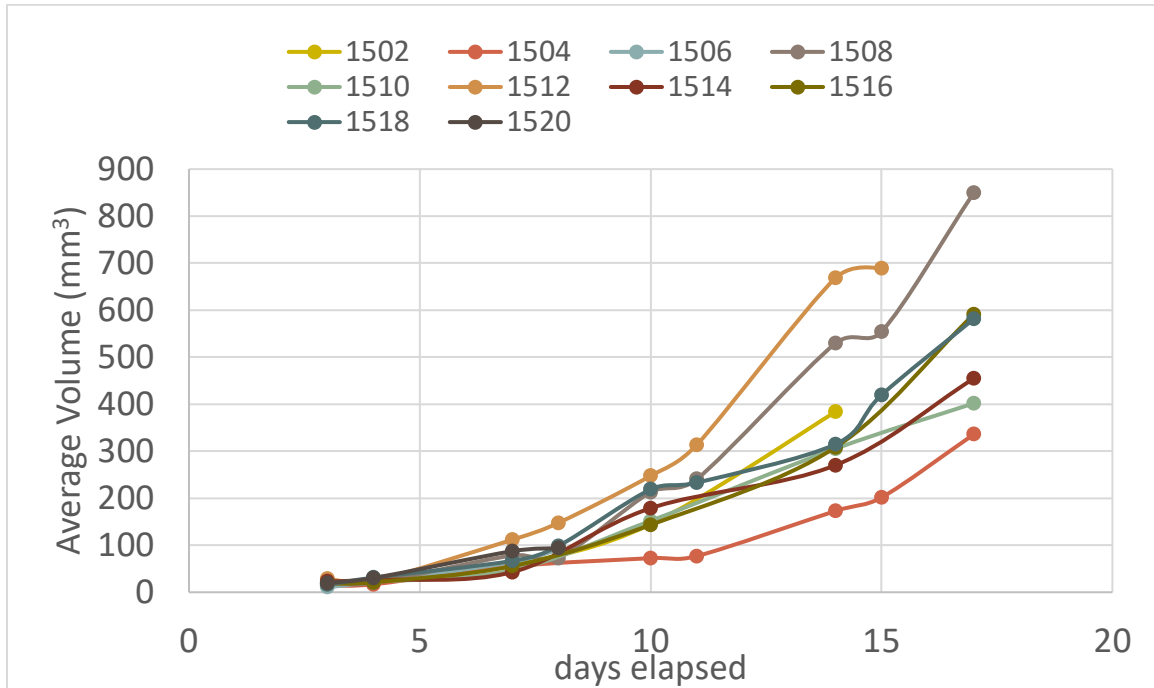


Figure 26. MC38 tumor growth over time. Tumor sizes were measured using calipers.

From hypoxia classification, acute hypoxia is present in all tumors throughout growth. As MC38s grow larger, cells being to reside outside of the diffusion length of oxygen from perfused blood vessels, leading to some occurrence of chronic hypoxia. The fraction of voxels classified as acutely hypoxic tend to decrease as tumor size increases. The normoxic fraction of MC38 tumors was roughly constant with growth. The hypoxia classifications for the whole MC38 cohort, for all longitudinal image studies, can be seen in Fig. 28.

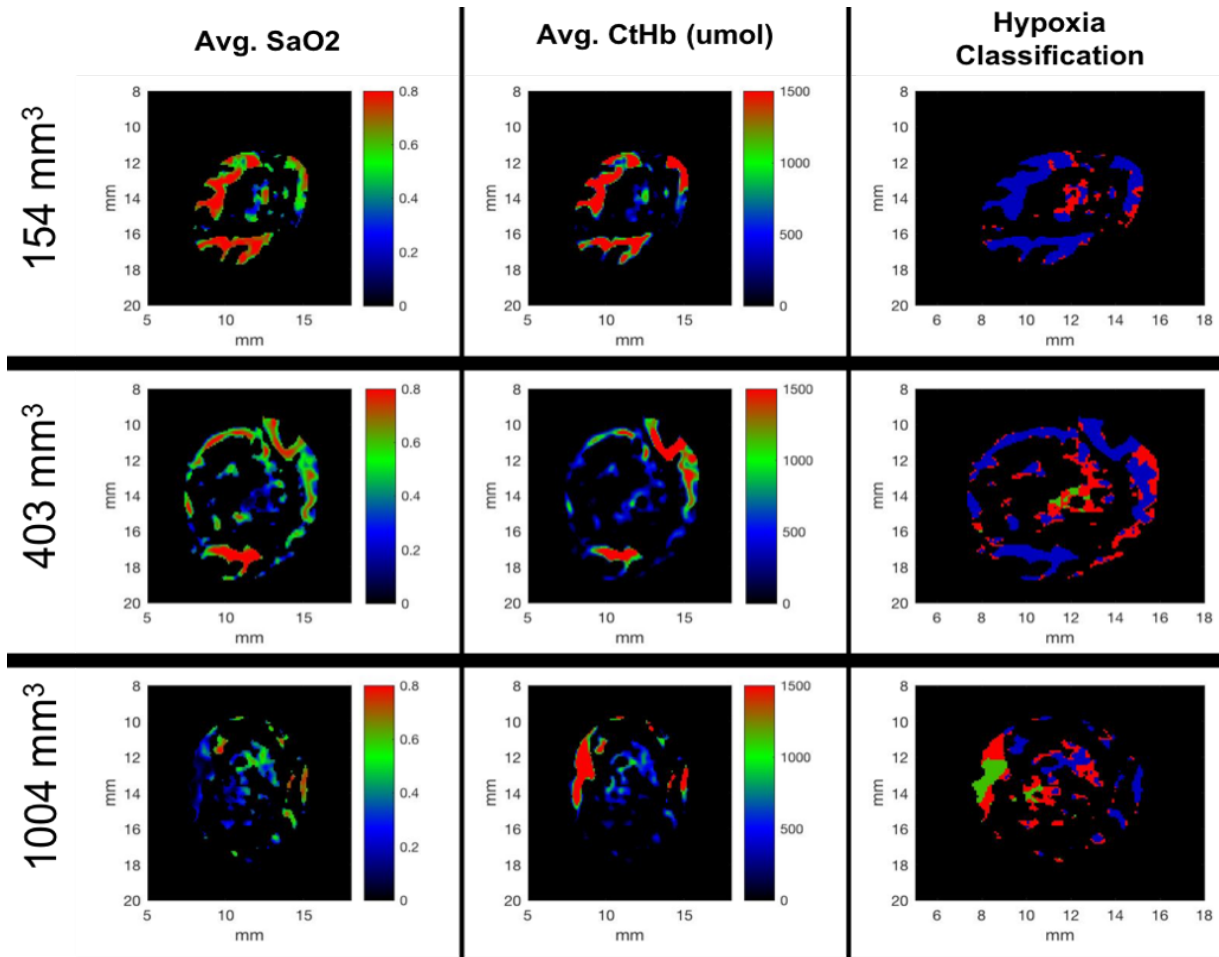


Figure 27. Representative PCT maps for a single MC38 tumor imaged on different days. For hypoxia classification, blue voxels are normoxic, red voxels are acutely hypoxic, and green voxels are chronically hypoxic. The SaO₂ and CtHb were, on average, highest for the earliest scans where the tumor was smallest. As the tumor volume increases, SaO₂ and CtHb decreased. As a result, only some acute hypoxia was classified in the tumor early on. With growth, the tumor become more acutely hypoxic, eventually developing regions of chronic hypoxia.

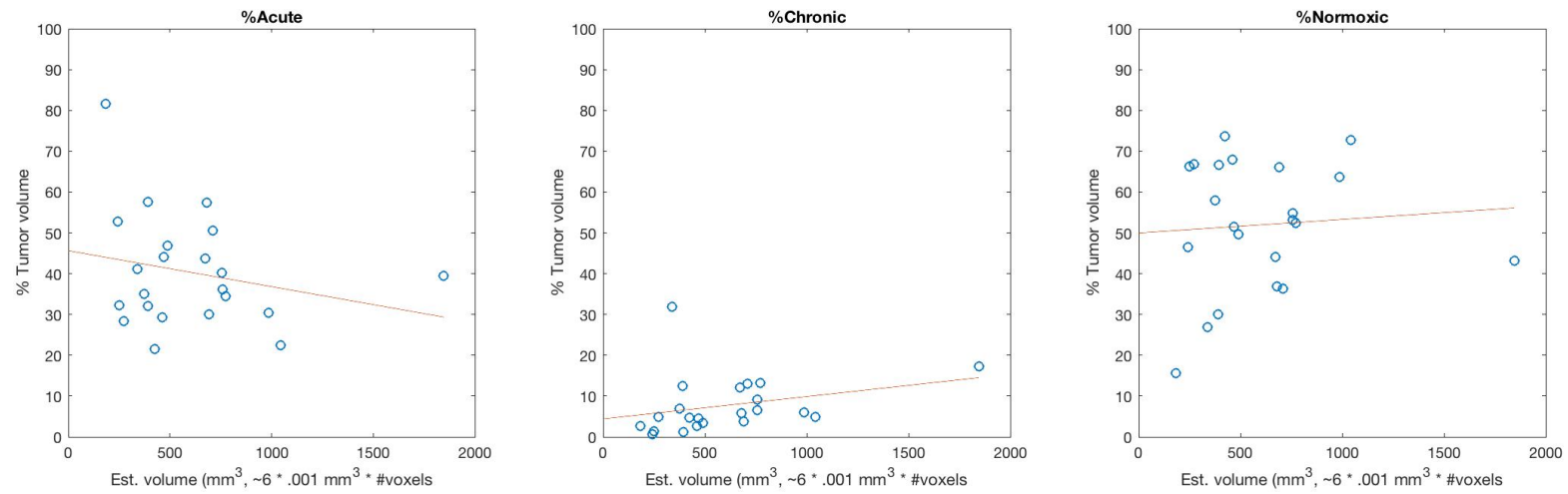


Figure 28. Trends in tumor hypoxia for MC38 tumors. Data shown is taken from longitudinal scans for the entire cohort of tumors. As demonstrated before, hypoxia in smaller tumors is predominantly acute, and chronic hypoxia appears as the tumor is allowed to grow. The relative amount of normoxic tissue was roughly constant.

5.3.2 Syngeneic MMTV-PyMT

All anti-angiogenic drugs resulted in a suppression of tumor growth measured at the time of imaging. Ang2 treatment alone resulted in the largest growth delay, but there is no statistically significant difference between treatment groups. Measurements can be seen in Fig. 28.

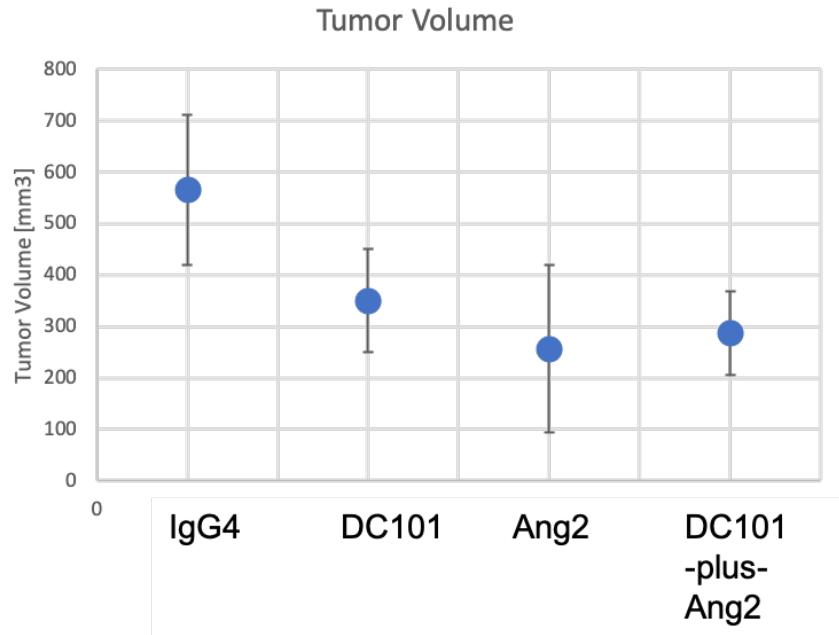


Figure 29. MMTV-PyMT tumor volumes, measured using calipers on the day of imaging. All treatment groups saw a reduction in tumor growth by the time of imaging, relative to the IgG4 control. Tumors treated with Ang2 alone saw the highest degree of growth suppression, but this was not significantly different from the other treatment groups.

Tumors treated with DC101 alone were consistently more highly oxygenated, but also had the lowest hemoglobin concentrations and the highest typical avascular fractions. On average, the DC101-treated tumors presented the lowest hypoxic fraction of all treatment groups, and the combination of DC101 and Ang2 resulted in the highest hypoxic fraction. Tumors treated with the combination therapy presented the highest total fraction of acute hypoxia, but the relative fraction of chronic hypoxia was not significantly different from the control group. DC101-treated tumors, however, had the lowest fractions of acute and chronic hypoxia across all treatment groups. Tumors treated with Ang2 alone were not significantly different from the control tumors in any metric. Box and whisker plots of SaO₂, CtHb, relative acute and chronic hypoxia, and normoxia are shown in Figures 29-33.

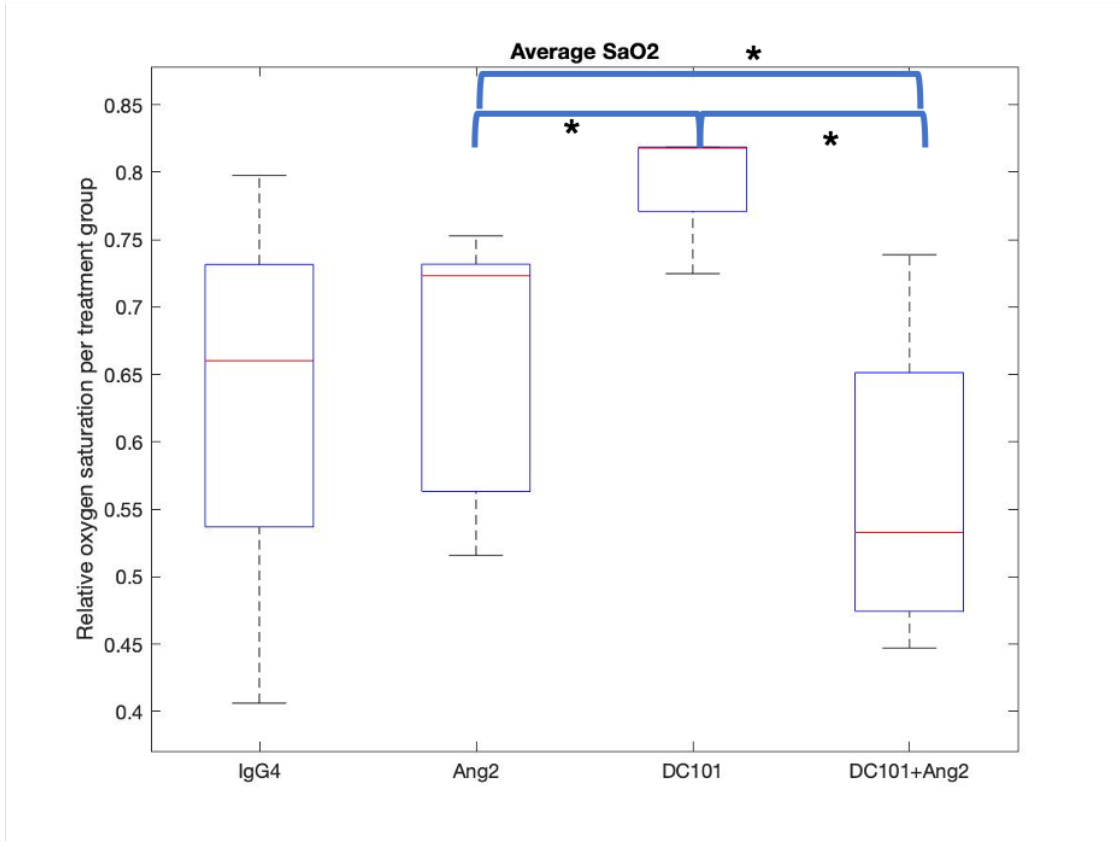


Figure 30. SaO2 trends for MMTV-PyMT treated with anti-angiogenic drugs. DC101-treated tumors had a significantly higher SaO2 than those treated with Ang2 or combination therapy. DC101+Ang2-treated tumors had a significantly lower SaO2 than DC101 or Ang2 alone. (*P < 0.05; paired t-test)

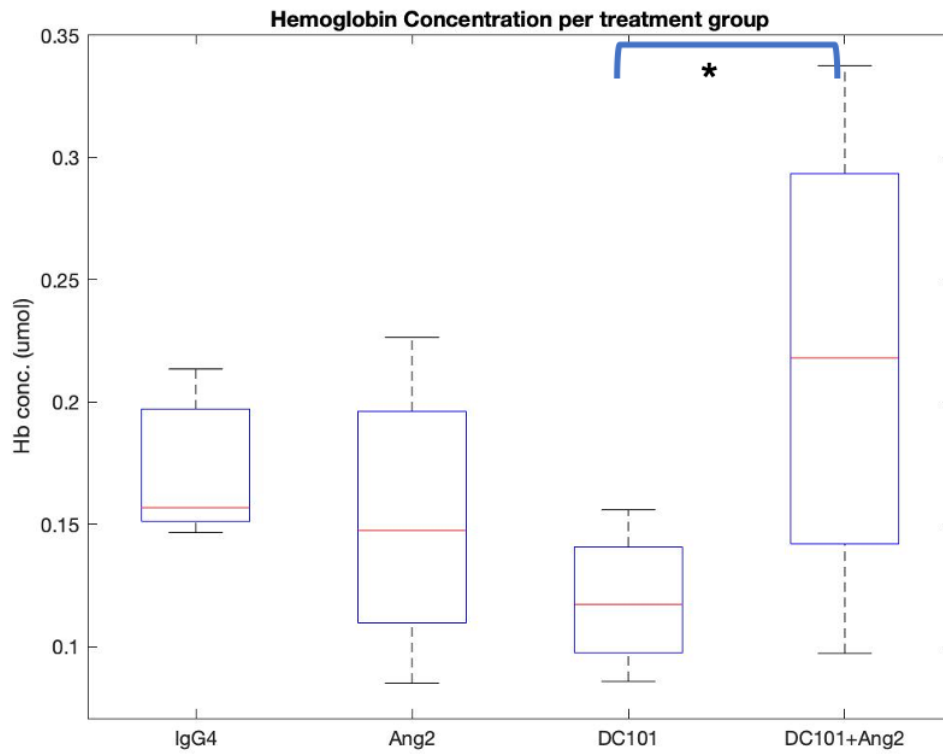


Figure 31. Hemoglobin concentration trends for MMTV-PyMT tumors treated with anti-angiogenic drugs. DC101-treated tumors had a significantly lower CtHb than those treated with combination therapy. (*P < 0.05; paired t-test)

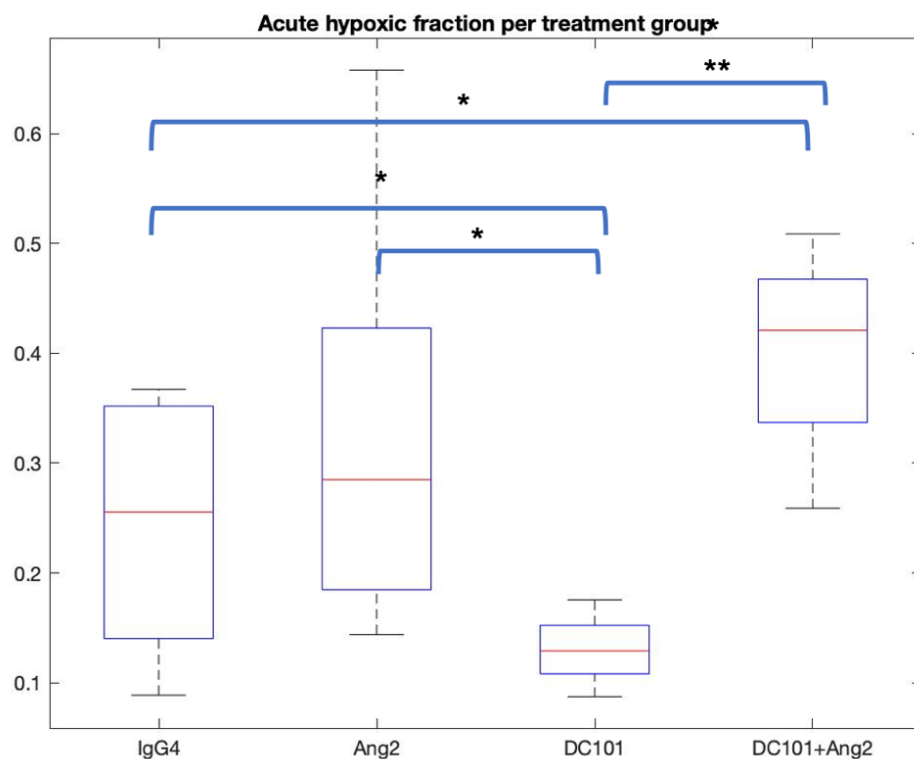


Figure 32. Acute hypoxia trends for MMTV-PyMT tumors treated with anti-angiogenic drugs. DC101-treated tumors had a significantly lower fraction of acute hypoxia than all other groups. DC101+Ang2-treated tumors had a significantly higher fraction of acute hypoxia than DC101 and the control but were not statistically different from tumors treated with Ang2 alone. (*P < 0.05; **P < 0.01; paired t-test)

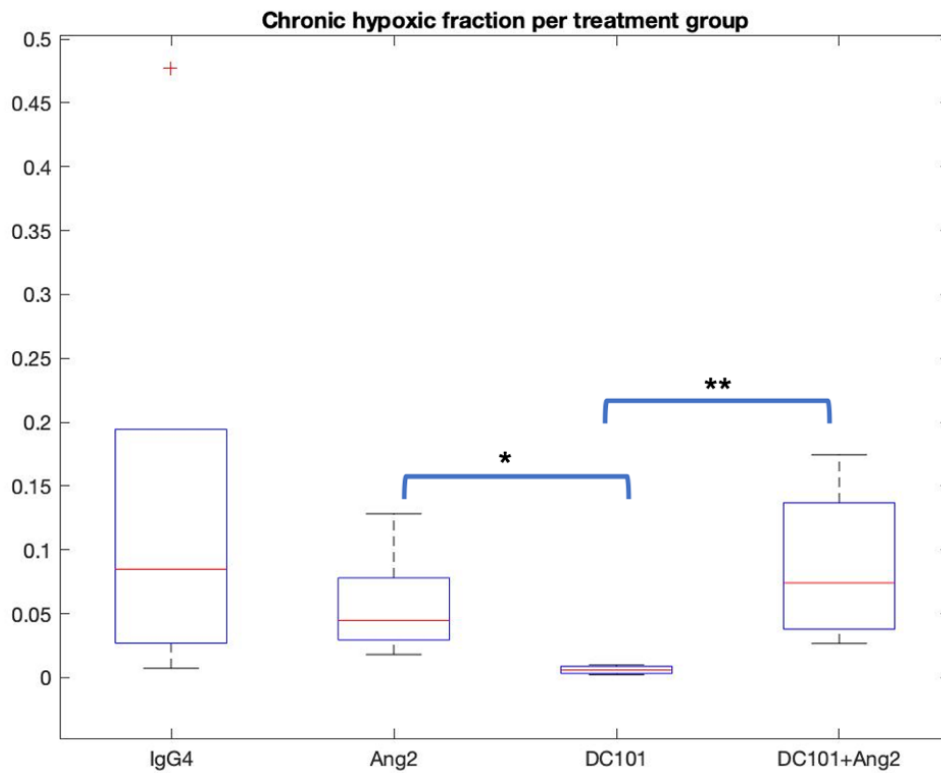


Figure 33. Chronic hypoxia trends for MMTV-PyMT tumors treated with anti-angiogenic drugs. DC101-treated tumors had a significantly lower fraction of chronic hypoxia than all other groups. (*P < 0.05; **P < 0.01; paired t-test)

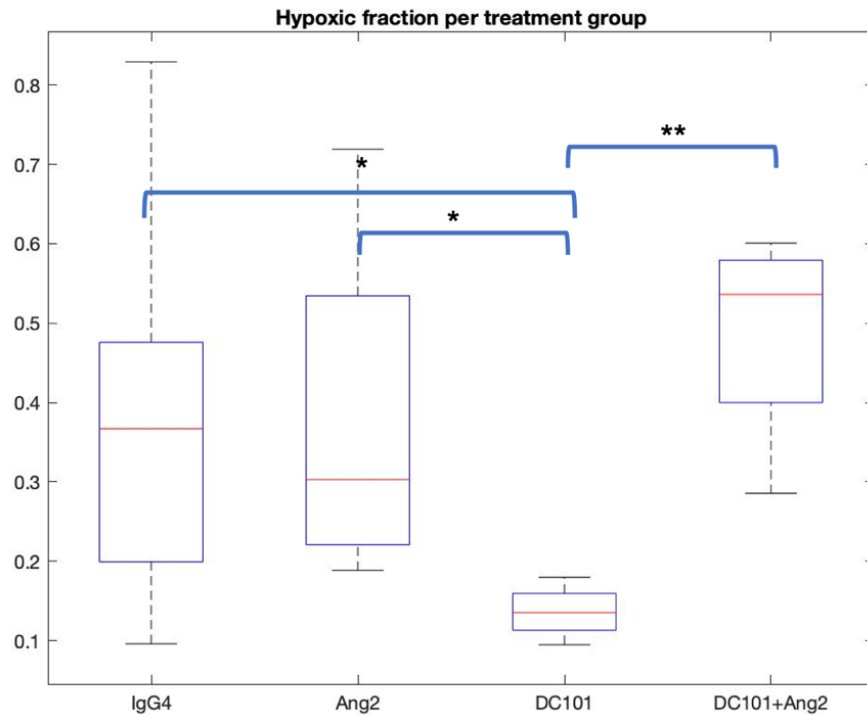


Figure 34. Overall hypoxic fraction trends for MMTV-PyMT tumors treated with various anti-angiogenic drugs. DC101-treated tumors had a significantly lower hypoxic fraction than all other groups. On average, MMTV-PyMT tumors had the highest hypoxic fraction following combination therapy, but this was not statistically different from Ang2 alone or the control group. (* $P < 0.05$; ** $P < 0.01$; paired t-test)

5.4 Discussion

Tumor hypoxia is of immense interest in cancer research, due to its implications in treatment resistance, metastatic potential, cancer recurrence, and overall survival⁸⁵. Many clinical approaches to hypoxia imaging have been developed, such as F-MISO PET, DCE-MRI, and BOLD MRI, each with their own strengths and weaknesses⁵⁵. Photoacoustic imaging is capable of overcoming most of the weaknesses associated with these clinical techniques, by directly measuring in-vivo hemoglobin concentration and oxygen saturation quickly, non-invasively, and at high spatial resolutions. Here, a technique has been developed to image a tumor longitudinally over time to measure variations in oxyhemoglobin saturation on a voxel-by-voxel basis, and further, to distinguish the hypoxic status of a tumor at high spatial resolution. This method to

classify tumor hypoxia was applied to two distinct tumor models. The MC38 cohort was used to examine changes in tumor hypoxia with growth, demonstrating the presence of acute hypoxia all throughout growth, with chronic hypoxia predominantly appearing in larger tumors. The MMTV-PyMT cohort demonstrated that this technique is capable of distinguishing changes in the tumor microenvironment as a result of treatment with anti-angiogenic drugs, such as VEGF2 and Ang2 suppressors.

Spatial mapping of tumor hypoxia offers a unique perspective to tumor imaging that could be used to guide radiation therapy planning. Chapters 3 and 4 developed empirical models of radiation-induced immunogenicity enhancement, which both predict that higher doses are required to stimulate an immune response through STING.

CHAPTER 6. DISCUSSION

Immunotherapy is an exponentially growing facet of oncology, now considered the fourth pillar of cancer care alongside surgery, radiation therapy, and chemotherapy⁸⁶. While the efficacy of immunotherapy drugs has dramatically improved in recent years, most solid tumors remain unresponsive to immunotherapy alone¹⁷. An increasingly common approach to enhance the efficacy of immunotherapy is to provide concurrent radiation to stimulate immunogenic cell death, effectively enhancing ‘visibility’ of a dying tumor cell to the surveilling immune system⁷⁷. The effects of radiation action on immunogenic cell death can be attributed to the activation of the STING pathway, which originates from extensive DNA damage⁸⁷. Many clinical and preclinical works have demonstrated the synergistic effects of radio-immunotherapy with respect to cancer treatment, across a wide variety of disease sites, tumor models, and cell lines^{22,35,36}. Laboratory experiments have shown a dose-dependent response, with pro-immunogenic effects only possible within a narrow window of doses, typically around 8 Gy of low-LET radiation. Limited prior data has explored the effects of radiation quality, ionization density, particle typing, or hypoxia on radiation-enhanced immunogenicity. While direct study of immunotherapy drugs is outside of the scope of this work, central themes to this thesis are the study of pro-inflammatory and anti-inflammatory signals that can result from radiation-induced DNA damage, and how to leverage these signals to potentially optimize abscopal effects.

We initially used MCDS as a means of simulating initial DNA damage in irradiated cell lines and applied this damage modeling to published data³⁵ on the dose response of cytosolic dsDNA and exonuclease Trex1. Solely based on initial DNA damage, our models predicted an RBE-based ‘shift’ in immunogenic signaling. Higher-LET radiation, which is capable of more-dense ionization interactions and induction of more-complex (and less repairable) DNA damage, was modeled to drive accumulation of cytosolic dsDNA at lower physical doses, with the caveat of narrowing the window of elevated cytosolic dsDNA, thus IFN β , due to upregulation of Trex1. Conversely, hypoxic cells, which have a lower RBE due to lack of oxygen fixation of DNA damage, were expected to accumulate cytosolic dsDNA at higher doses. These results follow expectations from textbook radiation biology, for endpoints of DSB induction and clonogenic cell death, but little published evidence exists for verification.

To verify and refine these models, an in vitro study of radiation-induced immunogenicity was performed in non-viral MCC, examining the dose responses of cytosolic dsDNA, IFN β , and exonuclease Trex1 following low-LET via SARRP x-rays and high-LET radiation via fast neutrons. While the data from cytosolic dsDNA measurements were inconclusive due to experimental difficulties, the endpoints of IFN β and Trex1 showed a differential response between radiation modalities, with an RBE_{IFN β} of 2.4 and a four-fold higher Trex1 upregulation per dose for neutrons relative to x-rays, measured over replicate experiments. This data was used to build empirical DNA damage-based models of IFN β and Trex1 using MCDS, as before. Empirical models were further applied Monte Carlo particle transport simulations of 6 MV x-rays and 50 MV fast neutrons, as well as proton, carbon, and alpha particle beams with ranges of 10 cm in water. The charged particle beams demonstrated a capacity to locally stimulate an immune response at the end of their range, and the uncharged beams were able to more uniformly stimulate IFN β with depth.

The in vitro results confirm the prior assumptions that there is a relation between initial DNA damage and immunogenicity, and that it directly follows established trends of relative biological effectiveness with respect to DSB induction, at normoxia. Secondly, while uncharged radiation modalities are able to more uniformly stimulate an immunogenic response, ion beams are capable of localized immune stimulation near the distal edge of their Bragg peaks– enabling treatment plan optimization to selectively stimulate arbitrary regions of a tumor. This becomes particularly attractive in the context of adaptive therapy or ‘biologically-guided’ therapy, providing an endpoint for which radiation might act on difficult-to-treat regions within a tumor. As stated previously, tumor hypoxia not only causes treatment resistance by lack of oxygen fixation of damaged DNA but drives changes in cellular phenotype making cancer cells more stem-like, thus more prone to local or distant recurrence. Thus, ion beams are uniquely suited to both target and escalate dose to hypoxic regions within a tumor, enabling immunogenicity enhancement of these potentially metastatic cells.

To support the end of targeting the hypoxic niche of tumors with immunostimulatory radiation, photoacoustic CT imaging techniques were developed with the intent of overcoming weakness associated with more clinically oriented PET or MRI techniques, namely poor spatial

resolution, limited temporal resolution, invasiveness, and requirement of additional contrast agents. Our approach utilizes longitudinal PCT-S scans to detect variations in local hemoglobin concentration and oxygen saturation on a voxel-by-voxel basis over the span of two hours. A hypoxia classification system was designed from the oxygen saturation measurements in PCT voxels containing hemoglobin. These techniques were applied to syngeneic MC38 and MMTV-PyMT tumor models to track changes in hypoxic status as a function of tumor growth and following anti-angiogenic therapy, respectively. In MC38-seeded mice, longitudinal PCT detected strong prevalence of acute hypoxia present in all tumors, with chronic hypoxia emerging over time with growth. In MMTV-PyMT-seeded mice, longitudinal PCT revealed that tumors treated with DC101 (anti-VEGF2) had a significantly lower hypoxic fraction than those treated with Ang2 (anti-angiopoietin 2) or a combination of DC101 and Ang2. Tumor hypoxia was classified in both models on the scale of 100 micrometers.

Altogether, the results from this thesis present the tools to model and enable immune stimulation of hypoxic cells within a tumor by radiation therapy. While enticing, successful clinical implementation many barriers must be first overcome. Photoacoustic CT is primarily a preclinical imaging modality, due to limitations in imaged field-of-view and depth of penetration. The longitudinal scanning technique applied here would need to be adapted to utilize clinical imaging equipment, such as CT, MRI, or ultrasound. Similarly, the cost effectiveness of a long scanning series would be prohibitive. Human patients also aren't typically anesthetized during diagnostic imaging procedures. Long time periods under immobilization are both uncomfortable to the patient and invite patient motion.

Clinical iontherapy in the US is currently restricted to protons, although carbon ion facilities are in-development. Range uncertainties in proton therapy remain an unsolved concern, arising from limitations in dose calculation and stopping power approximations from patient CT scans⁸⁸. Numerous technical developments have arisen to solve this problem. The only current clinical solution is applying dual-energy CT, which acquires scans of a patient at two x-ray energies and applies the difference in measured Hounsfield units to determine the average electron density in a voxel^{89,90}. Thermoacoustic (aka Radiation-acoustic) techniques are currently under development by Purdue University to apply technology comparable to PCT, for high-resolution

measurement of energy absorption in water⁹¹. Perhaps the most direct approach is proton CT, which utilizes high-energy proton transmission (much like x-rays) to determine the water-equivalent path length of protons through a medium, which can be reconstructed via backprojection (like x-rays) to map out stopping power ratios in a patient^{92,93}. All of these techniques are promising and have functioned well in laboratory experiments, but full clinical implementation has not been achieved.

One unexplored topic is measurement of the effects of tumor hypoxia directly on the action of the STING pathway. This is, in part, due to difficulties in experimentation with hypoxic cell cultures⁹⁴. A common approach to studying hypoxia is to incubate cells in growth medium supplemented with cobalt-chloride (CoCl₂), which acts to stabilize HIF-1a, inducing a chemical hypoxia⁹⁵. While this enables simple handling of the cells, this does not remove oxygen from the experiments altogether, and oxygen fixation of DNA damage can still occur. A more direct approach to hypoxic cell culture is to induce cell plates with a low-O₂ concentration of gas for an extended time. However, the cell plates must be kept in an air-tight container perfused with hypoxic gas, which makes hands-on experimentation difficult outside of a glove box. Upcoming experiments will aim to explore STING responses in hypoxic cells using a hybrid approach, utilizing growth medium supplemented with an oxygen scavenger⁹⁶ (sodium sulfite). At the appropriate concentrations, sodium sulfite limit dissolved oxygen in a fluid medium for an extended time, allowing cell plates to be temporarily handled outside of a hypoxic gas induction chamber.

From prior literature, it is anticipated that hypoxia will change the radiation-induced immunogenic response in ways beyond a simple dose shift. A study from Wu et al.⁸², demonstrated a hypoxia-dependent suppression of cGAS, the cytosolic dsDNA sensor upstream of STING. This immunosuppression was a result of overexpressed micro-RNA 25 and 93, which was demonstrated to suppress downstream IFN β secretion in vitro, leading to decreased CD8⁺ T-cell population in vivo. It is likely that, if STING is able to become activated following radiation, hypoxic cells will secrete lower amplitudes of IFN β . It is similarly unclear how hypoxia modifies Treg1 upregulation³⁷.

CHAPTER 7. CONCLUSIONS AND FUTURE WORKS

This work presents compelling evidence for radiation to boost the efficacy of immunotherapy and supports the hypothesis that radiation quality can influence subsequent immunogenic response. This was demonstrated through both DNA damage modeling and *in vitro* experimentation, showing a predictable ‘shift’ in immunogenicity following radiation exposure, that appears to directly correlate with the number of DNA DSB. This result has immense clinical and preclinical implications, that radiation therapy can theoretically be prescribed with not just curative, but pro-immunogenic intent. Current clinical trials are exploring this relationship between radiation and immunotherapy, and we believe that the concepts in this thesis can be extended to further explore other facets of radiation oncology, with the intent of improving the therapeutic advantage of combination therapy.

A natural next step will be translation of the *in vitro* assays described in Chapter 4 into *in vivo* models. Immunocompetent mice can be seeded with murine cancer cells that have been proven to have intact cGAS-STING signaling and irradiated to immuno-stimulatory doses as demonstrated through *in vitro* study. Small animal irradiators, such as the Xstrahl SARRP, have onboard CBCT systems suitable for image guided radiation therapy, with radiation fields as small as 1 mm diameter. Further, small-animal IGRT systems are capable of plan contouring based on non-CT images – PCT techniques developed in Chapter 5 can be applied to design hypoxia-guided radiation delivery. However, this introduces an array of challenges associated with treatment verification and small-field dosimetry. Nevertheless, study of radiation-enhanced immunogenicity in an animal model will enable more thorough analysis of post-radiation effects on cancer immune recognition, which can extend to assess dendritic cell infiltration, CD8⁺ T-cell priming, regulatory T-cell immunosuppression, and efficacy of varying immunotherapy agents.

Only two endpoints of pro-inflammatory and anti-inflammatory signaling were examined in this thesis, but numerous other endpoints may be of-interest. For instance, STING is triggered by accumulation of cytosolic dsDNA, which is delivered from the nucleus primarily through unstable, ‘leaky’ micronuclei. Micronucleus assay is a common metric for assessing DNA damage via immunofluorescence, comparable to phosphorylated histone H2AX. Further, activity of cGAS

binding to dsDNA could be assayed in parallel as an upstream indication of STING activation. The integrity of micronucleus membranes could be assessed through examination of Lamin A. Alternatively, inflammatory transcription of IRF3 and NF- κ B could be studied using PCR techniques, as well as gene encoding for IFN β , Trex1, or practically any other cytokine produced through cGAS-STING. Radiation-induction of all of these factors will likely vary based on particle LET and cellular oxygenation and may reveal further details on how this pro-immunogenic response could be triggered.

The effects of varying dose rates on radiation-induced STING signaling will be a topic of further study, particularly in the context of FLASH radiation therapy. *In vivo* study of radiation delivered at ultra-high dose rates (> 40 Gy/s) has been demonstrated to preferentially spare normal tissues while preserving tumor control at equivalent physical doses, relative to conventional dose rates⁹⁷. A common theory for this differential effect is that nearly instantaneous radiation delivery damages fewer circulating lymphocytes, limiting systemic immunosuppression. This has, in part, been confirmed *in vivo*, where enhanced CD8⁺ T-cell accumulation has been observed following irradiation of immunocompetent mouse tumor models⁹⁸. However, more studies are needed to further explore the inflammatory response of cancer cells following FLASH radiation.

Current efforts are probing the effects of DNA damage response inhibitors, such as ATR inhibitors, on subsequent immunogenic signaling. As an example, preliminary study has revealed that DNA repair in cancer cells is more highly dependent on ATR kinases than healthy tissues. Inhibition results in enhanced immunogenic cell death following DNA damage by low-LET radiation, with preferential enhancement in cancer cells. It is unclear, but testable, if high-LET radiation offers further enhancement in immunogenic cell death in combination with damage response inhibitors.

REFERENCES

1. Siegel RL, Miller KD, Jemal A. Cancer statistics, 2020. *CA Cancer J Clin.* 2020;70(1):7-30. doi:10.3322/caac.21590
2. Goodman PC. Perspective The New Light: *Discov Introd X-Ray.* 1995;(March).
3. Grubbe EH. X-rays in the treatment of cancer and other malignant diseases (1866-1922). *Med Rec.* 1902;62(18):692.
<https://search.proquest.com/openview/c2675b50d349ef4da14b78fb1526daac/1?pq-origsite=gscholar&cbl=40146>.
4. Thwaites DI, Tuohy JB. Back to the future: The history and development of the clinical linear accelerator. *Phys Med Biol.* 2006;51(13):343-362. doi:10.1088/0031-9155/51/13/R20
5. MOLE RH. Whole body irradiation; radiobiology or medicine? *Br J Radiol.* 1953;26(305):234-241. doi:10.1259/0007-1285-26-305-234
6. Nobler MP. The Abscopal Effect in Malignant Lymphoma and Its Relationship to Lymphocyte Circulation. *Radiology.* 1969;93(2):410-412. doi:10.1148/93.2.410
7. Nikitaki Z, Mavragani I V., Laskaratou DA, et al. Systemic mechanisms and effects of ionizing radiation: A new “old” paradigm of how the bystanders and distant can become the players. *Semin Cancer Biol.* 2016;37-38:77-95. doi:10.1016/j.semcancer.2016.02.002
8. Chen DS, Mellman I. Oncology meets immunology: The cancer-immunity cycle. *Immunity.* 2013;39(1):1-10. doi:10.1016/j.immuni.2013.07.012
9. Hanahan D, Weinberg RA. Hallmarks of Cancer : The Next Generation. *Cell.* 2011;144(5):646-674. doi:10.1016/j.cell.2011.02.013
10. Chen L, Han X. Anti – PD-1 / PD-L1 therapy of human cancer : past , present , and future. *J Clin Invest.* 2015;125(9):3384-3391. doi:10.1172/JCI80011.by
11. Kim JR, Moon YJ, Kwon KS, et al. Tumor infiltrating PD1-positive lymphocytes and the expression of PD-L1 predict poor prognosis of soft tissue sarcomas. *PLoS One.* 2013;8(12):1-9. doi:10.1371/journal.pone.0082870
12. Twyman-Saint Victor C, Rech AJ, Maity A, et al. Radiation and dual checkpoint blockade activate non-redundant immune mechanisms in cancer. *Nature.* 2015;520(7547):373-377. doi:10.1038/nature14292

13. Chen DS, Mellman I. Elements of cancer immunity and the cancer-immune set point. *Nature*. 2017;541(7637):321-330. doi:10.1038/nature21349
14. Hoos A. Development of immuno-oncology drugs-from CTLA4 to PD1 to the next generations. *Nat Rev Drug Discov*. 2016;15(4):235-247. doi:10.1038/nrd.2015.35
15. Egen JG, Kuhns MS, Allison JP. CTLA-4: New insights into its biological function and use in tumor immunotherapy. *Nat Immunol*. 2002;3(7):611-618. doi:10.1038/ni0702-611
16. Tumeh PC, Harview CL, Yearley JH, et al. PD-1 blockade induces responses by inhibiting adaptive immune resistance. *Nature*. 2014;515(7528):568-571. doi:10.1038/nature13954
17. Haslam A, Prasad V. Estimation of the Percentage of US Patients With Cancer Who Are Eligible for and Respond to Checkpoint Inhibitor Immunotherapy Drugs. *JAMA Netw open*. 2019;2(5):e192535. doi:10.1001/jamanetworkopen.2019.2535
18. Reynders K, Illidge T, Siva S, Chang JY, De Ruyscher D. The abscopal effect of local radiotherapy: Using immunotherapy to make a rare event clinically relevant. *Cancer Treat Rev*. 2015;41(6):503-510. doi:10.1016/j.ctrv.2015.03.011
19. Becker JC, Stang A, Decaprio JA, et al. Merkel cell carcinoma. *Nat Rev Dis Prim*. 2017;3(Mcc):1-17. doi:10.1038/nrdp.2017.77
20. Lipson EJ, Vincent JG, Loyo M, et al. PD-L1 expression in the Merkel cell carcinoma microenvironment: association with inflammation, Merkel cell polyomavirus and overall survival. *Cancer Immunol Res*. 2013;1(1):54-63. doi:10.1158/2326-6066.CIR-13-0034
21. Tseng YD, Nguyen MH, Baker K, et al. Effect of Patient Immune Status on the Efficacy of Radiation Therapy and Recurrence-Free Survival Among 805 Patients With Merkel Cell Carcinoma. *Int J Radiat Oncol Biol Phys*. 2018;102(2):330-339. doi:10.1016/j.ijrobp.2018.05.075
22. Schaub SK, Stewart RD, Sandison GA, et al. Does neutron radiation therapy potentiate an immune response to merkel cell carcinoma? *Int J Part Ther*. 2019;5(1):183-195. doi:10.14338/IJPT-18-00012.1
23. Macomber MW, Tarabdkar ES, Mayr NA, et al. Neutron Radiation Therapy for Treatment of Refractory Merkel Cell Carcinoma. *Int J Part Ther*. 2017;3(4):485-491. doi:10.14338/ijpt-17-00003.1

24. Moffitt GB, Stewart RD, Sandison GA, et al. Dosimetric characteristics of the University of Washington Clinical Neutron Therapy System. *Phys Med Biol*. 2018;63(10):aabd52. doi:10.1088/1361-6560/aabd52
25. Moffitt GB, Stewart RD, Sandison GA, Goorley JT, Argento DC, Jevremovic T. MCNP6 model of the University of Washington clinical neutron therapy system (CNTS). *Phys Med Biol*. 2016;61(2):93-957. doi:10.1088/0031-9155/61/2/937
26. Stewart RD, Streitmatter SW, Argento DC, et al. Rapid MCNP simulation of DNA double strand break (DSB) relative biological effectiveness (RBE) for photons, neutrons, and light ions. *Phys Med Biol*. 2015;60(21):8249-8274. doi:10.1088/0031-9155/60/21/8249
27. Chen Q, Sun L, Chen ZJ. Regulation and function of the cGAS-STING pathway of cytosolic DNA sensing. *Nat Immunol*. 2016;17(10):1142-1149. doi:10.1038/ni.3558
28. Sokolowska O, Nowis D. STING Signaling in Cancer Cells: Important or Not? *Arch Immunol Ther Exp (Warsz)*. 2018;66(2):125-132. doi:10.1007/s00005-017-0481-7
29. Abe T, Harashima A, Xia T, et al. STING Recognition of Cytoplasmic DNA Instigates Cellular Defense. *Mol Cell*. 2013;50(1):5-15. doi:10.1016/j.molcel.2013.01.039
30. Li T, Chen ZJ. The cGAS-cGAMP-STING pathway connects DNA damage to inflammation, senescence, and cancer. *J Exp Med*. 2018;215(5):1287-1299. doi:10.1084/jem.20180139
31. Li A, Yi M, Qin S, Song Y, Chu Q, Wu K. Activating cGAS-STING pathway for the optimal effect of cancer immunotherapy. *J Hematol Oncol*. 2019;12(1):1-12. doi:10.1186/s13045-019-0721-x
32. Weichselbaum RR, Liang H, Deng L, Fu Y. Radiotherapy and immunotherapy: a beneficial liaison? *Nat Rev Clin Oncol*. 2017;14(6):365-379. doi:10.1038/nrclinonc.2016.211
33. Ablasser A, Chen ZJ. CGAS in action: Expanding roles in immunity and inflammation. *Science (80-)*. 2019;363(6431):eaat8657. doi:10.1126/science.aat8657
34. Härtlova A, Erttmann SF, Raffi FAM, et al. DNA Damage Primes the Type I Interferon System via the Cytosolic DNA Sensor STING to Promote Anti-Microbial Innate Immunity. *Immunity*. 2015;42(2):332-343. doi:10.1016/j.immuni.2015.01.012

35. Vanpouille-Box C, Alard A, Aryankalayil MJ, et al. DNA exonuclease Trex1 regulates radiotherapy-induced tumour immunogenicity. *Nat Commun.* 2017;8:15618. doi:10.1038/ncomms15618
36. Zhang X, Niedermann G. Abscopal Effects With Hypofractionated Schedules Extending Into the Effector Phase of the Tumor-Specific T-Cell Response. *Radiat Oncol Biol.* 2018;1-11. doi:10.1016/j.ijrobp.2018.01.094
37. Vanpouille-Box C, Formenti SC, Demaria S. TREX1 dictates the immune fate of irradiated cancer cells. *Oncoimmunology.* 2017;6(9):1-2. doi:10.1080/2162402X.2017.1339857
38. Yang YG, Lindahl T, Barnes DE. Trex1 Exonuclease Degrades ssDNA to Prevent Chronic Checkpoint Activation and Autoimmune Disease. *Cell.* 2007;131(5):873-886. doi:10.1016/j.cell.2007.10.017
39. Hall EJ, Giaccia AJ. *Radiobiology for the Radiologist: Seventh Edition.*; 2012.
40. Semenenko VA, Stewart RD. A Fast Monte Carlo Algorithm to Simulate the Spectrum of DNA Damages Formed by Ionizing Radiation. *Radiat Res.* 2004;161(4):451-457. doi:10.1667/RR3140
41. Hill MA. Radiation Damage To Dna: the Importance of Track Structure. *PERGAMON Radiat Meas.* 1999;31:15-23. doi:10.1016/S1350-4487(99)00090-6
42. Chatterjee N, Walker GC. Mechanisms of DNA damage, repair, and mutagenesis. *Environ Mol Mutagen.* 2017;58(5):235-263. doi:10.1002/em.22087
43. Robert Grimes D, Partridge M. A mechanistic investigation of the oxygen fixation hypothesis and oxygen enhancement ratio. *Biomed Phys Eng Express.* 2015;1(4):045209. doi:10.1088/2057-1976/1/4/045209
44. Wenzl T, Wilkens JJ. Theoretical analysis of the dose dependence of the oxygen enhancement ratio and its relevance for clinical applications. *Radiat Oncol.* 2011;6(1):1-9. doi:10.1186/1748-717X-6-171
45. Tinganelli W, Durante M, Hirayama R, et al. Kill-painting of hypoxic tumours in charged particle therapy. *Sci Rep.* 2015;5:1-13. doi:10.1038/srep17016
46. Kumareswaran R, Ludkovski O, Meng A, Sykes J, Pintilie M, Bristow RG. Chronic hypoxia compromises repair of DNA double-strand breaks to drive genetic instability. *J Cell Sci.* 2012;125(1):189-199. doi:10.1242/jcs.092262

47. Dewhirst MW, Cao Y, Moeller B. Cycling hypoxia and free radicals regulate angiogenesis and radiotherapy response. *Nat Rev Cancer*. 2008;8(6):425-437. doi:10.1038/nrc2397
48. Eales KL, Hollinshead KER, Tennant DA. Hypoxia and metabolic adaptation of cancer cells. *Oncogenesis*. 2016;5(1):e190-e190. doi:10.1038/oncsis.2015.50
49. Dewhirst MW. Relationships between cycling hypoxia, HIF-1, angiogenesis and oxidative stress. *Radiat Res*. 2009;172(6):653-665. doi:10.1667/RR1926.1
50. Louie E, Nik S, Chen J, Sui J, et al. Identification of a stem-like cell population by exposing metastatic breast cancer cell lines to repetitive cycles of hypoxia and reoxygenation. *Breast Cancer Res*. 2010;12(6):R94. doi:10.1186/bcr2773
51. Rankin EB, Giaccia AJ. Hypoxic control of metastasis. *Science (80-)*. 2016;352(6282):175-180. doi:10.1126/science.aaf4405
52. Chouaib S, Umansky V, Kieda C. The role of hypoxia in shaping the recruitment of proangiogenic and immunosuppressive cells in the tumor microenvironment. *Współczesna Onkol*. 2018;2018(1):7-13. doi:10.5114/wo.2018.73874
53. Koong AC, Mehta VK, Le QT, et al. Pancreatic tumors show high levels of hypoxia. *Int J Radiat Oncol Biol Phys*. 2000;48(4):919-922. doi:10.1016/S0360-3016(00)00803-8
54. Hendrickson KRG, Juang T, Rodrigues A, Burmeister JW. Ethical violations and discriminatory behavior in the MedPhys Match. *Journal of Applied Clinical Medical Physics*. 2017:336-350.
55. Horsman MR, Mortensen LS, Petersen JB, Busk M, Overgaard J. Imaging hypoxia to improve radiotherapy outcome. *Nat Rev Clin Oncol*. 2012;9(12):674-687. doi:10.1038/nrclinonc.2012.171
56. Bell AG. On the production and reproduction of sound by light. *Am J Sci*. 1880;s3-20(118):305-324. doi:10.2475/ajs.s3-20.118.305
57. Rosencwaig A, Gersho A. Theory of the photoacoustic effect with solids. *J Appl Phys*. 1976;47(1):64-69. doi:10.1063/1.322296
58. Kruger RA, Lam RB, Reinecke DR, Del Rio SP, Doyle RP. Photoacoustic angiography of the breast. *Med Phys*. 2010;37(11):6096-6100. doi:10.1118/1.3497677
59. Hochuli R, Powell S, Arridge S, Cox B. Quantitative photoacoustic tomography using forward and adjoint Monte Carlo models of radiance. *J Biomed Opt*. 2016;21(12):126004. doi:10.1117/1.jbo.21.12.126004

60. Wang L V. Prospects of photoacoustic tomography. *Med Phys.* 2008;35(12):5758-5767. doi:10.1118/1.3013698
61. Mehrmohammadi M, Yoon SJ, Yeager D, Emelianov SY. Photoacoustic Imaging for Cancer Detection and Staging. *Curr Mol Imaging.* 2013;2(1):89-105. doi:10.2174/2211555211302010010
62. Stantz KM, Liu B, Cao M, Reinecke D, Miller K, Kruger R. Photoacoustic spectroscopic imaging of intra-tumor heterogeneity and molecular identification. In: Oraevsky AA, Wang L V., eds. *Proceedings of SPIE.* Vol 6086. ; 2006:608605. doi:10.1117/12.645106
63. Leonard JH, Dash P, Holland P, Kearsley JH, Bell JR. Characterisation of four merkel cell carcinoma adherent cell lines. *Int J Cancer.* 1995;60(1):100-107. doi:10.1002/ijc.2910600115
64. Franken N a P, ten Cate R, Krawczyk PM, et al. Comparison of RBE values of high-LET α -particles for the induction of DNA-DSBs, chromosome aberrations and cell reproductive death. *Radiat Oncol.* 2011;6(1):64. doi:10.1186/1748-717X-6-64
65. Seth I, Schwartz JL, Stewart RD, Emery R, Joiner MC, Tucker JD. Neutron exposures in human cells: Bystander effect and relative biological effectiveness. *PLoS One.* 2014;9(6). doi:10.1371/journal.pone.0098947
66. Stewart RD, Yu VK, Georgakilas AG, Koumenis C, Park JH, Carlson DJ. Effects of Radiation Quality and Oxygen on Clustered DNA Lesions and Cell Death. *Radiat Res.* 2011;176(5):587-602. doi:10.1667/rr2663.1
67. Nikjoo H, O'Neill P, Goodhead DT, Terrissol M. Computational modelling of low-energy electron-induced DNA damage by early physical and chemical events. *Int J Radiat Biol.* 1997;71(5):467-483. doi:10.1080/095530097143798
68. Moskvina V, Stewart RD, Tsiamas P, Axente M, Farr J. TU-EF-304-10: Efficient Multiscale Simulation of the Proton Relative Biological Effectiveness (RBE) for DNA Double Strand Break (DSB) Induction and Bio-Effective Dose in the FLUKA Monte Carlo Radiation Transport Code. *Med Phys.* 2015;42(6):3617-3617. doi:10.1118/1.4925665
69. Ferrari A, Sala PR, Fasso A, Ranft J. FLUKA: A multi-particle transport code, available at <http://www.slac.stanford.edu/cgi-wrap/getdoc/slac-r-773.pdf>, accessed February 15, 2016. *Cern Infn/Tc_05/11, Slac-R-773.* 2005;(October). doi:10.5170/CERN-2005-010

70. Böhlen TT, Cerutti F, Chin MPW, et al. The FLUKA Code: Developments and challenges for high energy and medical applications. *Nucl Data Sheets*. 2014;120:211-214. doi:10.1016/j.nds.2014.07.049
71. Deasy JO, Blanco AI, Clark VH. CERR: A computational environment for radiotherapy research. *Med Phys*. 2003;30(5):979-985. doi:10.1118/1.1568978
72. Hsi WC, Moyers MF, Nichiporov D, et al. Energy spectrum control for modulated proton beams. *Med Phys*. 2009;36(6Part1):2297-2308. doi:10.1118/1.3132422
73. Kanemoto A, Hirayama R, Moritake T, et al. RBE and OER within the spread-out Bragg peak for proton beam therapy: In vitro study at the Proton Medical Research Center at the University of Tsukuba. *J Radiat Res*. 2014;55(5):1028-1032. doi:10.1093/jrr/rru043
74. Semenenko VA, Stewart RD. Fast Monte Carlo simulation of DNA damage formed by electrons and light ions. *Phys Med Biol*. 2006;51(7):1693-1706. doi:10.1088/0031-9155/51/7/004
75. Stewart RD. Induction of DNA damage by light ions relative to ^{60}Co γ -rays. *Int J Part Ther*. 2018;5(1):25-39. doi:10.14338/IJPT-18-00030
76. Spada S, Yamazaki T, Vanpouille-Box C. *Detection and Quantification of Cytosolic DNA*. Vol 629. 1st ed. Elsevier Inc.; 2019. doi:10.1016/bs.mie.2019.07.042
77. Schoenhals JE, Seyedin SN, Tang C, et al. Preclinical Rationale and Clinical Considerations for Radiotherapy Plus Immunotherapy: Going Beyond Local Control. *Cancer J*. 2016;22(2):130-137. doi:10.1097/PPO.0000000000000181
78. Formenti SC. Optimizing Dose Per Fraction: A New Chapter in the Story of the Abscopal Effect? *Int J Radiat Oncol Biol Phys*. 2017;99(3):677-679. doi:10.1016/j.ijrobp.2017.07.028
79. Takahashi Y, Yasui T, Minami K, et al. Carbon ion irradiation enhances the antitumor efficacy of dual immune checkpoint blockade therapy both for local and distant sites in murine osteosarcoma. *Oncotarget*. 2019;10(6):633-646. doi:10.18632/oncotarget.26551
80. Mouriaux F, Zaniolo K, Bergeron MA, et al. Effects of long-term serial passaging on the characteristics and properties of cell lines derived from uveal melanoma primary tumors. *Investig Ophthalmol Vis Sci*. 2016;57(13):5288-5301. doi:10.1167/iovs.16-19317

81. Xia T, Konno H, Ahn J, Barber GN. Deregulation of STING Signaling in Colorectal Carcinoma Constrains DNA Damage Responses and Correlates With Tumorigenesis. *Cell Rep.* 2016;14(2):282-297. doi:10.1016/j.celrep.2015.12.029
82. Wu MZ, Cheng WC, Chen SF, et al. MiR-25/93 mediates hypoxia-induced immunosuppression by repressing cGAS. *Nat Cell Biol.* 2017;19(10):1286-1296. doi:10.1038/ncb3615
83. Bristow RG, Hill RP. Hypoxia and metabolism: Hypoxia, DNA repair and genetic instability. *Nat Rev Cancer.* 2008;8(3):180-192. doi:10.1038/nrc2344
84. Demaria S, Formenti SC. Radiation as an immunological adjuvant: current evidence on dose and fractionation. *Front Oncol.* 2012;2(October):1-7. doi:10.3389/fonc.2012.00153
85. Vaupel P, Mayer A. Hypoxia in cancer: Significance and impact on clinical outcome. *Cancer Metastasis Rev.* 2007;26(2):225-239. doi:10.1007/s10555-007-9055-1
86. Kruger S, Ilmer M, Kobold S, et al. Advances in cancer immunotherapy 2019 - Latest trends. *J Exp Clin Cancer Res.* 2019;38(1):1-11. doi:10.1186/s13046-019-1266-0
87. Deng L, Liang H, Xu M, et al. STING-Dependent Cytosolic DNA Sensing Promotes Radiation-Induced Type I Interferon-Dependent Antitumor Immunity in Immunogenic Tumors. *Immunity.* 2014;41(5):843-852. doi:10.1016/j.immuni.2014.10.019
88. Paganetti H. Range uncertainties in proton therapy and the role of Monte Carlo simulations. *Phys Med Biol.* 2012;57(11):R99--117. doi:10.1088/0031-9155/57/11/R99
89. Saito M. Potential of dual-energy subtraction for converting CT numbers to electron density based on a single linear relationship. *Med Phys.* 2012;39(4):2021-2030. doi:10.1118/1.3694111
90. Hansen DC, Seco J, Sangild Sørensen T, et al. A simulation study on proton computed tomography (CT) stopping power accuracy using dual energy CT scans as benchmark. *Acta Oncol (Madr).* 2015;(October 2016):1-5. doi:10.3109/0284186X.2015.1061212
91. Alsanea F, Moskvina V, Stantz KM. Feasibility of RACT for 3D dose measurement and range verification in a water phantom. *Med Phys.* 2015;42(2):937-946. doi:10.1118/1.4906241
92. Uzunyan SA, Blazey G, Boi S, et al. A New Proton CT Scanner. *23rd Conf Appl Accel Res Ind CAARI.* 2014:1-6. <http://arxiv.org/abs/1409.0049>.

93. Arbor N, Dauvergne D, Dedes G, et al. Monte Carlo comparison of x-ray and proton CT for range calculations of proton therapy beams. *Phys Med Biol.* 2015;60(19):7585. doi:10.1088/0031-9155/60/19/7585
94. Al-Ani A, Toms D, Kondro D, Thundathil J, Yu Y, Ungrin M. Oxygenation in cell culture: Critical parameters for reproducibility are routinely not reported. *PLoS One.* 2018;13(10):1-13. doi:10.1371/journal.pone.0204269
95. Wu D, Yotnda P. Induction and Testing of Hypoxia in Cell Culture. *J Vis Exp.* 2011;(54):4-7. doi:10.3791/2899
96. Jiang B, Ren C, Li Y, et al. Sodium sulfite is a potential hypoxia inducer that mimics hypoxic stress in *Caenorhabditis elegans*. *J Biol Inorg Chem.* 2011;16(2):267-274. doi:10.1007/s00775-010-0723-1
97. Wilson JD, Hammond EM, Higgins GS, Petersson K. Ultra-High Dose Rate (FLASH) Radiotherapy: Silver Bullet or Fool's Gold? *Front Oncol.* 2020;9(January):1-12. doi:10.3389/fonc.2019.01563
98. Rama N, Saha T, Shukla S, et al. Improved Tumor Control Through T-cell Infiltration Modulated by Ultra-High Dose Rate Proton FLASH Using a Clinical Pencil Beam Scanning Proton System. *Int J Radiat Oncol.* 2019;105(1):S164-S165. doi:10.1016/j.ijrobp.2019.06.187

APPENDIX A. INTERFERON BETA ELISA PROTOCOL

This assay uses the DuoSet Human IFN β ELISA kit, as well as the general ancillary kit, which includes optimized well plates and all needed reagents aside from complete medium and samples.

Reagent preparation

All should be done before beginning assay. Reconstitutions should be performed with reagents at room temperature. After adding the liquid diluent, the antibody/standard vials should be recapped, and allowed to sit at room temperature for 15mins, ideally with slow rocking/agitation.

1. Capture antibody

- Reconstitute with 0.5 mL PBS (supplied in ancillary kit)
- Aliquot into 5 x 0.1 mL samples, freeze at -20C

2. Wash buffer (0.5% Tween-20 in PBS)

- Add 20mL of 25x concentrate to 480 mL DI H₂O, mix
- Store for ~1 month at 2-8C

3. Reagent diluent (1% BSA in PBS)

- Dilute 1:10 in DI H₂O
- For prep, prepare 2 mL
 - 0.2mL of reagent diluent concentrate in 1.8mL DI H₂O
- Store opened concentrate at 2-8C for up to 1 month.
 - Only dilute as much as needed each day.

4. Detection antibody

- Reconstitute with 1mL reagent diluent
- Aliquot into 5 x 0.2 mL samples, freeze at -20C

5. IFN β Standard

- Reconstitute with 0.5 mL reagent diluent
- Aliquot into 0.1 mL samples, freeze at -70C

Day One (plate preparation)

1. Thaw capture antibody stock, allow to equilibrate to room temperature with supplied PBS
2. Dilute 83 μ L of capture antibody stock in 10mL PBS

- working concentration = 4 ug/mL
- 3. Coat 96-well plate with **capture antibody** at working concentration, 100uL/well
- 4. Seal plate and incubate overnight at room temperature
 - Do NOT use plate shaker. Leave on benchtop.

Day Two (plate preparation)

1. Prepare reagents
 - Mix fresh **reagent diluent**
 - 30mL needed for blocking the plate
 - 3mL reagent diluent concentrate in 27 mL DI H2O
 - 20 mL needed for detection antibody, streptavidin-HRP
 - *Skip this step if the plate isn't being assayed on the same day*
 - 2mL concentrate in 18 mL DI H2O
 - Thaw detection antibody *if using on the same day*
2. Aspirate and wash with **wash buffer** 3x
 - ~200uL wash buffer distributed with multichannel pipette
 - Invert plate over sink, shake to remove buffer
 - Pat on paper towel to remove excess buffer
 - *Make sure to completely remove buffer for best performance*
3. Block plates with **reagent diluent**, 300 uL/well
 - Incubate 1hr at RT
4. Aspirate/wash 3x with **wash buffer**
 - This can be treated as a stopping point if needed. Make sure the plate is filled with wash buffer, cover with a plate sealer, and store at 4C. Should be good for 1-2 days.

Day Three (Assay; if plate stored overnight)

5. *Prepare 20mL reagent diluent if needed for standards/streptavidin*
6. Prepare samples/standards
 - can be done concurrently with step 3 if done on the same day
 - Thaw samples for at least 30mins in room temp. water bath

- Standards: 7-point twofold calibration curve.
 - Thaw IFN β **standard**
 - Prepare/label 10 Eppendorf tubes
 - Includes two extra standards, higher than what will be plated. This enables use of >10uL antibody stock to limit some pipetting errors, while maintaining datapoints at low concentrations.
 - 1mL **complete cell growth medium** to most-concentrated standard, 0.5mL else
 - Add 10uL of IFN β standard to 1mL of medium for highest standard (1800 pg/mL)
 - Transfer 500uL to next-highest sample, mix. Repeat.
 - Use reagent diluent **ONLY** as low standard.
 - Plated concentrations: [450, 225, 113, 56, 28, 14, 7, 0] pg/mL
 - **Samples:** cell-free supernatant
 - Thaw and allow to equilibrate, if necessary
7. Add 100uL of prepared **sample or standard** (diluted in reagent diluent if needed).
 - Cover with plate sealer and incubate 2hrs at room temp
 8. Aspirate/wash 3x with **wash buffer**
 9. Add 100uL of **detection antibody** at working concentration.
 - Dilute detection antibody stock in reagent diluent.
 - Use 0.167mL antibody stock in 10mL of reagent diluent (working concentration = 100 ng/mL)
 - Cover with plate sealer and incubate 2hrs at room temperature.
 - NOTE: If time to reach plate reader > 20mins, move plate and remaining supplies closer *before* the next step. Need:
 - Multichannel pipette, pipette tips, 3-4 reagent reservoirs, biohazard bag, gloves, paper towels, plate sealers, foil
 - 10 mL reagent diluent, 5 mL each color reagent A and B (keep separate), 5 mL stop solution, 0.25mL Streptavidin HRP (cover in foil), wash buffer
 10. Aspirate/wash 3x with **wash buffer**
 11. Add 100uL of **Streptavidin-HRP** to each well, incubate 20mins at room temperature

- Prep streptavidin-HRP by diluting stock 1:40 in reagent diluent
 - 0.25 mL stock to 9.75mL reagent diluent
- From here, avoid putting the plate in direct light
- 12. Aspirate/wash 3x with **wash buffer**
- 13. Add 100uL of substrate solution, incubate 20mins at room temperature.
 - Mix equal parts of **color reagents A and B** (5mL each for one plate)
 - Use within 15mins of mixing.
- 14. Add 50 uL of **stop solution** to each well. Tap plate to mix.
- 15. Read out ASAP.
 - **Optical density at 450nm**
 - Use wavelength correction at 540-570nm if available, to correct for plate imperfections
 - If not, find reading at 540 or 570 nm, subtract from signal at 450nm

APPENDIX B. TREX1 IMMUNOFLUORESCENCE PROTOCOL

This assay uses an anti-Trex1 antibody pre-conjugated with an Alexa fluorochrome, with supplies that are common around biology labs. Staining for additional antibodies (such as dsDNA) can be added onto this protocol by washing 3x before/after exposure.

Reagents:

- PBS
- 4% formaldehyde in PBS [mix 1.1mL formaldehyde (37% w/w) in 9 mL PBS]
- 0.5% Tween-20 in PBS
- 3% BSA in PBS
- Pre-conjugated Ab 1:500 in PBS
- ProGold w/DAPI

Use 1 mL of reagent per well in 4-well chamber slides for fixation, blocking, washing. Volume can be reduced to 0.5 mL per well for antibody staining, to conserve supplies. All steps should be performed while slowly rocking at room temperature.

Staining:

1. Remove supernatant, rinse w/PBS 5min (1-2X)
2. Add 4% formaldehyde (in PBS) for 10min
3. Remove fixative, rinse w/PBS 5min (1-2X)
4. Add 0.5% Tween-20 (in PBS) for 10min
5. Remove Tween, rinse w/PBS 5min (2X)
6. Add 3% BSA (in PBS) 30-60min
7. Remove BSA, rinse w/PBS 5min (2X)
8. **[move rocker to darkened room]**
9. Add anti-Trex1 Ab (1:500) (in PBS) for 2hr

10. Remove Ab, rinse w/PBS 5min (**3X**)
11. Tap upside down to dry, remove chambers using tool
12. add 1 drop ProGold w/DAPI, then square coverslip
13. let dry, store in dark (ProGold acts as its own sealant)

APPENDIX C. CYTOSOLIC DSDNA QUANTIFICATION PROTOCOL

This assay follows the conventions published by Vanpouille-Box et al., using NE-PER Nuclear and Cytoplasmic extraction and SpectraMax dsDNA Nano quantification kits.

Cytoplasmic Extraction

- Detach cells with trypsin for 3mins at RT, count
- Transfer suspensions to 15mL tubes, centrifuge/aspirate medium and wash with PBS
- Transfer cells to 1.5mL tube, centrifuge at 500xg (2500 rpm) for 2-3 mins
 - Want 1-10 million cells per tube
- Aspirate buffer as well as possible
- Add ice-cold CER I to cell pellet
 - 100uL per million cells
 - Add HALT protease inhibitor at 10uL per mL CER I
 - Note: add HALT to total volume of CER I for all samples before adding to cells
- Vortex at high setting (15 seconds) to resuspend pellet
- Incubate 10mins on ice
- Add ice-cold CER II to tube
 - 5.5 uL per million cells
- Vortex on high setting for five seconds and incubate on ice for 1 minute
- Vortex again for 5 seconds
- Centrifuge for 5 mins at highest speed in microcentrifuge (~14000rpm = 16000 x g on Eppendorf 5415 centrifuge)
- Supernatant contains cytoplasmic extracts – transfer to pre-chilled tube and place on ice.
 - Extracts can be stored short-term at -20C, long-term at -80C

dsDNA quantification

- Expect ~13,000 ng dsDNA per million cells (from MC38 data). Kit's max dynamic range is 250 ng per well. Should only plate cytoplasmic extract for ~20,000 viable cells per well

- Allow kit components to equilibrate to room temperature
- Vortex and centrifuge components briefly to minimize reagent loss in cap
- Dilute AccuClear Nano buffer to 1X with DI water
 - Typical dilution: 42 wells
 - 8.0 mL DI water
 - 0.4 mL Nano Buffer
- Prepare dsDNA standards
 - Note: unnecessary with Bulk kit
- Dilute Nano dye 1:100 in 1X Nano buffer ('working solution')
- Add dsDNA standards and unknown samples to black 96 well plate
 - Fill three wells per sample for triplicate testing
 - 10uL sample, 200uL working solution
- Allow 5 mins incubation at RT in the dark
- Readout ASAP – expect 15% signal decrease at 3hrs following combination of working solution and DNA. Kit recommends readout within 1 hour.
 - Abs. 468nm, emit 507nm

VITA

Devin Miles

Education

Ph.D.	PURDUE UNIVERSITY Medical Physics Track: Therapeutic Radiological Physics Advisor: Keith Stantz	2016-2020
M.S.	DUKE UNIVERSITY Medical Physics, May 2016 Track: Radiation Therapy Physics Advisor: Mark Oldham	2014-2016
B.S.	CASE WESTERN RESERVE UNIVERSITY Physics, May 2014 Advisor: Glenn Starkman, David Jordan	2010-2014

Certification Progress

2016	American Board of Radiology Part 1: Therapeutic Medical Physics - Passed
------	---

Experience

2018 – pres.	University of Washington Medical Center, Dept. of Radiation Oncology Visiting Scientist and Research Technologist, Radiation Biology Laboratory <ul style="list-style-type: none">• Designed and performed in-vitro experiments to explore radiation-induced STING effects on murine and human cells, and variations caused by high LET radiation and low oxygenation. Collaboration with Stantz Lab at Purdue University• Maintain cell cultures used in UW research projects, prepare cell culture media, sterilize equipment and media, cryopreserve samples, and properly dispose of biohazard wastes• Maintain inventory of laboratory mice• Operate and maintain standard laboratory instruments such as spectrophotometers, centrifuges, coulter counters, incubators, microscopes, and balances• Routine laboratory housekeeping tasks including dishwashing, ordering supplies, properly disposing of chemical wastes, computer maintenance and data backup, and other duties as required
--------------	--

- Assist with experiments according to established protocols
- Participate in laboratory meetings and planning sessions
- Shadowed medical physicists, residents, radiation therapists

2016 – 2020

Purdue University, School of Health Sciences

Graduate Researcher, Stantz Lab

- Investigating in-vivo photoacoustic CT spectroscopy and dynamic-contrast enhanced imaging to characterize tumor hypoxia, and examining implications in anti-angiogenic and immune therapies
- Investigating the impact of radiation quality and oxygenation on STING radio-immune modulation through Monte Carlo modeling, in-vitro experiments
- Mentoring graduate and undergraduate students in medical physics projects

2014-2016

Duke University, Dept. of Radiation Oncology

Graduate Researcher, 3D Dosimetry and Optical Bio-Imaging Lab

- Characterized novel formulations of PRESAGE dosimeters to support long-term dosimeter stability, reusability, and deformability
- Designed, prototyped, and benchmarked a solid-tank optical-CT system for 3D dosimeter readout
- Performed treatment planning and small-field dosimetry to support orthovoltage preclinical radiotherapy studies (using PXi XRAD 225cx), with applications in lung SBRT, hippocampal avoidance in whole-brain radiotherapy, and radiation-induced normal tissue toxicities
- Applied 3D printing techniques to support a wide range of RT studies, including orthovoltage 3D-conformal RT and IMRT, spatially-fractionated RT (GRID/Lattice), coded-aperture spectral imaging for cancer detection, and micro-CT calibration
- Developed deformable PRESAGE prostate and GYN phantoms for 3D dosimetry of volumetric interstitial brachytherapy irradiations
- Investigated remote 3D dosimetry to validate ViewRay MRI-guided IMRT treatment plans, in collaboration with Washington Univ., St. Louis
- Shadowed medical physicists, physics residents

2013-2014

University Hospitals Cleveland, Dept. of Radiology

Research Assistant/Intern

- Investigated textural analysis techniques to quantify image heterogeneity in PET images from PET/CT and PET/MR systems
- Shadowed clinical diagnostic-imaging medical physicist

2011-2013

Case Western Reserve University, Dept. of Physics

Research Assistant, High-Energy Astrophysics Group

- Investigated the effect of cross-sectional shape on the optical and electrical properties of quantum nanowires through finite element analysis
- Performed Monte Carlo simulations to optimize detector geometry for OSETI system

Affiliations

- **American Association of Physicists in Medicine**, student member, 2014 – present
- **Radiation Research Society**, student-in-training, 2016-present

Grants

NIH/STTR	R41CA217421 (PI: Mark Oldham; John Adamovics)	2016
-----------------	--	------

A practical and versatile high-resolution 3D dosimetry system for clinical use

Patents

-
- **ECONOMICAL DRY-TANK OPTICAL CT SCANNER AND METHODS OF USING SAME**; US Provisional Patent Application 62/478,700

Awards

-
- **Purdue Bilsland Dissertation Fellowship**, 2018-2019
 - **Purdue Compton Travel Grant**, 2017
 - **Purdue Doctoral Fellowship**, 2016-2020

Service

-
- Journal review, *Medical Physics*, 2017 – pres.
 - Duke Graduate and Professional Student Council, 2015

Relevant Skills

Software	MATLAB 3D Slicer FLUKA general purpose Monte Carlo Monte Carlo Damage Simulation Radiation treatment simulation: Eclipse, SmART-PLAN, Muriplan CAD modeling
Physics	Gel dosimetry, optical-CT imaging 3D printing Photoacoustic CT imaging
Biology	Aseptic cell culture technique Mouse and rat handling, anesthesia, euthanasia, necropsy, tail vein injection Flow cytometry, immunofluorescence assay ELISA, microplate fluorescence assay Comet assay

Publications

- 1. Differential effects of high versus low LET radiation on type-I interferon response through STING**
D Miles, N Cao, G Sandison, RD Stewart, T Pulliam, U Parvathaneni, P Goff, P Nghiem, G Moffitt, K Stantz, Submitted to *Int. J. Radiation Oncol. Biol. Phys.*, 2020
- 2. A preclinical study of longitudinal photoacoustic CT spectroscopy to characterize intra-tumor hypoxic status**
D Miles, T Nguyen, F Stirm, A Moustaki, B Youngblood, K Stantz; In preparation for *Phys. Med. Biol.*, 2020
- 3. A Method for Generating Intensity Modulated Radiation Therapy Fields for Small Animal Irradiators Utilizing 3D Printed Compensator Molds**
S Yoon, J Kodra, *D Miles*, D Kirsch, M Oldham; Accepted for *Med. Phys.*, 2020
- 4. Development and preliminary evaluation of a murine model of chronic radiation-induced proctitis**
K Ashcraft*, *D Miles**, M Sunday, K Choudhury, K Young, G Palmer, P Patel, E Woska, R Zhang, M Oldham, M Dewhirst, B Koontz; *Int. J. Radiation Oncol. Biol. Phys.* 101(5), 1194-1201, 2018.; *equal contribution
- 5. A precision 3D conformal treatment technique in rats: application to whole brain radiotherapy with hippocampal avoidance**
S Yoon, C Cramer, *D Miles*, M Reinsvold, KM Joo, D Kirsch, M Oldham; *Med. Phys.*, 44(11), 6008–6017, 2017

6. **Three-Dimensional Dosimetric Validation of a Magnetic Resonance Guided Intensity Modulated Radiation Therapy System.**
L Rankine, S Mein, B Cai, A Cururu, T Juang, **D Miles**, S Mutic, Y Wang, M Oldham, H Li; *Int. J. Radiation Oncol. Biol. Phys.* 97(5), 1095-1104, 2017
7. **Utilizing a Diagnostic kV Imaging System for X-Ray-Psoralein Activated Cancer Therapy (X-PACT)**
J Adamson, S Mein, B Meng, R Gunasingha, S Yoon, **D Miles**, H Walder, Z Fathi, W Beyer, N Spector, T Gieger, M Nolan, M Oldham; *Biomed. Phys. Eng. Express* 3, 035018, 2017
8. **A prototype cost-effective optical-CT system for PRESAGE 3D dosimetry readout**
D Miles, S Yoon, J Kodra, J Adamovics, M Oldham; *IOP Conf. Series: Journal of Physics: Conf. Series* 847 012026, 2016
9. **Treatment Planning and 3D Dose Verification of Whole Brain Radiotherapy with Hippocampal Avoidance in Rats**
S Yoon, **D Miles**, C Cramer, M Reinsvold, D Kirsch, M Oldham; *IOP Conf. Series: Journal of Physics: Conf. Series* 847 012004, 2016
10. **Characterization of novel preclinical dose distributions for micro irradiator**
J Kodra, **D Miles**, S Yoon, D Kirsch, M Oldham; *IOP Conf. Series: Journal of Physics: Conf. Series* 847 012054, 2016
11. **How feasible is remote 3D dosimetry for MR-guided Radiation Therapy (MRgRT)?**
S Mein, L Rankine, **D Miles**, T Juang, B Cai, A Cururu, S Mutic, J Fenoli, J Adamovics, H Li, M Oldham; *IOP Conf. Series: Journal of Physics: Conf. Series* 847 012056, 2016
12. **Investigation into the feasibility of optical-CT 3D dosimetry with minimal use of refractively matched fluids**
K Chisholm, **D Miles**, L Rankine, M Oldham; *Med. Phys* 42(5), 2607–14, 2014

Presentations/Posters

-
1. **STING and Trex1 as radiation-induced regulators of tumor immunogenicity**
D Miles, Oral presentation at *University of Washington Neutron and Immunotherapy Journal Club*, Seattle, WA 2019
 2. **Photoacoustic CT to characterize the effects of antiangiogenic drugs on acute and chronic hypoxia**
D Miles, K Stantz, Oral Presentation at *61st Annual Meeting of the AAPM*, San Antonio, Tx, 2019
 3. **A Monte Carlo study of STING induction in radiation therapy**
D Miles, V Moskvin, K Stantz, Oral Presentation at *60th Annual Meeting of the AAPM*, Nashville, TN, 2018
 4. **Photoacoustic CT to characterize acute and chronic hypoxia**
D Miles, T Nguyen, F Stirm, K Stantz, Oral Presentation at *60th Annual Meeting of the AAPM*, Nashville, TN, 2018

5. **Implementation of IMRT treatment to preclinical micro-irradiator**
J Kodra, SW Yoon, *D Miles*, D Kirsch, M Oldham; Poster at *Duke University Physics in Medicine Tri-Program Interdisciplinary Summit*, Durham, NC, 2017
6. **Investigations on the temporal evolution of antivascular effects induced by anti-angiogenic therapy using multiple imaging modalities in an orthotopic syngeneic mouse model**
M Castanares, B Chavali, C Meyer, *D Miles*, M Babur, R Little, S Cheung, Y Watson, J Stewart, B Falcon, K Williams, G Plowman, K Stantz, J O'Connor, S Chintharlapalli, E Collins; Poster at *2017 World Molecular Imaging Congress*, Philadelphia, PA, 2017
7. **An Auxiliary Minibeam Collimator for Preclinical Proton Radiotherapy**
D Miles, K Stantz, V Moskvina, J Farr; E-Poster at *59th Annual Meeting of the AAPM*, Denver, CO, 2017
8. **Characterization of a Novel Light-Collimating Tank Optical-CT System for 3D Dosimetry**
D Miles, S Yoon, J Adamovics, M Oldham; Presentation at *58th Annual Meeting of the AAPM*, Washington DC, 2016
9. **3D Remote Dosimetry for MRI-Guided Radiation Therapy: A Hybrid Approach**
L Rankine, S Mein, J Adamovics, B Cai, A Curcuro, T Juang, *D Miles*, S Mutic, Y Wang, M Oldham, H Li; Presentation at *58th Annual Meeting of the AAPM*, Washington DC, 2016
10. **Validation of ELP Dosimetry Using PRESAGE Dosimeter: Feasibility Test and Practical Considerations**
K Lambson, K Lafata, J Schaal, *D Miles*, S Yoon, W Liu, M Oldham, J Cai; Poster at *58th Annual Meeting of the AAPM*, Washington DC, 2016
11. **Rodent-morphic PRESAGE 3D Dosimetry and High-Precision Preclinical RT with 3D Printed Beam-Shaping Tools**
D Miles, S Yoon, C Cramer, D Kirsch, M Oldham; Presentation at *Precision X-Ray User Meeting*, Washington DC, 2016
12. **Toward a Deformable 3D Dosimeter for Plan Verification of Multi-Modality Treatments**
D Miles, T Juang, J Adamovics, J Chino, M Oldham, O Craciunescu, E-Poster at *2016 World Congress of Brachytherapy*, San Francisco, CA
13. **Feasibility of a micro-radiotherapy technique to investigate hippocampal sparing in whole-brain radiotherapy in rats**
D Miles, S Yoon, C Cramer, M Reinsvold, D Kirsch, M Oldham, E-Poster at *2016 International Conference on the use of Computers in Radiation Therapy (ICCR)*, London, UK
14. **Effects of Time and Temperature on a Potential Reusable 3D Dosimeter**
T Juang, *D Miles*, E Crockett, J Adamovics, M Oldham; Poster at *56th Annual Meeting of the AAPM*, Anaheim, CA, 2015
15. **Tissue-Equivalent Material Phantom to Test and Optimize Coherent Scatter Imaging for Tumor Classification**

K Albanese, R Morris, ***D Miles***, M Lakshmanan, J Greenberg, A Kapadia; Poster at *56th Annual Meeting of the AAPM*, Anaheim, CA, 2015